UNIVERSITÀ
DEGLI STUDI
FIRENZE

DOTTORATO DI RICERCA IN
FISICA E ASTRONOMIA

CICLO XXXVIII

Evolution of the reaction dynamics in the ^{58}Ni+^{58}Ni system at Fermi energies.

Settore Scientifico Disciplinare PHYS-01/A

Dottoranda
Dott.ssa Baldesi Lucia

Supervisori
Prof. Barlini Sandro

Dott. Camaiani Alberto

Coordinatore
Prof. Giovanni Modugno

Salvo eventuali più ampie autorizzazioni dell'autore, la tesi può essere liberamente consultata e può essere effettuato il salvataggio e la stampa di una copia per fini strettamente personali di studio, di ricerca e di insegnamento, con espresso divieto di qualunque utilizzo direttamente o indirettamente commerciale.
Ogni altro diritto sul materiale è riservato.

Contents

Introduction **3**

1 Physics case **7**
1.1 Reaction dynamics at Fermi energies . . . 10
1.1.1 The neutron enrichment of the neck and the isospin drift phenomenon . . . 15
1.2 The source reconstruction . . . 17

2 The INDRA-FAZIA experimental apparatus **21**
2.1 FAZIA . . . 21
2.1.1 The detectors . . . 22
2.1.2 The electronics . . . 25
2.1.3 FAZIA trigger . . . 27
2.1.4 Digital treatment of the signals . . . 28
2.2 INDRA . . . 29
2.3 The INDRA-FAZIA coupling . . . 30
2.4 Identification techniques . . . 31
2.4.1 ΔE-E method . . . 32
2.4.2 Pulse Shape Analysis in silicon detectors . . . 33
2.4.3 Pulse Shape Analysis in CsI(Tl) . . . 35

3 ^{58}Ni+^{58}Ni at 32, 52, 74 AMeV **37**
3.1 Identification procedure . . . 39
3.2 Energy calibration . . . 47

4 Theoretical models and simulations **53**
4.1 Antisymmetrized Molecular Dynamics . . . 54
4.2 GEMINI . . . 57
4.3 HIPSE and SIMON . . . 59
4.4 Filter and first comparison with experimental data . . . 60
4.5 The dynamical phase within AMD . . . 63

5 Selection and characterization of the reaction channels 69
5.1 Preliminary event selection 70
5.2 Selection of the QP evaporation channel 70
5.3 Selection of the QP breakup channel 77
5.3.1 Statistical vs dynamical origin of the breakup 80
5.4 Reaction centrality estimation 82

6 Characterization of secondary fragments 87
6.1 Characteristics of the QP fragments 88
6.1.1 QPr channel 89
6.1.2 QPb channel 92
6.1.3 Comparison between QPr and QPb channels 94
6.2 Light particles in coincidence with the QP 95
6.2.1 Efficiency correction 96
6.2.2 Isospin characteristics of light particles 99

7 Primary source reconstruction 103
7.1 Reconstruction of the initial projectile 104
7.2 Pre-equilibrium contribution 109
7.3 Disentanglement of evaporation and midvelocity components . 112
7.4 Isospin characteristics of evaporative and midvelocity emissions 120

Conclusions 125

A PSA identification thresholds 129

B Response of FAZIA CsI(Tl) to energetic protons 135

Bibliography 140

Introduction

In nuclear physics, the Fermi energy domain (20-100 AMeV) is a transition region in which reaction mechanisms exhibit the interplay between mean-field effects and nucleon-nucleon collisions. Heavy-ion collisions in this regime are generally described as a two-step process: a dynamical phase, corresponding to the primary interaction between projectile and target, and a statistical phase, in which the hot fragments produced in the first stage undergo de-excitation. The outcome of the dynamical phase, and thus the final characteristics of the secondary fragments, strongly depends on the beam energy, the reaction centrality, and the size of the colliding nuclei.

This work focuses on peripheral and semiperipheral collisions, where the exit channel is predominantly binary, with two heavy fragments: the quasi-projectile (QP) and quasi-target (QT). Less frequently, especially if the reacting nuclei are not heavy, strong deformations of the QP and/or QT along the separation axis can lead to their breakup through a process with exhibits dynamical characteristics.

One of the most interesting features in semiperipheral collisions at Fermi energies is the enhancement of Light Charged Particles and Intermediate Mass Fragments at intermediate velocities, between those of the QP and the QT. Moreover, such emission present a neutron-to-proton content larger with respect to the evaporative one. The enhanced emissions and their chemical composition are related to the dynamics of the collision. A low-density region connecting the QP and QT, called "neck", develops during the interaction and a net flow of neutrons is expected to arise due to the density gradient between the region at saturation density and the neck. Its rupture is expected to generate the enhanced and neutron-richer emissions at midvelocity.

The main goal of this thesis is to investigate the reaction dynamics by reconstructing the primary sources emerging after the projectile-target interaction in the ^{58}Ni+^{58}Ni system, and to track them as a function of the reaction centrality and the beam energy, i.e., 32, 52, and 74 AMeV. This detailed investigation is possible thanks to the features of the INDRA-FAZIA apparatus, which combines the excellent isotopic resolution of the FAZIA ar-

ray with the large angular coverage of the INDRA multidetector. An original aspect of this work is the fact that the source reconstruction is performed for both the main evaporative channel (QPr channel) and the breakup channel (Qpb channel), where the breaking-up source can be accessed by detecting and identifying, in charge and mass, the two fission fragments.

Starting from the detected cold fragment, each event class is investigated by analysing the remnant or reconstructed quasi-projectile and the accompanying light fragments (Z<5), which can be produced either during the statistical de-excitation path of the primary hot sources or dynamically emitted due to mechanical instabilities arising during the dynamical evolution of the whole system.

The AMD transport model, coupled with GEMINI++ as afterburner, which provides an overall good reproduction of the experimental observables, is used to strengthen the centrality sorting events and to gain insight into the reaction dynamics as predicted by the model. Moreover, the AMD+GEMINI simulations are used to estimate the detector efficiency for light fragments, a key step for reliably extrapolating the primary source properties.

The proposed method for the reconstruction of the primary sources is based on a calorimetric approach. Starting from all the light fragments associated with the QP phase space (in both evaporative and breakup channels), the evaporative and mid-velocity components are disentangled by means of angular distribution assumptions. By combining the evaporative component with the detected or reconstructed quasi-projectile, the excited QP* source is obtained, while the midvelocity component corresponds to the neck source. It is worth noting that, in this work, for the first time, such a complete reconstruction of the primary sources is applied to the breakup channel, allowing for a direct comparison of the results obtained in the two channels. According to the AMD+GEMINI model, the reconstructed source is estimated to form between 100-300 fm/c from the onset of the collision. This allows access to the isospin content of both the evaporated particles and the neck, providing insight into the isospin drift as a function of the reaction centrality and beam energy.

This thesis is organized as follows. Chapter 1 introduces the physics case with particular attention to the aspect of the reaction dynamics more strictly connected to the purpose of this work. Chapter 2 presents the INDRA-FAZIA apparatus and the employed identification techniques, while in Chapter 3 the experiments in which the ^{58}Ni+^{58}Ni reactions were measured and the data reduction procedures are described. Chapter 4 introduces the theoretical models used in this work and discusses the features of the dynamical phase predicted by the AMD model. Chapter 5 details the event selection of the QPr and QPb channels, giving a first hint of their general characteristics and

proposing a centrality estimator. Chapter 6 focuses on the properties of the remnant and reconstructed quasi-projectiles together with the light fragments emitted in coincidence, while Chapter 7 reports the source reconstruction and their average properties as a function of centrality and beam energy for both the QPr and QPb channels. Finally, some conclusions are drawn.

Chapter 1

Physics case

Nuclear reaction are the only terrestrial tool to access the property of nuclei far from their standard conditions, in terms of chemical composition, excitation energy and density. On one side, they can be exploited to investigate the nucleus structure, by means of inelastic collisions or few nucleon transfer reactions, populating nuclei up to tens of MeV of excitation energy. On the other side, they can be used to create nuclear systems at higher excitation energy and far from the nuclear saturation density (0.16 fm^{-3}), allowing to explore the properties of the "ideal concept" of nuclear matter that is at the base of the description of astrophysical objects such as neutron stars [1].

The interaction mechanisms during an heavy ion collisions depends on several parameter and it is a complex quantum problem, related to the underlying interactions between the nucleons forming the projectile and the target. Among the various parameters, the available energy E_{beam}/A and the impact parameter b are usually used to give a classification of the various processes, as schematized in Fig. 1.1. Depending on the collision energy, a nucleon within the projectile may seen the target interaction as a mean field representing the collective contribution of all the nucleons, or it can experience single nucleon-nucleon collisions.

The mean field approach typically is valid below 20 AMeV. In this regime, the De Broglie wavelength ($\lambda = \frac{h}{mv_{rel}}$, where m is the nucleon mass and v_{rel} the relative velocity between projectile and target) associated with the relative motion of projectile nucleons relative to target nucleons is well above the average distance d between two nucleons within a nucleus (typically around 2 fm). This implies that the nuclei behave as a single entity, and the process is governed by collective behaviour rather than individual collisions. In this case, the interaction time may be relatively long ($\sim 10^{-20}$s), allowing for the achievement of complete chemical and thermal equilibrium. In central collisions, a highly excited and thermodynamically equilibrated source,

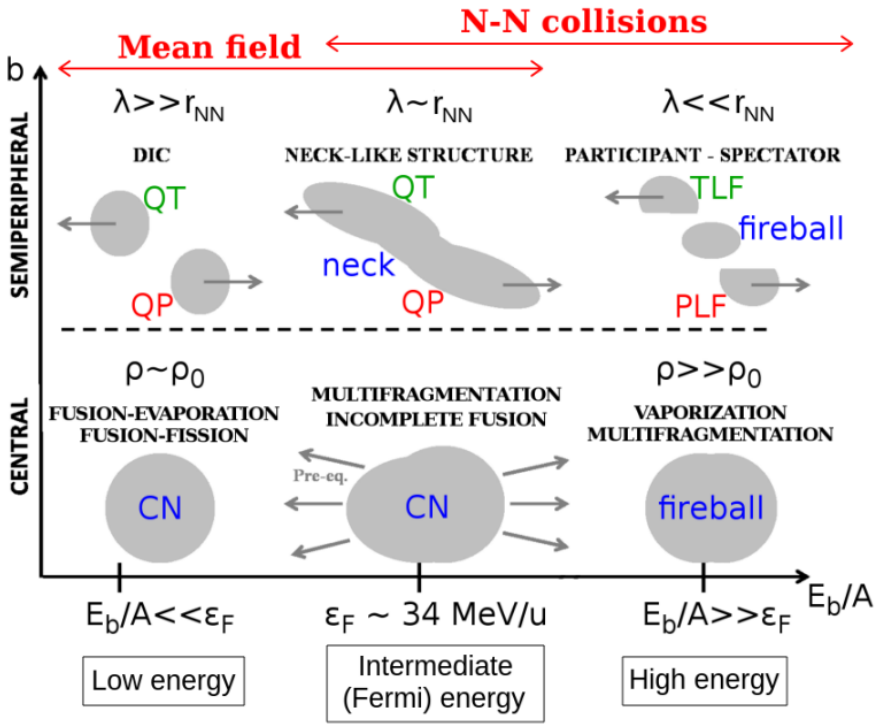

Figure 1.1: Schematic diagram of the possible evolutions of a heavy ion collision depending on bombarding energy per nucleon (E_b/A) and impact parameter b.

known as the Compound Nucleus (CN), can be formed through the fusion of both projectile and target, losing memory of the entrance channel. The CN subsequently de-excites via statistical decay processes such as particle and gamma-ray emission or fission. In semi-peripheral collisions, the Deep Inelastic Collisions (DIC) dominate, where only a portion of the available energy is transferred to internal degrees of freedom, and the reaction products retain memory of their initial characteristics. This leads to the emergence of two heavy fragments in the exit channel: the quasi-projectile (QP) and the quasi-target (QT).

Conversely, at high energies (above 100 AMeV), the De Broglie wavelength is much smaller than the average nucleon distance. Here, nucleon-nucleon collisions dominate and the collective effects become weaker. In fact, the kinetic energy transferred to the nucleons is high enough to let them reach a single particle free state: the Pauli exclusion principle has less effect and the nucleon-nucleon interactions become predominant. In this case, the semiperipheral reactions can be schematized with the so called participant-spectator

picture. In this scenario, the participants, i.e. the nucleons of the overlapping region, form a "fireball" of dense hot nuclear matter which undergoes vaporisation or multifragmentation, emitting highly energetic nucleons. The spectator remnants are less excited fragments and decay by statistical evaporation or multifragmentation. In central collisions, phenomena as complete vaporization or multifragmentation may occur.

The region of the intermediate energies, typically between 20 to 100 AMeV, is called "Fermi region". In this energy domain, the de Broglie wavelength is comparable to the average distance between nucleons within nuclei. As a result, it represents a transition region where both the mean-field interaction and nucleon-nucleon collisions play significant roles in determining the reaction dynamics, and features typical of both the low and high energy domains coexist. In this regime, the interaction timescales are shorter than at low energies (below 10^{-21}s) and the energy density can become quite large; as a result the system may not achieve full equilibration of its internal degrees of freedom. On one hand, a significant fraction of the available energy can be thermalized during the reaction, enabling the formation of hot nuclei; on the other hand, a substantial portion of the available energy may not be thermalized, leading to prompt emission of particles before full thermalization. This phenomenon is known as pre-equilibrium emission. A general overview of the "topology" of the various reaction mechanisms observed at intermediate energies as a function of centrality can be obtained by inspecting the invariant centre of mass velocity plots of the emitted products, as shown in Fig. 1.2 (adapted from [2]). The figure displays typical examples of invariant cross section plots for protons (upper row) and α particles (lower row) for different centrality bins. The abscissa and ordinate represents the velocity components parallel ($v_{\parallel}$) and perpendicular ($v_{\perp}$) to the beam direction, respectively, while the variable in the third axis represents the corresponding cross section. For the most peripheral collisions (left panels), the binary character of the exit channel is evidenced by the two well-defined circular emission patterns arising from particle evaporation from the QP and QT sources. In fact, in the reference frame of each emitter, the energy spectrum of the evaporated particles exhibits a Maxwellian-like distribution, with a pronounced maximum around the Coulomb barrier corresponding to a given velocity. This produces the typical circular pattern, commonly referred to as Coulomb circles, which can be clearly distinguished in the plots. It is worth noting that an enhancement of particle yields appears in the midvelocity region between the two main fragments ($v_{\parallel} \sim 0$). Such an effect is peculiar of this energy regime: a connection region between projectile and target may form during the collision due to the interplay between the mean field and the nucleon-nucleon collisions. As a consequence, particle and fragments emitted

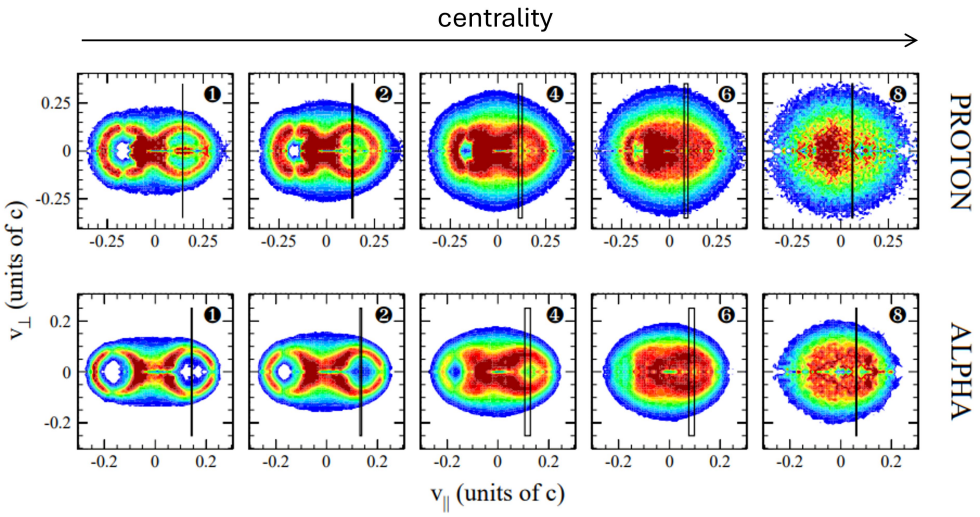

Figure 1.2: Invariant cm velocity plots ($v_{\parallel}$,$v_{\perp}$) for protons (upper row) and α particles (lower row) for Xe+Sn collisions at 50 AMeV for different bins of centrality, which increases from left to right. Adapted from [2].

from this region better preserve characteristics ascribable to the dynamics, thus they are a good probe to investigate the nuclear force. As the collisions become more central (moving from left to right panels), the binary character of the exit channel is less and less evident, until only one central emission source can be found. Therefore, depending on the reaction centrality, two big categories of events can be identified: the peripheral and semi-peripheral collisions where a quasi-projectile and a quasi-target are produced and the central collisions whose outcome evolves with the bombarding energy from incomplete fusion to multifragmentation or vaporization of the central source.

In this work the study of the ^{58}Ni+^{58}Ni reaction at 32, 52 and 74 AMeV is presented, focusing on the reaction dynamics of the peripheral and semiperipheral collisions. Therefore, more details about this collision category will be given in the next section.

1.1 Reaction dynamics in semiperipheral collisions at Fermi energies

As already described, the cross section of semiperipheral reactions at Fermi energies is largely dominated by the binary channel, where the formation of a quasi-projectile and a quasi-target, with kinematic properties close to those

of the initial colliding nuclei, is observed together with some Light Charged Particles (Z=1,2) and Intermediate Mass Fragments (3≤Z≤7). A characteristic feature of these collisions is the enhancement of yields at velocities intermediate between those of QP and QT. This is not limited to LCPs, as shown in Fig. 1.2, but is particularly evident for IMFs [3].

Various arguments and models have been proposed to explain the enhancement of particles at intermediate velocities experimentally observed in many studies [2–8].

In Refs. [9, 10], the authors propose to ascribe such an effect to the Coulomb repulsion of neighbouring reaction products. Such a description, also known as Coulomb proximity effect, affects the angular distribution of statistically evaporated particles. In fact, in the early stages of the collision, when the two partners are still close in space, the Coulomb field of the target may influence the evaporation from the QP and vice versa, leading to an asymmetric angular distribution. In Ref. [10] the observed emission pattern of α particles in the ^{28}Si+^{112}Sn reaction at 50 AMeV is shown to be compatible with a fast ($<10^{-22}$ s) statistical emission from the excited QP and QT, whose electric fields mutually perturb the particle trajectories. However, the question of how much this spatial asymmetric emission toward midvelocity can be accounted for by only Coulomb proximity is so far not clear. In fact, the effect is expected to be sizeable for heavy systems and less significant for relatively light systems, such as the one studied in this work. As described in Ref. [4], calculations performed with the statistical code SIMON, assuming a purely binary scenario, for the ^{36}Ar+^{58}Ni reaction at 74 AMeV indicate that the Coulomb proximity affects less than the 5% of the statistical emission, suggesting that this effect cannot be entirely excluded in our system, but other effects such as dynamical contributions should play the dominant role to explain the yield enhancement at midvelocity.

The dynamical scenario involves the development of a neck-like structure between the rotating di-nuclear systems. The nuclear matter in this neck region it is expected to be diluted, while the two main partners are supposed to remain close to the ground-state saturation density [11]. A qualitative illustration of the mechanism is given in the first panels of Fig. 1.3, taken from Ref. [12], where the results of a Boltzmann Nordheim Vlasov transport model are shown. Density contours, plotted for a semiperipheral collision ^{124}Sn+^{124}Sn at 50 AMeV at various times, show the developing in the overlap region of a neck structure that during the interaction time (80-120 fm/c) heats and expands still remaining in contact with the denser and colder regions of QP and QT. The rupture of the neck, at about 140 fm/c, due to its thermo-mechanical instabilities, may be at the origin of IMFs and LCPs emitted at mid-velocity, as experimentally observed and predicted by various

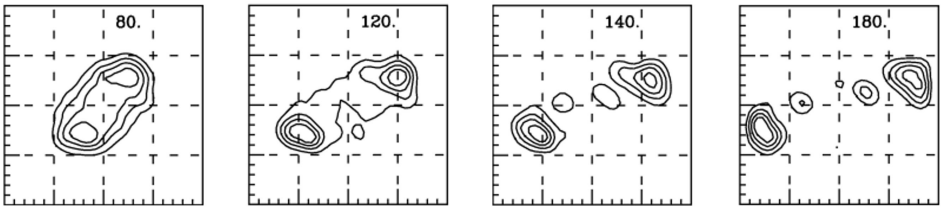

Figure 1.3: BNV calculation of density contour plots for a semiperipheral ^{124}Sn+^{124}Sn reaction at 50 AMeV, at several time instants (fm/c). Adapted from [12].

transport models [2–8, 13–20]. The size, the breaking time, the excitation energy and other characteristics of the neck are of course strongly influenced by the impact parameter, as well as on the beam energy and the initial size of the nuclei. Also the fluctuations of the degrees of freedom are large and thus the neck evolution can vary much from event to event. It must be noted that, by analogy with the participant-spectator picture at higher energies, the neck can be seen as the part of matter which participates in the collision process and therefore could be viewed as a "hot spot" whose properties can be different on average from those of the rest of the system.

The neck rupture can be seen as a limiting case of a more dissipative mechanism that can cause the dynamical fission of the QP and/or QT [6, 21–25], which, in general, represents a less favourable process with respect to their decay by means of particle evaporation. Unlike statistical fission, which is a slow process governed by equilibrium conditions, dynamical fission is a fast process, with a time scale of the order of $\sim$ 200 fm/c. The resulting fragments typically exhibit a mass asymmetry and are often aligned along the separation axis, with the lighter fragment preferentially emitted backward, toward the centre of mass of the system [6, 21–27]. A common interpretation of these observations is that the interacting di-nuclear system, by fluctuation, can produce two highly deformed nascent QP and QT connected by the neck region. The instabilities generated by the interaction drive the system to the neck rupture, producing two deformed fragments, as shown in Fig. 1.4. Because of the deformation and the angular momentum, the QP and QT are likely to undergo a prompt breakup, leading to the production of two fragments referred to as Light Fragment (LF) and Heavy Fragment (HF). If still excited, both fragments may subsequently decay through statistical evaporation. Of course this event type can involve the QP or the QT also as a function of their size. In symmetric systems, it is expected to occur with equal probability for both partners.

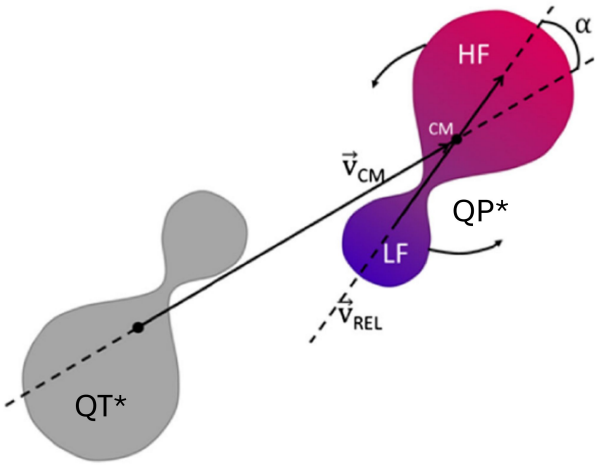

Figure 1.4: Illustration of the rotation of the strongly deformed QP (and QT) before its breakup. The α angle is also shown (see text for details). Adapted from Ref. [28].

In the literature to examine these decays, there are frequent references to the α angle [28–34], i.e. the angle between the QP-QT separation axis and the QP fission axis (see Fig. 1.4), defined as:

$$\alpha = \arccos\left(\frac{\mathbf{v}_{QP} \cdot \mathbf{v}_{rel}}{|\mathbf{v}_{QP}| \cdot |\mathbf{v}_{rel}|}\right) \tag{1.1}$$

where $\mathbf{v}_{QP}$ defines the direction of the QP velocity and $\mathbf{v}_{rel}$ defines the direction of the relative velocity between the breakup fragments. The $\cos(\alpha)$ distributions can give insight into the statistical or dynamical origin of the breakup. In fact, for statistical processes one expects an isotropic distribution since it does not preserve the memory of the entrance channel and of the QP-QT separation axis. On the contrary, dynamical fissions occur in preferentially aligned HF-LF configurations, with the LF emitted backward, as the highly elongated and deformed QP is expected to break apart on a short timescale along the QP-QT separation axis. This is evident in Fig. 1.5, adapted from Ref. [28], where the angular distribution $\cos(\alpha)$ for a pair of breakup fragments is shown. According to the interpretation proposed above, the peak at $\cos(\alpha) = 1$ is consistent with a dynamical decay.

In addition to these effects, another type of dynamical emission is the pre-equilibrium emission. These fast emissions can occur during different stages of the reaction whenever a non-thermalized source is present, such as the hot and deformed interaction region or a QP/QT that has not yet reached equilibrium. During these early stages of the reaction, some nucleons or

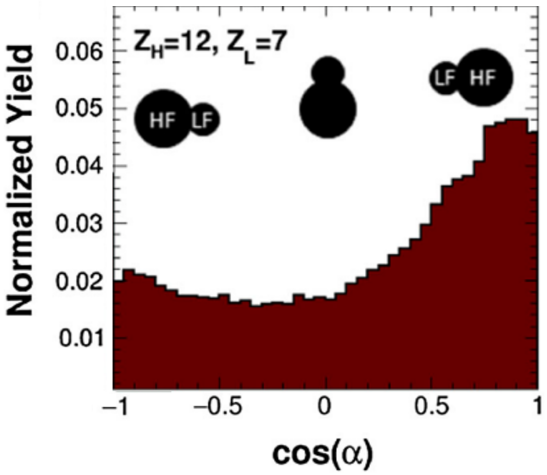

Figure 1.5: Normalized angular distributions for breakup fragments with Z_{HF}=12 and Z_{LF}=7. Emission of the LF in the backward direction corresponds to $\cos(\alpha) = 1$. Adapted from Ref. [28].

light clusters may suffer nucleon-nucleon collisions that push them "outside" the attractive potential of the bulk. This phenomenon mainly includes free nucleons and is more significant in central collisions [35, 36]. These particles, keeping memory of the entrance channel, are preferentially emitted along the moving beam axis.

Gaining information on the dynamical phase from an experimental point of view is challenging, since only the secondary fragments, i.e. those observed after the statistical de-excitation, can be detected. The detection takes place nanoseconds after the collision, corresponding to timescales extremely longer than those of the reaction. As a consequence, the features of the primary sources must often be inferred through simulations and/or sophisticated experimental event analyses which attempt their reconstruction. Nevertheless, a well-established experimental signature of the dynamical nature of mid-velocity emission is their neutron enrichment [2, 5, 8, 15, 17, 37–40], as described in more details in Section 1.1.1, which can be interpreted within the framework of the nuclear Equation of State (nEoS).

In the following section, this experimental evidence and its theoretical interpretation will be summarized. Finally, a description of the primary source reconstruction methodology and their properties will be illustrated.

1.1.1 The neutron enrichment of the neck and the isospin drift phenomenon

From a theoretical point of view, the neutron richness of the matter produced in the neck region observed experimentally [2, 5, 8, 15, 17, 37–41] can be explained in the framework of the nuclear Equation of State and the isospin transport phenomena.

The nEoS aims at the description of the behaviour of nuclear matter in terms of thermodynamic observables such as density, temperature, excitation energy per nucleon, pressure, volume and isospin (i.e. N/Z). Its relevance lies in its implications in a wide range of physical phenomena, from the ground state properties of nuclei to the dynamics of astrophysical systems such as core collapse supernovae and neutron star mergers [42–48].

The nEoS is aimed at describing the energy per nucleon of a nucleus far from ground state conditions (T=0 MeV and ρ=0.16 fm^{-3}), which can be expressed as a function of the nuclear density $\rho = \rho_n + \rho_p$, where ρ_n and ρ_p are the neutron and proton densities, and the isospin asymmetry parameter $\delta = \frac{\rho_n - \rho_p}{\rho}$:

$$\frac{E}{A}(\rho, \delta) = \frac{E}{A}(\rho, \delta = 0) + \frac{E_{sym}}{A}(\rho)\delta^2 \tag{1.2}$$

The first term corresponds to the symmetric nuclear matter, whose behaviour around and far from the saturation density has been well constrained through nuclear structure studies [48]. The coefficient of the second term, commonly referred to as the symmetry energy, corresponds to asymmetric nuclear matter and represents one of the major open questions in nuclear physics. Typically, it is expanded in a Taylor series around the saturation density. By comparing experimental observations with theoretical predictions, the coefficients of this expansion can be constrained. A comprehensive overview of the current state of knowledge on the symmetry energy is provided in [49].

During heavy-ion collisions, the symmetry energy rules the exchange of neutrons and protons between the two colliding nuclei, i.e. the so called isospin transport phenomena. Protons and neutrons experience different forces due to their respective chemical potentials [11], and, in the presence of isospin ($\Delta\delta$) and/or density ($\Delta\rho$) gradients, the difference between neutron and proton currents $j_n - j_p$ can be written as:

$$j_n - j_p \propto \frac{E_{sym}}{A}\nabla\delta + \frac{\partial E_{sym}/A}{\partial\rho}\delta\nabla\rho \tag{1.3}$$

where two contributions can be distinguished. The first term, the isospin diffusion, is driven by asymmetry gradients and acts to relax any neutron-proton unbalance. Isospin diffusion has been experimentally highlighted and

quantified for many years in asymmetric reactions [8, 20, 39, 41, 50–60]. The second term, the isospin drift, is driven by density gradients and induces a net neutron flux towards low density regions. The isospin drift is thus expected to be responsible of the neutron enrichment of the neck region observed in the midvelocity emissions due to the density gradient that would develop between the neck and the quasi projectile/target region. Since the drift mechanism does not require an initial isospin asymmetry between projectile and target, it can be studied separately from the isospin diffusion process by choosing symmetric reactions, such as the ^{58}Ni+^{58}Ni system studied here.

Within this interpretation the isospin drift is strictly related to the reaction dynamics because its occurrence is started by the production of region at sub-saturation density during a collision. Therefore, generally speaking, the isospin drift is basically ruled out at low beam energy because no diluted regions can be achieved. Instead, with increasing beam energy, compression-expansion phases can be expected; these phases, their duration and the portion of the interacting system that may be involved depend on two other parameters, namely the impact parameter and the size of reacting nuclei.

From an experimental point of view, the neutron enrichment of the midvelocity emission is usually investigated by studying the isospin content (N/Z or related observables) of fragments as a function of their emission pattern: particles emitted forward (backward) with respect to the QP (QT) are mainly associated with statistical evaporation, whereas the intermediate velocity region is populated by a superposition of QP and QT statistical emissions together with fragments originating dynamically from the neck. Despite the difficulty associated to the full disentanglement between statistical and dynamical emissions, the neutron enrichment effect has been clearly highlighted in several studies [5, 15, 19, 39–41].

An example is shown for the ^{80}Kr+^{40}Ca at 35 AMeV reaction in Fig. 1.6, taken from Ref. [40]. In this figure, some isobaric (t/^{3}He, ^{7}Li/^{7}Be and isotopic (d/p, t/p, ^{7}He/α) yield ratios are presented for fragments emitted forward and backward with respect to the QP, using the parallel velocity along the beam axis v_{par} with the conditions $v_{par} > v_{QP}$ and $0 < v_{par} < v_{QP}$, respectively. Considering that the backward emitted fragments, more sensitive to the midvelocity emission, are more neutron rich than those forward emitted, an isospin drift effect is highlighted.

In other works [2, 3, 37], attempts to achieve a more complete separation of these two components have been proposed.

The neutron enrichment of the neck may influence the properties of the primary QP*/QT*, and, consequently, a correlation between the neutron excess of the midvelocity fragments and the corresponding neutron depletion of the QP remnant could be expected [28, 30, 59, 61, 62]. This effect can

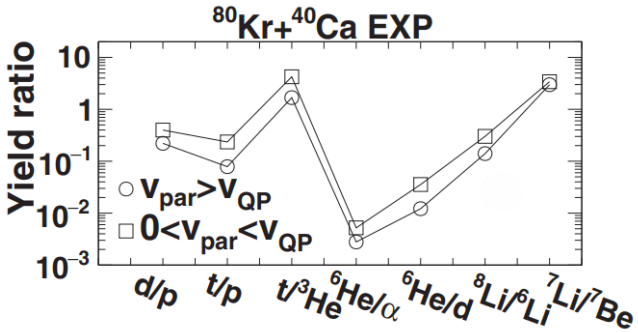

Figure 1.6: Isotopic and isobaric yield ratio of light fragments (Z¡5) forward (circles) and backward (squares) emitted with respect to the QP reference frame. Data refer to the ^{80}Kr+^{40}Ca reaction at 35 AMeV. Taken from Ref. [40].

be seen in Fig. 1.7, taken from Ref. [61], where Thériault at al. for the ^{58}Ni+^{58}Ni reaction at 52 AMeV, after separating the midvelocity and the evaporative components, compared the isospin content of the reconstructed QP* with that of the midvelocity fragments as a function of centrality estimator $Z_{proj} - Z_{QP}$. [62]. They observed a lower N/Z ratio of the QP* with respect that of the initial system (1.07), which decreases with centrality while that of the midvelocity component slightly increases. Although the N/Z of the midvelocity component for the same reaction will be discussed in Chapter 7, a direct comparison with those results is not possible. In that study, the isospin estimation also included free nucleons, whereas in the present work, due to the strong assumptions required for estimating free neutron emission, only clusters are considered. For the same reason, the isospin content of the QP* will not be directly investigated. Nevertheless, conclusions on the role of the midvelocity emission in determining the isospin of the primary QP* will be drawn.

1.2 The source reconstruction

As discussed, the secondary fragments, i.e. those directly detected, can be produced by different sources, both statistical, as the evaporation of the primary QP*/QT*, or dynamical, such as the midvelocity and the pre-equilibrium emission. The disentanglement of particles coming from these different emitting sources allow the reconstruction of their characteristics, which are of particular interest since are more directly related to the dynamics of the reaction.

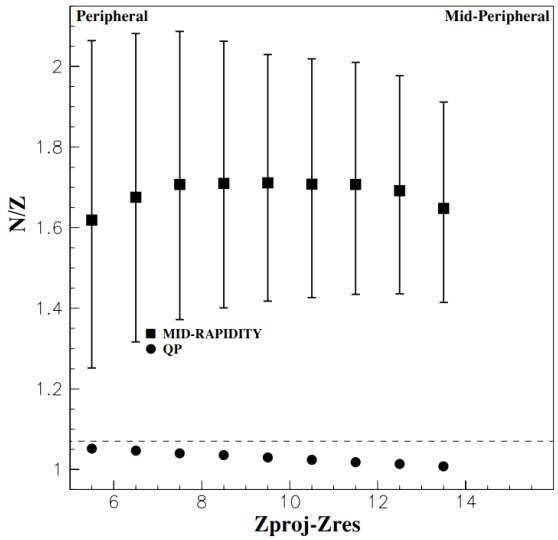

Figure 1.7: N/Z of reconstructed QP* (dots) and midvelocity emission (squares) for the reaction ^{58}Ni+^{58}Ni at 52 AMeV as a function of the charge difference between the projectile and the residue. The dotted line shows the original N/Z of the projectile and target (1.07). Adapted from Ref. [61].

Several attempts and various strategies have been proposed for this purpose [2–4, 37, 61–64], starting from the detection of nearly complete events, obtained either with 4π detectors [2, 4, 37, 61, 62] or through corrections for detection inefficiencies based on simulations [3, 63]. Moreover, a reliable estimate of the impact parameter is required, as it plays a crucial role in characterizing the reaction dynamics.

A critical point in this reconstruction procedure is how to take care of the free neutrons, which are usually not detected. A possible approach for the neutron emission estimation is based on the difference between the original QP and the number of bounded neutrons. For this procedure, the isotopic identification of the charged particles is mandatory. Then, with specific assumptions, it is possible to attribute them to the different sources.

For charged particles, directly measured, the contributions coming from the different sources can be separated by means of their characteristics.

One of the possible approach for the separation of the yields of midvelocity and evaporative components is proposed in [3, 63] and it will be used in this work. In Fig. 1.8, this method is applied to recognize the evaporative nature of α particles emission. In the left panel, the experimental yields in the ($v_\perp$,$v_\parallel$) plane for a given centrality selection are shown. Considering only the particles emitted forward with respect to the centre of mass ($v_{cm} > 0$),

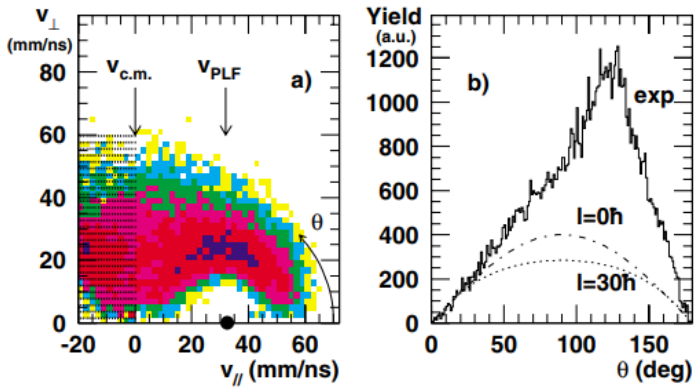

Figure 1.8: Left panel: experimental yields of α particles for a given centrality, in the ($v_\perp$,$v_\parallel$) plane. Right panel: Corresponding angular distribution in the QP frame (histogram) and results of simulations for an evaporating source with spin $0\hbar$ and $30\hbar$ (dashed and dotted lines). Taken from Ref. [63].

which are more related to the QP phase space, the angular distribution in the QP reference frame can be obtained (right panel). Assuming that the evaporative component, expected to follow a $\sin(\theta)$ distribution for a source with non-zero spin, can be reliably estimated from the most forward angles, the midvelocity yield can then be evaluated as the difference between the total angular distribution and the $\sin(\theta)$ one. In the case of a source with non-zero spin, the distribution of evaporated particles tends to become flatter (as shown for $l = 30\hbar$ in the right panel). However, the $\sin(\theta)$ distribution remains a good approximation for sources with low spin. It should be noted that this technique does not allow one to distinguish possible contributions from pre-equilibrium emissions.

Concerning the excitation energy of the primary sources, the method of nuclear calorimetry, which relies in the measurement of the kinetic energies of the emitted particles, can be used.

Another approach used to point out the yields and the apparent temperatures of different sources is the moving source fit applied to the kinetic energy spectra of the emitted particles, assuming Maxwellian distributions [4, 55, 64, 65]. This method can be used to characterize all the different sources: primary QP*/QT*, the midvelocity and also the pre-equilibrium. However, two main issues arise: first, the source velocity cannot be easily identified or assigned; second, assuming a Maxwellian emission implies a nuclear temperature and thus internal equilibrium, an assumption that becomes questionable for the dynamical emissions. The temperature concept is more

reasonable when applied to QP*/QT* sources, for which the typical apparent temperatures estimated are below 3-5 MeV and show a clear dependence on centrality: nuclei are only weakly excited in peripheral collisions, while their excitation energy increases at smaller impact parameters. Despite the limitations discussed above, in Ref. [65] an apparent temperature associated with pre-equilibrium emission was estimated to be around 10 MeV, while in Ref. [64] an apparent temperatures of ∼15 MeV has been estimated for the midvelocity component, which appear almost independent of centrality. These temperatures are consistent with dynamical emissions predominantly originate from nucleon-nucleon interactions.

In conclusion, the reconstruction of the emitting sources represents a very interesting topic, approached in the literature mainly in the QP-QT binary channel. In recent years, increasing attention has also been devoted to the quasi-projectile breakup [28, 30, 33]. However, to the best of our knowledge, very rare and not complete attempts has been made to reconstruct the characteristics of the primary sources in this channel [24].

Chapter 2

The INDRA-FAZIA experimental apparatus

INDRA and FAZIA are multidetector arrays designed for the detection of charged particles produced in heavy ion collisions in the Fermi energy domain (20-100 AMeV). INDRA is a 4π multidetector array developed at GANIL (Caen, France) in the 1990s, while FAZIA is a modular array which represents the state-of-the-art for the detection of charged particles, thanks to its unprecedented Z and A identification capabilities. Since 2019, twelve blocks of FAZIA have been coupled with the INDRA multidetector to combine the extensive angular coverage of INDRA with the excellent identification performance of FAZIA at forward angles.

This chapter presents an overview of the INDRA and FAZIA apparatuses and their coupling. The last section is dedicated to description of the particle identification techniques employed in this works, namely the ΔE-E and the Pulse Shape Analysis (PSA) methods.

2.1 FAZIA

FAZIA (*Forward-angle A and Z Identification Array*) is a multi-detector array [66, 67], designed to be a modular and transportable detector so that it can be used in different laboratories and easily coupled with other experimental setups.

The basic module of FAZIA, called "block", consists of 16 three stage ΔE-E telescopes, each made of two silicon detectors followed by a CsI(Tl) crystal. The Front End Electronics (FEE) associated to each block is placed under vacuum, close to the detectors, resulting in a total block length of about 80 cm, as shown in Fig. 2.1. This choice minimizes signal distortion and the elec-

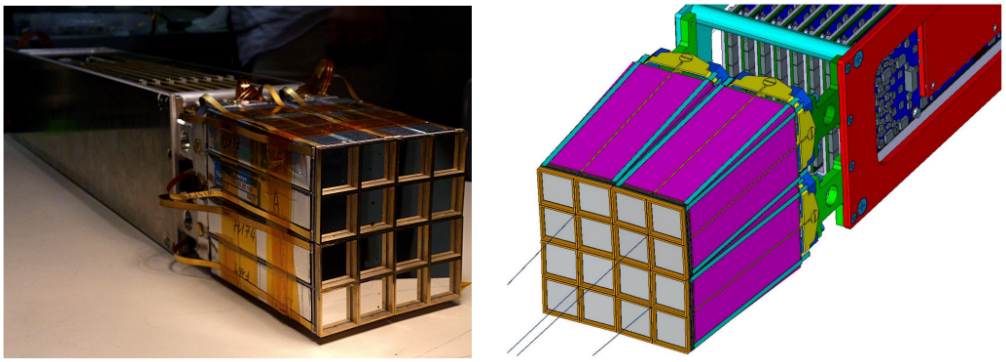

Figure 2.1: Picture (left) and schematic rendering (right) of a FAZIA block, showing the silicon detectors, the CsI(Tl) crystals and the Front End Electronics. Taken from [68].

tronic noise, while also reducing the connections needed between the vacuum chamber and the outside, thereby enhancing the modularity and portability of the setup. In fact, in this way, each block needs only 3 connections: an optical fiber for I/O, a 48 V power supply cable, and a water-cooling line to dissipate the heat produced by the electronics operating under vacuum. Considering that one block corresponds to 48 detectors, the ability to operate with such a large number of detectors using only three connections represents a remarkable simplification compared to more conventional detector systems.

2.1.1 The detectors

As already introduced, the basic unit of the FAZIA apparatus is a three stages telescope:

- The first layer is a silicon detector (Si1) with a thickness of 300 μm. Its active surface is 20×20 mm^2. These detectors are mounted on a 2×2 holding frame made of an aluminum alloy [67], as shown in Fig. 2.2.

- The second layer is a silicon detector (Si2). The standard thickness of these silicon detectors is 500 μm. However, during recent experiments, these Si2 were used only for the outer blocks. Indeed, to better cope with the higher bombarding energy, thicker silicon detectors (750 μm) were used for the four inner blocks. The second stage silicon detectors are mounted on a frame similar to that employed for the first stage.

- The third layer is a Cesium Iodide (CsI) scintillator doped with Thallium 10 cm thick, followed by a photodiode to collect the light. The

crystal is a parallelepiped, slightly tapered to match the designed distance from the target of 1 m. The front face of the scintillator is covered with a reflective alluminazed Mylar foil (~ 1.5 μm thick), while the lateral wrapping consists of a highly reflective (98%) polymer foil (ESR Vikuiti, 3M).

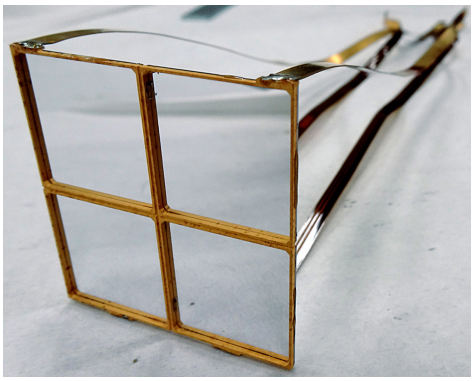

Figure 2.2: Holding frame with mounted silicon detectors. The kapton flexi cables, needed to connect the detectors to the Front End Electronics are soldered to the metal and μ-bonded to the silicon pads. Taken from [67].

The silicon and CsI(Tl) detectors are coupled in "quartets", each formed by 4 telescopes. The quartets are in turn arranged in a 2x2 matrix, thus forming a full FAZIA block.

The current design of the FAZIA detector is the result of a long R&D activity aimed at the optimization of their performance [66]. In particular, the goal was the improvement of their energy resolution and their identification capabilities obtained with ΔE-E and PSA techniques. As discussed in details in [66], the FAZIA collaboration has established the so-called "FAZIA recipe", which is a set of characteristics of the silicon detectors needed to ensure excellent performance. In particular, it is important to consider the following properties:

- "Random" cut of the silicon wafers which should be tilted with respect to the major lattice direction to reduce the channelling effect. This effect, related to the crystal orientation, influences the interaction of the particles with the silicon. In fact, if an impinging particle has a direction close to that of the major axis of the lattice, it tends to pass, on average, farther from the lattice atoms, experiencing a weaker interaction. This can introduce fluctuations in the stopping power, spoiling the energy resolution. Moreover, the channelling effect also

affects the particle range and, consequently, the shape of the signal [69], which strongly impacts the identification capability of the PSA. Therefore, to minimize this effect, the wafer are sliced from the ingot following specific cutting prescriptions.

- Usage of silicon detectors with high doping uniformity. This feature, which is necessary to have a uniform electric field in the depletion region of the detector, is mandatory for achieving good result with the PSA when using single pad detectors. In fact, the shape of the signal depends on the time development of the charge collection, which is strongly affected by local inhomogeneities of the electric field. Consequently, a non-uniform electric field leads to a signal shape that, for the same impinging particle, will depend on the impact position, thus compromising the identification performance of PSA. Although the voltage applied to the silicon junction is the same, the local resistivity, which is connected to the local doping concentration, can change across the detector, spoiling the PSA performance. For such a reason, the FAZIA collaboration uses silicon detectors with the highest possible doping homogeneity. Initially, this was guaranteed by the neutron Transmutation Doped (nTD) technique. However, when this production method became unavailable, Ultra-homogeneous High Purity Silicon (UHPS) detectors were adopted. Given the impact of doping homogeneity on the PSA performance, the FAZIA collaboration has developed a non-destructive method [69], based on scanning the detector using collimated UV-light pulses, to measure the resistivity distribution as a function of the position. Although not all detectors have been tested, the UHPS standard ensures resistivity distributions with a FWHM of about 3-6%, comparable to those obtained with the nTD silicon detectors. This ensures that the full FAZIA apparatus achieves PSA identification capabilities comparable to those reported in [70], as verified for the first time and discussed in detail in Appendix A.

- Selection of silicon detectors with high thickness uniformity. This feature is mandatory to obtain good identification performance in the ΔE-E technique: the high thickness homogeneity reduces the dependence on the impact position of the ΔE released by a particle. FAZIA silicon detectors have a thickness uniformity better than $\pm$ 1 %.

- Reverse mounting configuration of silicon detectors, so that the particles enter from the low-field side. In this way it is possible to enhance the PSA identification performances, without affecting the ΔE-E method [71].

- An aluminium layer of $\sim$ 30 nm on both sides of the detectors. This reduce the sheet resistance preserving good timing properties, without affecting the energy resolution for the straggling effect.

- Constant monitoring of the silicon detector reverse current. This allows for the compensation of the voltage drop over the bias resistor, in order to keep constant the electric field inside the detectors during the whole experiment. The constancy of the electric field is necessary to ensure that the shape of the signal induced by particles with same Z, A and energy remains unchanged throughout the experiment.

- Minimization of dead layers in order to reduce the energy straggling.

On-board electronics are also a distinctive feature of FAZIA, which we will now describe briefly.

2.1.2 The electronics

One of the main characteristics of the FAZIA apparatus is the integration of its electronics directly inside the vacuum chamber, as close as possible to the detectors. The full description of the FAZIA electronics can be found in [67]. Here, only a brief overview is presented. In Fig. 2.3 a schematic view of the electronics is shown, where one can distinguish the Front-End Electronics card and the "service" cards (Block card, Power Supply and Half-Bridge), all connected via a backplane.

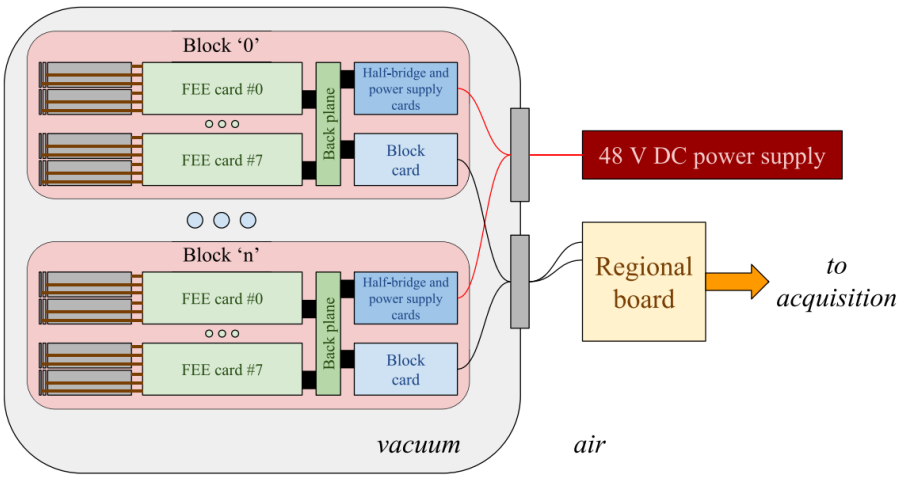

Figure 2.3: Schematic representation of the FAZIA electronics inside and outside the vacuum chamber. Figure taken from [67].

Each FEE cards, directly connected to the detectors with flexi cables, serves two FAZIA telescopes (6 detectors) providing the pre-amplifier stage in the first part, the digitizing and signal processing in the central part, and the high voltage generation and controls in the last part, as shown in Fig. 2.4.

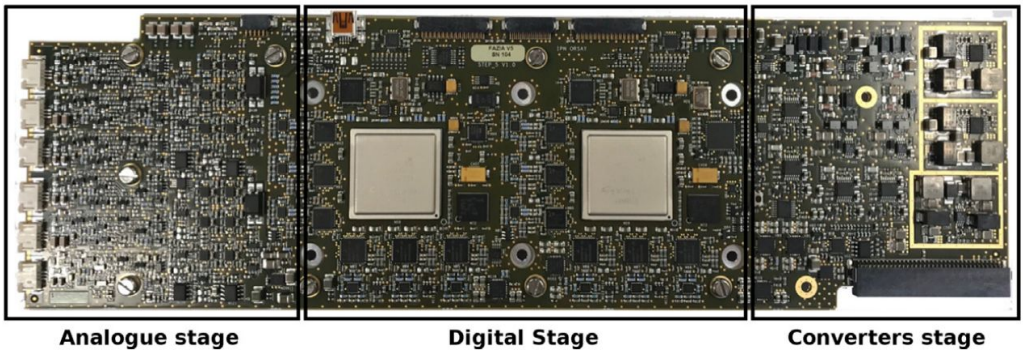

Figure 2.4: Picture of a Front-End Electronic card. The three stages (analogue, digital and converters) of the board are highlighted. Figure taken from [67].

In particular, concerning the analogue stage, each front-end card hosts six charge sensitive preamplifiers, one for each detector of the two telescopes connected to the FEE card. Their output dynamic range is 8 V, which must be adapted to exploit the available dynamic range of the following sampling ADCs. The number of sampling ADCs is larger with respect to the number of pre-amplifiers since some of signals are split. In particular, the Si1 pre-amplifier signal is used with two different dynamic ranges (QH1 and QL1 in the following) and it is also analogically differentiated to obtain the corresponding current signal (I1), used for PSA purposes. Also the Si2 signal (Q2) is analogically differentiated to generate the current signal I2, while the CsI(Tl) signal (Q3) is the only one that is directly sampled. Of course, all the signals described above pass through an anti-aliasing filter before being sampled by the ADCs.

The digital stage consists of twelve ADCs (six per telescope), with different sampling rate and characteristics. The QH1, Q2, and Q3 signals are sampled using 14-bit, 100 MS/s ADCs with a 2 V range and an effective number of bits (ENOB) of 11.4. The QL1, I1 and I2 signals are instead sampled by 14-bit, 250 MS/s ADCs (ENOB=11.2), with a 1.5 V input range. Note that the QH1 corresponds to the full range of the pre-amplifier, attenuated by a factor of 4 to match the 2 V range of the corresponding ADC, while the QL1 signal is obtained with an amplification factor of 3 and a full range of the

ADC of 1.5 V. Considering the different factors and range of the ADCs, the ratio between QH1 and QL1 signal is 16, allowing to have for less energetic particles a dedicated signal with higher sampling rate to apply the Time of Flight identification technique if needed. The twelve ADCs are read by two Field Programmable Gate Arrays (FPGA), one for each telescope, which perform a real-time digital filtering of the signals in order to obtain triggers and energy measurements from each detector.

Finally, the last stage of the FFE, the converters stage, generates the required bias voltages for the silicon detectors, up to 300 V for Si1 and up to 500 V for Si2, starting from the 48 V supply. In this stage also the automatic correction of the HV to take care of the reverse current is implemented.

By means of a backplane bus the FEE cards are connected with the three service cards, namely the Block card (BC), the Half-Bridge card and the Power Supply card. The Half-Bridge and the Power Supply cards provide and monitor the low voltages needed by the electronics. The Block card merges the data coming from one block and manages all the input/output operations, including slow controls, which have to pass through the Regional Board (ReBo). The Regional Board, which is the only part placed outside of the vacuum chamber, collects all the data coming from the Block cards and sends them to the acquisition system, handling also the slow control requests, the trigger information coming from the blocks and sends back validation signals. Moreover, it manages the coupling between FAZIA and other apparatuses allowing for the synchronization of various acquisition systems. Since the electronics operate under vacuum, an efficient cooling system is required. It consists of a copper plate, on which all the cards are screwed on and thermally coupled by means of a thermal grease. Inside the copper plate, there are channels which distribute a liquid (water with 30% alcohol or glycol) along the surface that holds the cards.

2.1.3 FAZIA trigger

The FAZIA trigger starts with the local triggers generated by the FPGA of the FEE cards by exploiting on-line fast trapezoidal shaping filters implemented on the QH1, Q2 and Q3 signals. The local trigger for each detector is produced when the maximum amplitude of the shaped signal is larger than a threshold ("fast threshold") that can be set by the user. Logic signals from Si1, Si2 and CsI are combined in the FPGA, usually in OR configuration, to build the local trigger for each telescope. Then, the local triggers reach the Block Card which counts the number of local triggers and sends the total to the ReBo every 40 ns. The global trigger is generated inside the ReBo when, integrating over a time window, the local triggers coming from all the

Block Cards overcomes the multiplicity threshold. If a downscale factor K is imposed, the global trigger is accepted once every K occurrences. Finally, the ReBO performs a check for any possible alerts generated by FEEs (such as nearly full FPGA data buffers). If an alert is present, a veto flag is issued; otherwise, the validation signal and an event number is distributed to all BCs and then to each FEE through the backplanes. A telescope is acquired when the amplitude of at least one of its detectors has passed the slow filter threshold. It's worth mentioning that FAZIA, when coupled with other detectors, can also work in the so-called slave mode. In this case, when an external trigger is received and the veto flag is false, a validation signal is generated.

2.1.4 Digital treatment of the signals

The FAZIA collaboration adopts both online and offline digital signal processing to extract energy and shape-related information from the digitized signals. As one can imagine, the online signal processing is, in principle, favourable because it allows to store only the extracted energy information, without the need to save the entire waveform, thus reducing both storage space and acquisition time. Unfortunately, not all the algorithms needed for digital processing can be implemented in the FPGA without a sizeable effect in the dead time. Typically, if a signal interpolation is needed, the time calculation is not compatible with on-line processing. For such a reason, only energy information, obtained through a trapezoidal shaping filter, is extracted in the on-line calculation. In particular, in addition to the filter needed for the trigger, there are also slower shaper for energy calculation on QH1, Q2 and two different filter for Q3 signal, the "fast" and "slow" filter in order to exploit the PSA on CsI(Tl). The rise-time and the flat-top values of the slow trapezoidal filters can be set by the user. Usually, the rise-time for the QH1 and Q2 shapers is 2 μs while the flat top is 1 μs. For the Q3 shapers, the rise-time is set at 2 μs, while the flat top at 10 μs for the slow filter and at 500 ns for the fast one. Concerning the PSA in silicon detectors, since many years, the FAZIA collaboration is using as PSA parameter the maximum of current signal. For such a reason, to overcome the limitation due to the 250 MHz of sampling rate, an interpolation of the I1 and I2 signal is needed and this can be done only off-line, starting from a portion of the signal containing the region of the maximum amplitude, stored by the acquisition. In fact, when a FEE card receives a validation signal, depending on the setting in slow controls, if needed, a portion of the different signals (QH1, QL1, I1, Q2, I2, Q3) and the processed online values are transferred to FIFO memories. At the same time, the acquisition thresholds, user adjustable, are

checked. If any of the energy shaped signals exceed its respective acquisition threshold, all the telescope signals are marked for acquisition. When a telescope is marked for acquisition, all its information is transferred to another FIFO memory, together with the event number provided by the ReBo, to build the local event. The local events from the FEE cards are collected by the respective Block cards, where the event number is also checked. The partial event thus built is written in the Block card FIFO buffer, ready to be read from the ReBo.

2.2 INDRA

INDRA (*Identification de Noyaux et Détection avec Résolutions Accrues*) is 4π multi-detector array for charged particles [72, 73]. The apparatus has operated since 1993 at GANIL for the study of heavy ion collisions at Fermi energies focusing mainly on the topic concerning the equation of state of nuclear matter. In its original configuration, shown in Fig. 2.5 it covered almost the 90% of the total solid angle thanks to 336 detection modules (telescopes) arranged in 17 rings with cylindrical symmetry with respect to the beam axis, covering polar angles from 2° to 176°. Moreover, it was

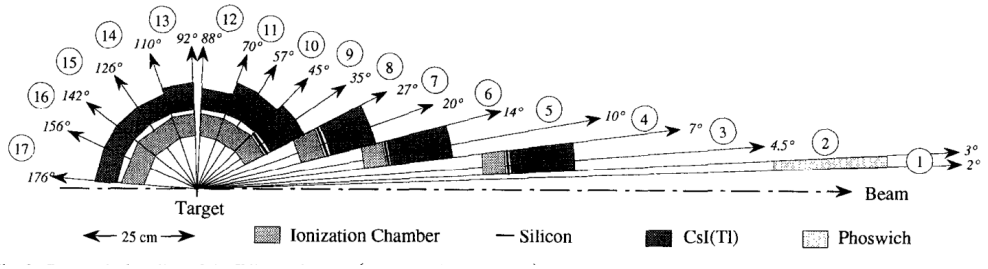

Figure 2.5: Original geometry of the INDRA apparatus (from [72]).

characterized by very low identification thresholds ($\sim$ 1 AMeV), achieved by using Ionization Chambers as first stage of the telescopes. Residual energies are measured by a combination of silicon (150 or 300 μm thick) and/or CsI detectors (5 to 14 cm in length) read out by photomultipliers, used as the second and/or third stage of the telescopes, depending on polar angle. In fact, the telescopes configuration depends on the ring:

- The ring 1 was originally made of phoswich detectors, later replaced by 12 Si-CsI(Tl) telescopes.
- The rings from 2 to 9 are three stage telescopes made of IC-Si-CsI(Tl).

- The rings from 10 to 17 are two stage telescopes made of IC-CsI(Tl).

In the last experiments, the Ionization Chamber stage has not been used and the particle identification has been achieved either by applying the ΔE-E method on the available detector layers, or the PSA in CsI(Tl). Since the beginning, no limitation has been observed in the charge identification, while concerning the isotopic identification a very important step has been done: in previous INDRA experiments the mass identification was limited to approximately Z∼4-6, whereas since 2022 (i.e. between the data-taking campaigns relevant to this work) the upgrade of the electronics from the original analog to a digital one, together with the replacement of some silicon detectors, has extended this upper limit up to Z∼10 [74]. It is worth noting that even with the new digital electronics, only the preamplifier stage is placed close the detectors, while the sampling stage is outside the vacuum chamber. More technical details are described in [74]. In conclusion, the overall identification performance of INDRA has been significantly improved (see Section 3.1). Moreover, the new electronics and DAQ system have drastically reduced the INDRA dead-time which is now comparable to that of FAZIA (10-15 μs), allowing for a much easier coupling between the two detector acquisitions.

2.3 The INDRA-FAZIA coupling

Since 2019, INDRA and FAZIA apparatuses have been coupled to maximize their performances: a large angular coverage guaranteed by INDRA and a very good mass identification in the forward region with FAZIA. A picture of the INDRA-FAZIA setup during the mounting operations can be seen in 2.6. In this configuration, 12 FAZIA blocks are organized in structure of 3 blocks to create a sort of forward wall between 1.4° and 12.6° placed at 100 cm from the target (which is located inside the INDRA apparatus). To permit the installation of FAZIA, the first five rings of INDRA were removed, thereby improving the isotopic identification of quasi-projectile-like fragments, which are predominantly emitted in the forward direction. The remaining INDRA rings (from 6 to 17) cover a wide angular range from 14° to 176°, corresponding to about 80% of the full 4π solid angle. This extensive coverage enables the reconstruction of global observables, such as light charged particle multiplicity or transverse energy, which are useful for estimating the reaction centrality.

Concerning the coupling of the DAQ systems of INDRA and FAZIA, it is implemented at three levels. At the trigger level, the two apparatuses operate in a common dead time mode. This is achieved by interconnecting their trigger and veto input/output signals, ensuring that neither FAZIA nor

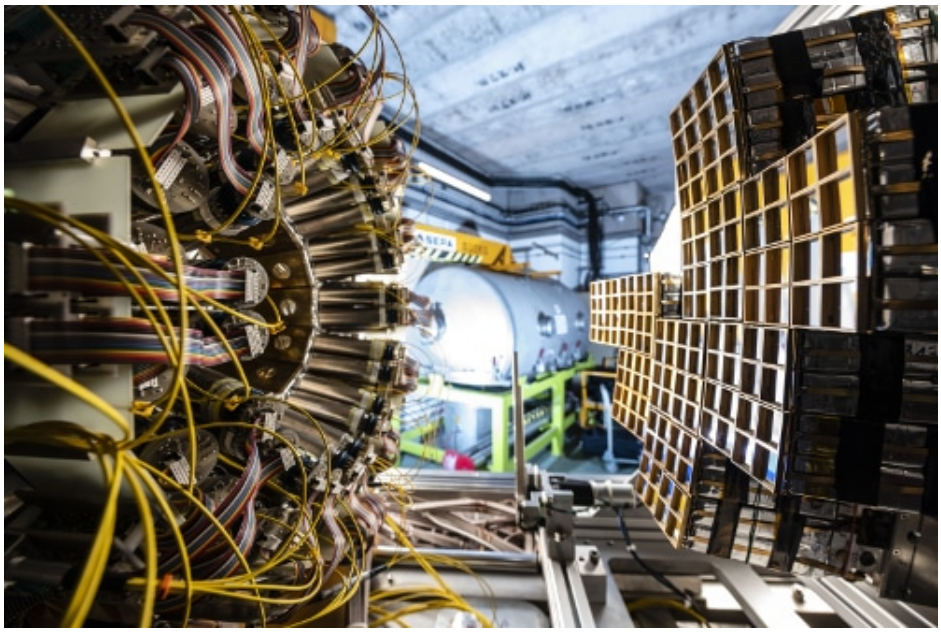

Figure 2.6: Picture of the INDRA-FAZIA apparatus during the mounting operations at GANIL (only 9 FAZIA blocks were mounted when the picture was taken). INDRA is the apparatus on the left side and FAZIA the one on the right side.

INDRA produce a validation signal while the other apparatus is not ready. The second level of the acquisition coupling consists in the generation of a common time stamp, based on the VXI CENTRUM (*Clock Event Number Transmitter Receiver Universal Module*) technology, developed at GANIL in the early 2000s. The CENTRUM is an absolute timestamp generator connected to both apparatuses, enabling precise synchronization between independent acquisition systems through event timestamp distribution. Finally, the third level is performed by NARVAL, an acquisition system developed by IPN Orsay (France). NARVAL collects data from both INDRA and FAZIA acquisitions and merges events whose timestamps differs by less than a coincidence window, producing global events containing information from both detectors. This system is designed to be as general as possible and it may also be used for coupling FAZIA with other detector arrays in future experiments.

2.4 Identification techniques

In this section, we recall the physical background of the identification methods possible with the INDRA-FAZIA apparatus, namely the ΔE-E method

and the Pulse Shape Analysis (PSA) in both Silicon and in CsI(Tl) detectors. In principle, the Time of Flight method identification technique [75, 76] could also be applied. However, this method will not be discussed here, as it was not used in the analysis of the data presented in this work.

2.4.1 ΔE-E method

The ΔE-E method is one of the most used identification techniques for charged particles in nuclear physics at Fermi energies. The ΔE-E technique relies on the fact that the stopping power of a material depends on the characteristics of the incident charged particle, as described by the Bethe-Block formula [77]. In the non-relativistic limit (v≪c), the energy loss per unit path length of a fragment with charge Z, mass A and velocity v within an absorber, can be well described by the following approximation of the Bethe-Block formula:

$$S = -\left|\frac{dE}{dx}\right| = \propto \frac{Z^2}{v^2} \propto \frac{Z^2 A}{E} \tag{2.1}$$

where E is the initial kinetic energy of the impinging particle and the proportionality constant only depends on the absorber.

Considering a telescope with two different stages, if the impinging particle passes through the first layer to be stopped in the second one, starting from Eq. 2.1 and considering a finite thickness of the first layer, the energy deposited in the ΔE layer can be considered as a reasonable approximation of the dE/dx value. Considering the energy deposited in the second layer as a good approximation of the total energy E, the corresponding energy loss ΔE in the first layer is therefore inversely proportional to it. It should be noted that the proportionality factor between these two energy measurements scales with the square of the particle charge Z and depends on its mass A. Therefore, drawing the correlation plot between the energy deposited in the first detector (ΔE) and the residual energy released in the second one (E_{res}), the different ion species will be distributed on different quasi-hyperbolic ridges depending on their charge Z and more weakly on their mass A.

The ΔE-E identification capability depends on the characteristics of the detectors, mainly their energy resolution and, for the ΔE stage, its thickness homogeneity. Several detector combinations can be used for this purpose, such as ionization chambers (IC), silicon detectors or scintillators. In general, the use of an IC as a first layer allows to have lower energy thresholds in the application of the ΔE-E technique, but spoils the mass identification capability due to the worse energy resolution of a gas detector compared to a standard silicon detector. In any case, the ΔE-E method can be applied only if the impinging particle is fully stopped within the telescope.

As an example, Fig. 2.7 shows a Si1-Si2 ΔE-E correlation matrix obtained with the FAZIA apparatus for the ^{58}Ni+^{58}Ni reaction at 32 AMeV, where punch-through events are removed with a veto condition on the CsI(Tl) detector.

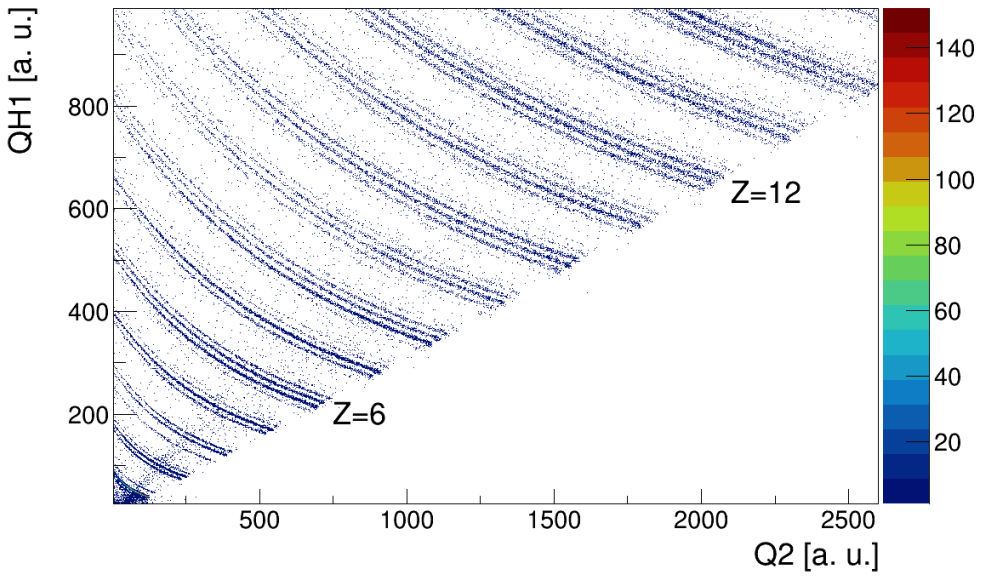

Figure 2.7: Example of Si1-Si2 ΔE-E correlation matrix for a FAZIA telescope for the ^{58}Ni+^{58}Ni reaction at 32 AMeV. Punch-through events are removed with a veto condition on the CsI(Tl) detector.

The residual energy detector can also be the CsI(Tl) scintillator. In this case, the Si-CsI ΔE-E method can be exploited both in FAZIA (see Fig. 3.2) and in rings 6-9 of INDRA (see Fig. 3.6). Although the method is the same, the use in FAZIA of thicker and more homogeneous silicon detectors, combined with in vacuum FEEs, results in a much higher performance: mass identification up to $Z \sim 26$ can be achieved with FAZIA, whereas in INDRA it remains limited to Z about 10 with the new electronics.

Fragments that do not have enough energy to reach the second layer cannot be identified with the ΔE-E technique. However, its energy threshold can be lowered by applying the Pulse Shape Analysis technique to particles stopped within the first layer.

2.4.2 Pulse Shape Analysis in silicon detectors

The Pulse Shape Analysis (PSA) is a powerful tool for the identification of fragments stopped in the first layer of a telescope (as Si1 in FAZIA), allowing

to reduce the energy threshold for identification with respect to the one of the ΔE-E technique. In fact, with PSA the information coming from the detector stopping the particle is enough for the identification.

Due to their different stopping powers, different particles with the same kinetic energy have different ranges, resulting in distinct energy loss profiles along the detector depth and, consequently, different signal shapes. For such a reason, by correlating a shape-related observable with the deposited energy, it becomes possible to distinguish and thus identify the detected fragments. For silicon detectors, two widely used shape parameters are the rise-time of the charge signal and the maximum of the current signal. The FAZIA collaboration investigated both approaches concluding that the latter provide better identification performance [78]. For this reason, the "current PSA" method is used in Si1 for the FAZIA apparatus. An example is shown in Fig. 2.8.

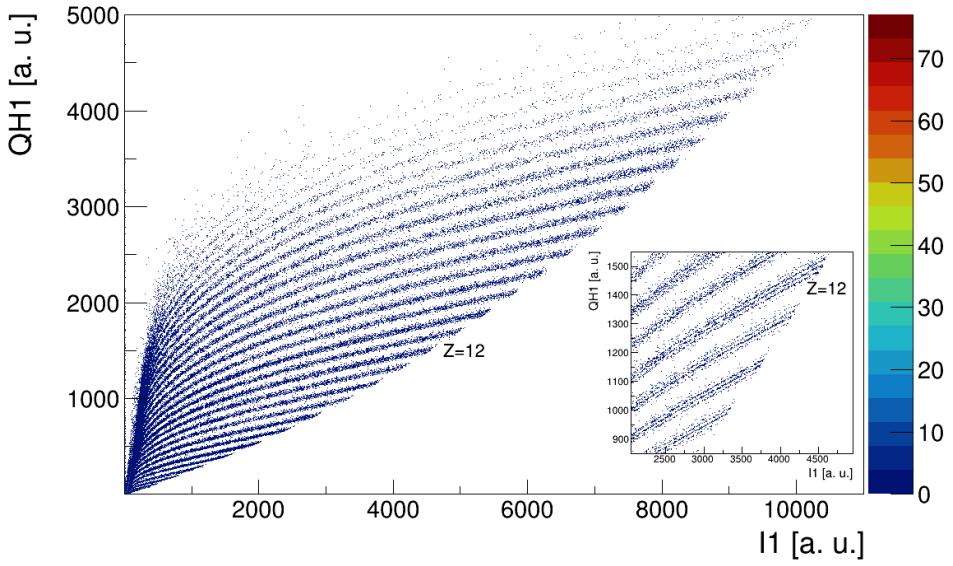

Figure 2.8: Example of PSA correlation between the energy in Si1 and the maximum of the corresponding current signal for the ^{58}Ni+^{58}Ni reaction at 32 AMeV. The inset shows an expanded view on the Z=12 region, to better appreciate the isotopic discrimination. Punch-through events are removed with a veto condition.

This method allows to obtain optimal performance for Z and A identification thanks to a careful construction of the Si detectors, as previously described, and thanks to the optimized PSA algorithms based, for the eval-

uation of the current maximum, on a smoothing spline interpolation, which leads to the best identification results as shown in [70].

2.4.3 Pulse Shape Analysis in CsI(Tl)

The PSA technique can be applied also to CsI detectors. In this case, the PSA method is possible thanks to the fact that the scintillation light produced in CsI(Tl) by the passage of a particle depends on its (Z,A) and energy. In particular, its time development can be described as the sum of two exponential functions with different decay constants:

$$I(t) = I_{fast} \cdot \frac{e^{-t/\tau_{fast}}}{\tau_{fast}} + I_{slow} \cdot \frac{e^{-t/\tau_{slow}}}{\tau_{slow}} \tag{2.2}$$

where the two time constants are $\tau_{fast} \sim 700$ ns and $\tau_{slow} \sim 5$ μs. The decay constant, and in particular the intensity of the two components, depend on the Z, A and energy of the particles, allowing the PSA application. The I_{fast}/I_{slow} ratio tends to become constant for heavier fragments [79], but in both FAZIA and INDRA this method is applied exclusively to identify light particles. In particular, it is used for high-energy light particles, for which the ΔE deposited in the silicon detectors is so small that the signal amplitude becomes comparable with the electronic noise, making it impossible to apply the ΔE-E method. Moreover, this method is essential for INDRA rings 10-17, where the CsI(Tl) crystals are the only working detectors and CsI PSA is therefore the sole available identification technique. Fortunately, at these backward angles, the detected particles are exclusively light particles, for which the PSA performance is sufficient to ensure accurate identification.

The PSA relies on disentangling the two components by processing the CsI signal with two different shapers, each set to a time constant close to the τ_{fast} and τ_{slow}. The amplitude of the fast shaper mostly depend on I_{fast}, while the slow one is sensitive to the total emitted light. For this reason, in many previous work of the FAZIA collaboration, the fast component has been plotted as a function of the slow component after subtracting a fraction of the fast one (typically 0.8), in order to better separate the two contributions and improve the isotopic identification. Recently, a new correlation plot, i.e. the ratio of the fast to the slow component vs the slow one, has been proposed [80]. An example of such a correlation matrix for an INDRA CsI is shown Fig. 2.9. For comparison, a PSA matrix from a FAZIA crystal is shown in Fig. 3.8.

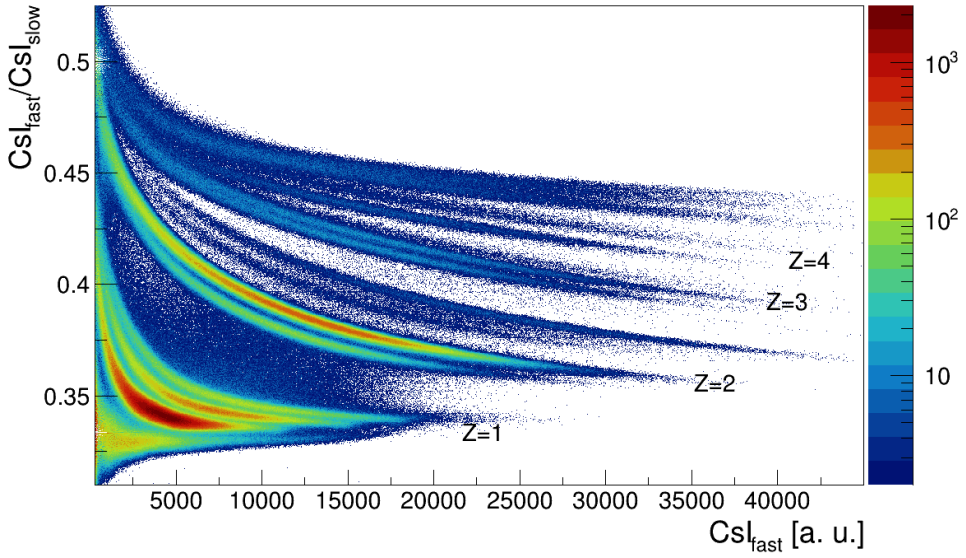

Figure 2.9: Example of a CsI PSA matrix (fast/slow vs slow) obtained with an INDRA crystal for the ^{58}Ni+^{58}Ni reaction at 74 AMeV. Events below the Z=1 lines correspond to γ-rays detected by the CsI.

Chapter 3

The E789 and E818 experiments: ^{58}Ni+^{58}Ni at 32, 52, 74 AMeV

In this work we will investigate the ^{58}Ni+^{58}Ni reaction at three different energies 32, 52 and 74 AMeV in order to study how the reaction dynamics evolve with centrality and beam energy. These systems were measured during the first two campaigns (E789 and E818 in the following) carried out with the INDRA-FAZIA apparatus.

The E789 experiment, conducted at GANIL in 2019, was the first experimental campaign to exploit the coupled INDRA-FAZIA apparatus. This campaign focused on the neutron-proton equilibration in Ni+Ni systems at 32 and 52 AMeV. The measurement of all the four possible combinations of the two reaction partners, ^{58}Ni and ^{64}Ni, provided the opportunity to compare the properties of the reaction products of the two asymmetric reactions, with those of both the neutron rich and the neutron deficient symmetric systems. Moreover, the two different energies modify the timescale of the interaction process. The isospin equilibration has been investigated employing the isospin transport ratio technique [81] in both the evaporative (QPr) and breakup (QPb) channels. The results of this campaign, already published in [59, 60, 82], have evidenced a relaxation of the initial isospin imbalance with increasing centrality, with a stronger isospin equilibration for the reactions at 32 AMeV, as expected due to the longer projectile-target interaction time than at 52 AMeV [59]. Furthermore, a higher degree of equilibration has been observed in the breakup channel compared to the QPr channel. This behavior may be interpreted in terms of different average projectile-target contact times, as supported by the contact time estimates extracted from antisymmetrized molecular dynamics simulations [60].

The second experiment with the INDRA-FAZIA apparatus, the E818 experiment, was conducted at GANIL in 2022. The measured reactions were ^{36}Ar,^{58}Ni+^{58}Ni at 74 AMeV. This second campaign focused on the clusterization properties of nuclear matter in central collisions adopting the nuclear statistical equilibrium scheme modified by in-medium effects [83]. In fact, previous studies performed with the INDRA apparatus have examined the mid-rapidity source emissions and determined the chemical equilibrium constant including in-medium corrections [84, 85]. The goal of the E818 experiment was to extend the in-medium measurements to heavier clusters by selecting the vaporisation source, thus extending the range of produced clusters, and by using the FAZIA+INDRA apparatus, which offers improved isotopic resolution.

Considering both the E789 and E818 experiments, the ^{58}Ni+^{58}Ni reaction was measured at 32, 52 and 74 AMeV, allowing for a detailed investigation of how the reaction dynamics evolve with the beam energy.

In Tab. 3.1 a summary of the characteristics of the reactions studied in this analysis are presented.

$Energy$ $(AMeV)$	b_{gr} (fm)	$\theta_{\mathrm{gr}}^{\mathrm{lab}}$ (deg)	$v_{\mathrm{CM}}^{\mathrm{lab}}$ (mm/ns)	$v_{\mathrm{p}}^{\mathrm{lab}}$ (mm/ns)	$v_{\mathrm{p}}^{\mathrm{CM}}$ (mm/ns)
32	10.61	6.56	38.98	76.67	38.98
52	10.86	3.95	49.43	96.26	49.43
74	10.97	2.75	58.64	112.96	58.64

Table 3.1: Kinematic characteristics of the ^{58}Ni + ^{58}Ni reactions

The INDRA-FAZIA apparatus, already described in the previous chapter, has been mounted in a scattering chamber placed in the D5 experimental hall in GANIL. For both experiments, the INDRA ionization chambers were not mounted. As mentioned, FAZIA was located at the forward polar angles, replacing rings 1 to 5 of INDRA multidetector. In the first campaign FAZIA was positioned at the standard distance of 100 cm from the target, covering the polar angles between 1.4° and 12.6°. For the second campaign instead FAZIA was placed at 85 cm from the target with a polar coverage from 1.9° to 14°. The targets were mounted on a target holder inserted between rings 12 and 13 of INDRA. In the E789 experiment a ^{58}Ni target with a thickness of 300 μg/cm^2 was used, while in the E818 campaign one 410 μg/cm^2 thick.

In the E789 experiment, the trigger condition for FAZIA was M$\geq$2, while triggers M$\geq$1 could also be acquired but downscaled by a factor 100. Whereas for INDRA the minimum bias M$\geq$1 trigger was used with the additional condition to be in coincidence with a FAZIA trigger. A different trigger was

adopted in the E818 experiment, consisting in the minimum bias trigger M≥1 for both FAZIA and INDRA. For INDRA only rings 6 to 9 were triggering the acquisition (silicon detectors).

To have an idea of the detector granularity, the dead zones between the two apparatuses, and the not working detectors, polar plots for the reaction ^{58}Ni+^{58}Ni at 74 AMeV are shown in Fig. 3.1. The plots have been obtained

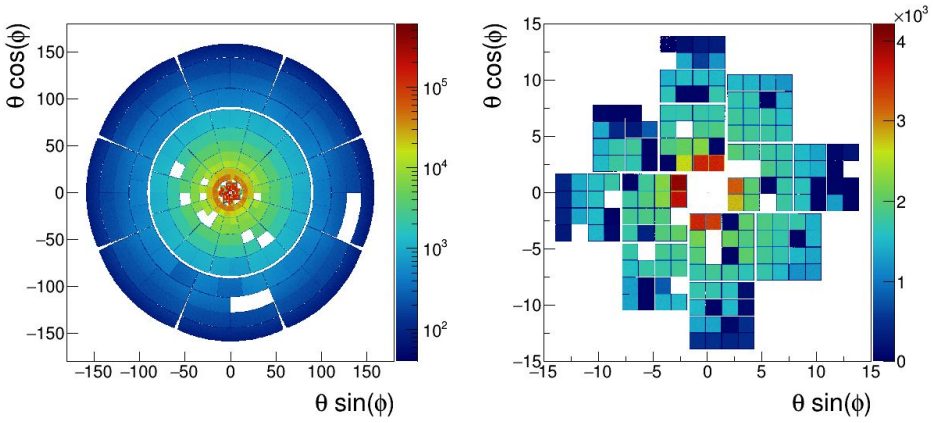

Figure 3.1: Polar plots $\theta\cos(\phi) - \theta\sin(\phi)$ representing the geometrical coverage of the experimental apparatus in the laboratory reference frame for the reaction ^{58}Ni+^{58}Ni at 74 AMeV. Left panel: the INDRA-FAZIA apparatus. Right panel: the FAZIA detector.

by reporting the correlation $(\theta\cos(\phi), \theta\sin(\phi))$ of all the experimentally detected particles. The left panel displays the complete INDRA-FAZIA apparatus, whereas the right panel shows a close-up of the 12 FAZIA blocks.

Before being able to exploit the data from an experiment, data reduction, which mainly involves the calibration of detectors and the identification of detected particles, must be carried out. In the following, the procedures for the E818 experiment will be described. See Ref. [86] for more details about the E789 experiment.

3.1 Identification procedure

Data reduction starts with the identification of the detected particles in charge and, when possible, in mass. Although the identification techniques, already described in Section 2.4, are based on different physical processes and different correlations, a similar identification procedure is applied to all of them. In the following, the identification procedure, performed using the

Kaliveda software (a homemade C++ based code developed within the collaboration) [87], is described in detail for the Si1+Si2-CsI ΔE-E correlation. Then, an example for each identification method is presented, highlighting the differences between them.

The first step of the procedure requires the manual drawing of the "identification grid", consisting of several lines placed along the correlation ridges, as plotted in black in Fig. 3.2. A graphical tool is used to click points on

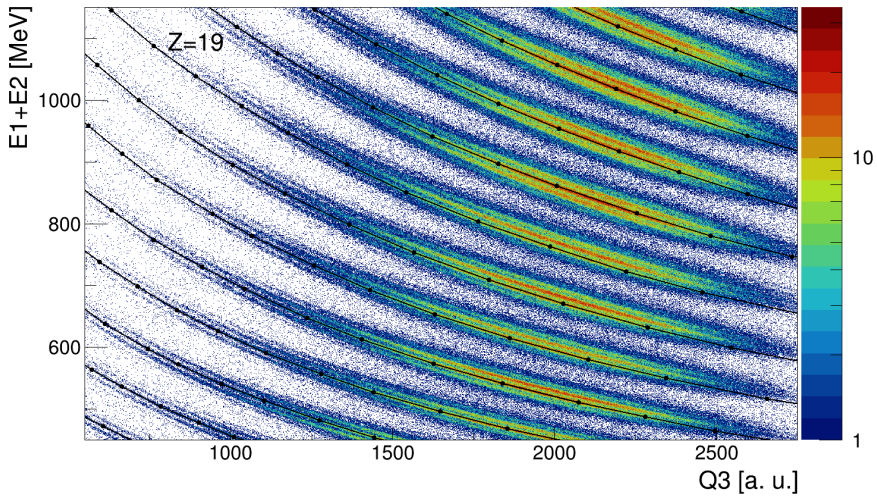

Figure 3.2: Si1+Si2-CsI ΔE-E correlation matrix obtained with a FAZIA telescope for the ^{58}Ni+^{58}Ni reaction at 74 AMeV. The identification grid is plotted in black; a single line has been drawn for each element.

each ridge, in order to obtain a segmented line that follows it as accurately as possible. In this case, only one line is drawn for each element, even when isotopic ridges can be recognised. A Particle IDentification (PID) value equal to the atomic number Z of the underlying experimental curve is assigned to each line. At this point, a linearisation procedure is applied: basing on the position of the event on the correlation matrix, a PID value is assigned to each particle by interpolating between the PID values of the four closest lines. At the end of the interpolation a PID distribution is obtained, as shown in Fig. 3.3, where each peak corresponds to a different isotope. Starting from a single element, the mass identification is performed through a multi-Gaussian fit on its PID distribution. If two Gaussian distributions overlap, the masses are probabilistically assigned according to the values of each Gaussian peak. An example of the fitting results are show in Fig. 3.4, where starting from Fig. 3.3, the distributions of carbon, sulphur and iron isotopes are shown. The filled grey area represent the PID distribution. The multi-Gaussian

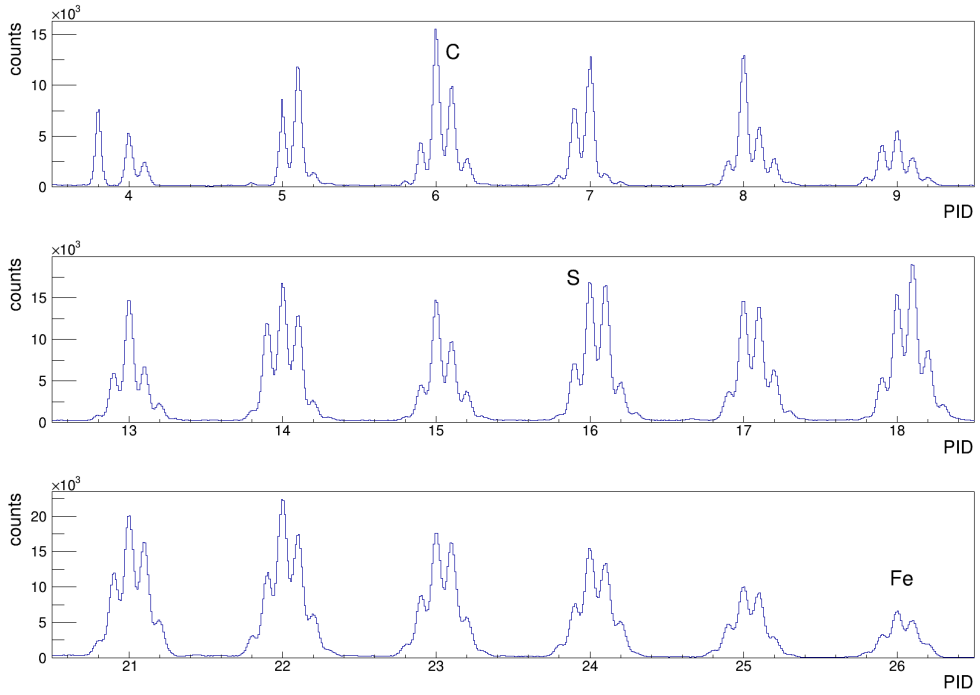

Figure 3.3: PID distribution of some elements obtained from the Si1+Si2-CsI ΔE-E correlation matrix of a FAZIA telescope for the ^{58}Ni+^{58}Ni reaction at 74 AMeV.

fits are drawn with black lines, while the single Gaussian fit with coloured dotted lines. At the end of the identification procedure, the particles not well-identified because in between two lines are discarded. The result of the complete identification procedure can be viewed in Fig. 3.5, that presents the nuclide chart (N,Z) including all the identified particles. In this example, obtained with the data of the reaction at 74 AMeV, isotopes are identified up to Z=26. This represents a significant improvement with respect to the E789 campaign, where the ΔE-E correlation with the CsI allowed isotopic discrimination only up to $Z = 18$. The improved performance is related to the better ΔE signal, achieved in two ways:

- the increasing of the thickness of the Si2 in some of FAZIA block (750 μm instead of 500 μm for the four inner blocks)
- the use of the Si1+Si2-CsI correlation instead of Si2-CsI.

In this way, in the E818 experiment, 800 or 1050 μm of silicon detectors were used as ΔE instead of the 500 μm employed in the E789 identification

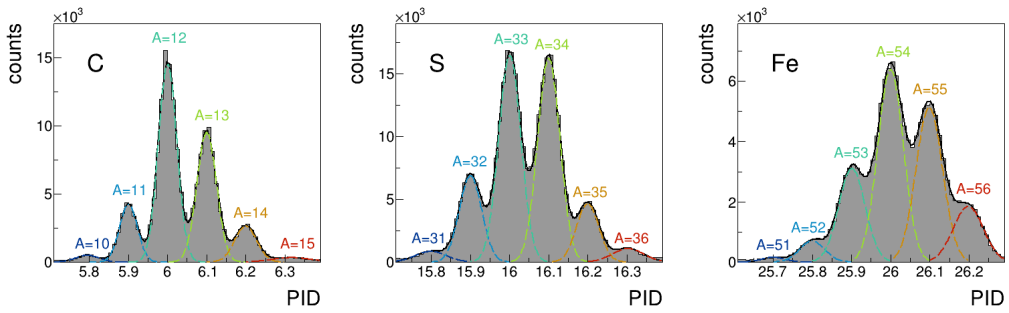

Figure 3.4: PID spectra for carbon, sulphur and iron isotopes obtained with a Si1+Si2 vs CsI correlation. Different colours show the single Gaussian fit for each isotope, while black line corresponds to the global fit.

procedure, increasing the deposited energy and consequently decreasing the impact of the energy straggling phenomenon.

An identical procedure is applied to the ΔE-E identification in Si1-Si2 for FAZIA (see Fig. 2.7), which allows isotopic identification up to $Z \sim 25$, and in Si-CsI for rings 6-9 of INDRA, as shown in the left panel of Fig. 3.6. As anticipated, the implementation of the new digital electronics in INDRA, combined with the use of new silicon detectors for rings 6 and 7, has made it possible to achieve isotopic discrimination unprecedented within INDRA. This is evident in the right panel of Fig. 3.6 where the multi-Gaussian fit is shown for Z=10 in the case of the ^{84}Kr+^{124}Sn reaction, which produces elements heavier than those populated in the Ni+Ni system.

From the point of view of the procedure, the same identification method is also applied to the FAZIA Si1 PSA correlation, using again only a single line drawn for each element. The main difference is that, in this case, charge and mass discrimination are not achieved over the entire correlation, as shown in Fig. 3.7a. Therefore, also two graphical cuts are needed. The red contour delimits the region where the resolution is not good enough to allow element identification. The fragments falling in this area are excluded from the analysis. The green contour instead delimits the area where there is also isotopic resolution. Only for the events inside this region a mass is assigned with the method described above. For the fragments outside of this area, a mass according to the EAL is assigned. The corresponding nuclear chart of the particles identified both in Z and A, is presented in Fig. 3.7b. It should be noted that with this method particles with Z=1 and 2 are not identified in A.

The identification procedure adopted for the CsI PSA differs slightly with respect to the standard procedure described above. As previously mentioned,

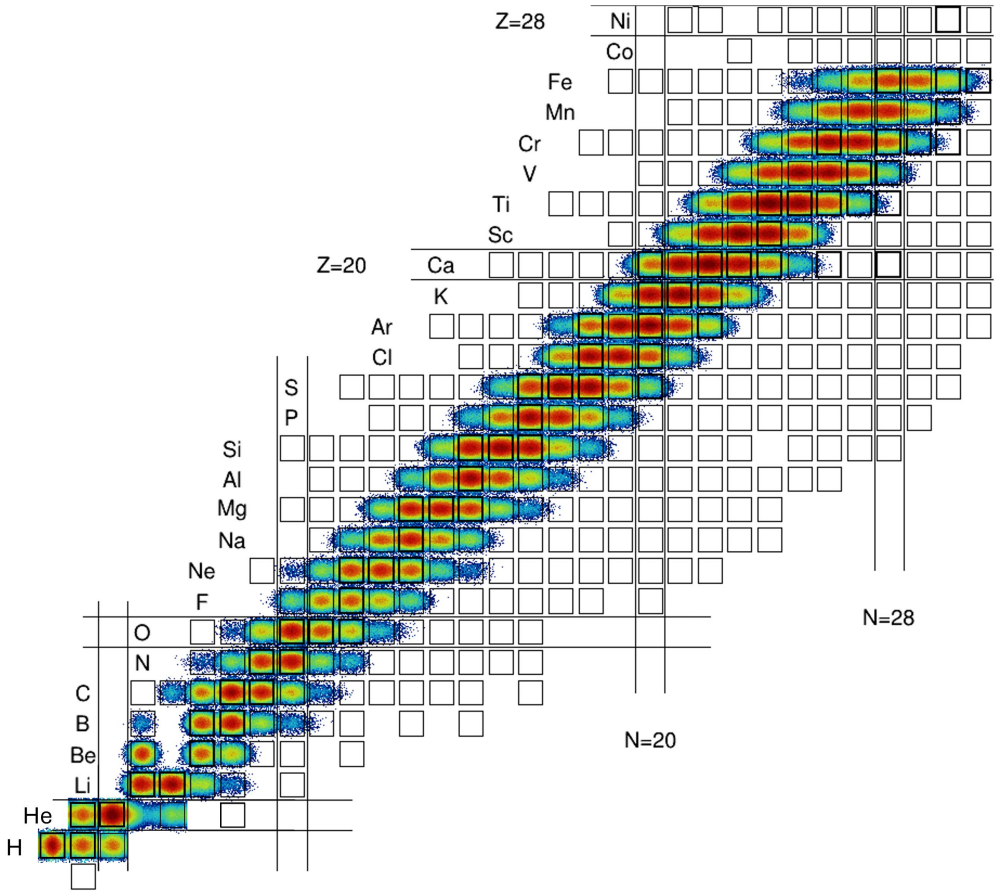

Figure 3.5: Nuclide chart obtained from the identification results of the Si1+Si2-CsI ΔE-E method for a FAZIA telescope for the ^{58}Ni+^{58}Ni reaction at 74 AMeV.

this identification method mainly concern light and energetic particles. An example of a FAZIA correlation matrix is presented in Fig. 3.8, where the ratio of Fast Light to Total Light (Q3fast/Q3) is plotted as a function of the Total Light (Q3). Since the identifiable ions range from Z=1 to Z=4, a different line for each isotope has been drawn (in black in Fig. 3.8), and a PID value has been assigned with the information on both Z and A of the detected particle. Since at low CsI energies it becomes difficult to distinguish the isotopic lines, a contour cut, drawn in red, is defined to exclude these particles from CsI PSA identification, favouring instead Si-CsI identification, which performs much better in this energy range. Moreover, a cut line (in green) has been used to exclude the region below Z=1 lines, which is associated with uncharged particles such as gamma-rays and possible Incomplete

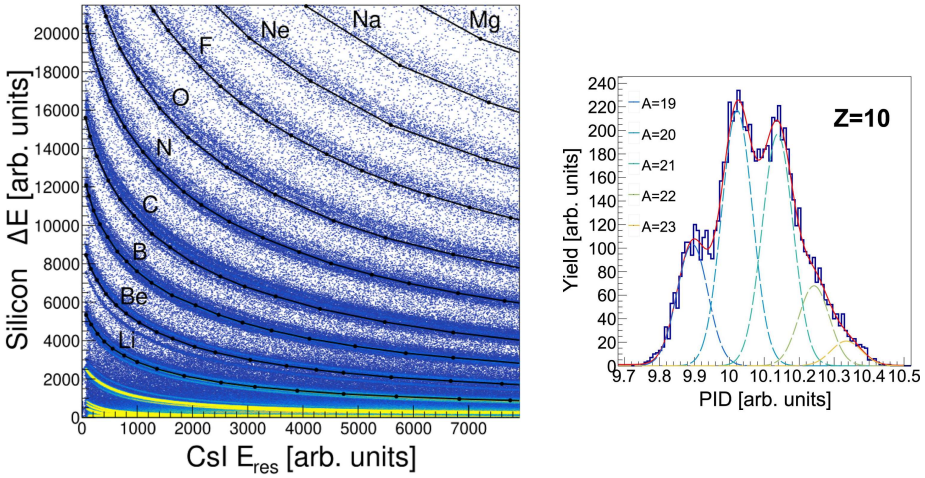

Figure 3.6: Left panel: Si-CsI ΔE-E matrix of a INDRA telescope for the ^{84}Kr+^{124}Sn at 68 AMeV. Right panel: corresponding multi-Gaussian fit for Z=10. Figures taken from [74].

Energy Deposition (IED) events, as described in Appendix B. Once that the identification grid and the contours are defined, the particle identification procedure is then the same as previously described.

For rings 6-9 of INDRA, where a Si detector is the first layer, the identification procedure for the CsI PSA is the same. Instead, for rings 10-17, where the telescopes consist only of a CsI(Tl) detector, obviously, particle identification relies exclusively on the CsI PSA technique. It is important to mention that in some cases in the CsI PSA of INDRA, the separation between protons, deuterons and tritons is lost for higher energies. In this case we add another graphical cut, in order to delimit this region. The fragment inside this cut will be removed in the analysis when the energy and/or mass of the particles are involved, but will be taken into account from the point of view of the total Z=1 multiplicity.

The identification capability of the FAZIA (upper panels) and INDRA (lower panels) apparatuses are summarized in Fig. 3.9, where the identification energy threshold for the different identification methods are shown for the "typical" detectors of the E789 (left panels) and E818 (right panels) experiments. Of course, these limits depend on the actual performance of individual telescopes, but they can be considered representative of the typical behaviour. In each panel, the different region of identification methods are shown with different colours as a function of the charge of the fragments and their energy per nucleon. The darker areas correspond to regions where isotopic identification is also achieved. For FAZIA, the identification thresholds

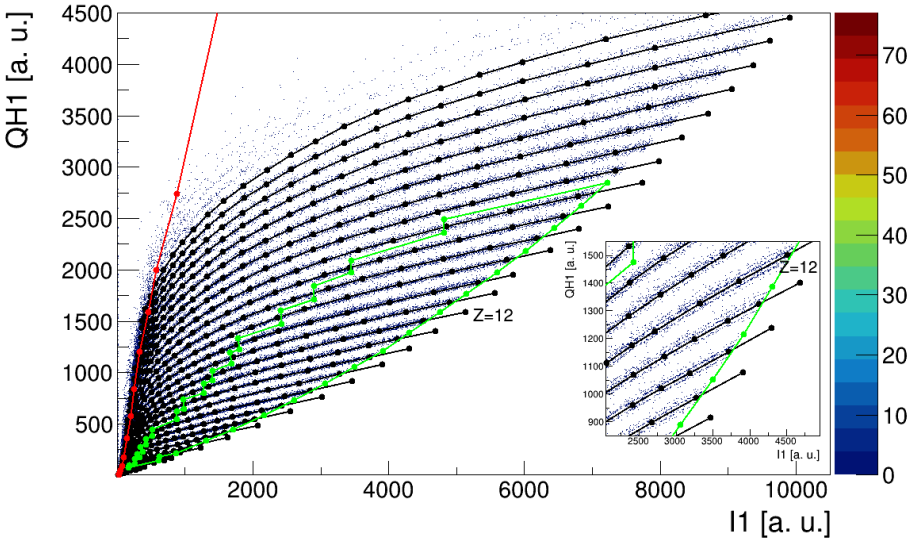

(a) Si1 PSA matrix and grid

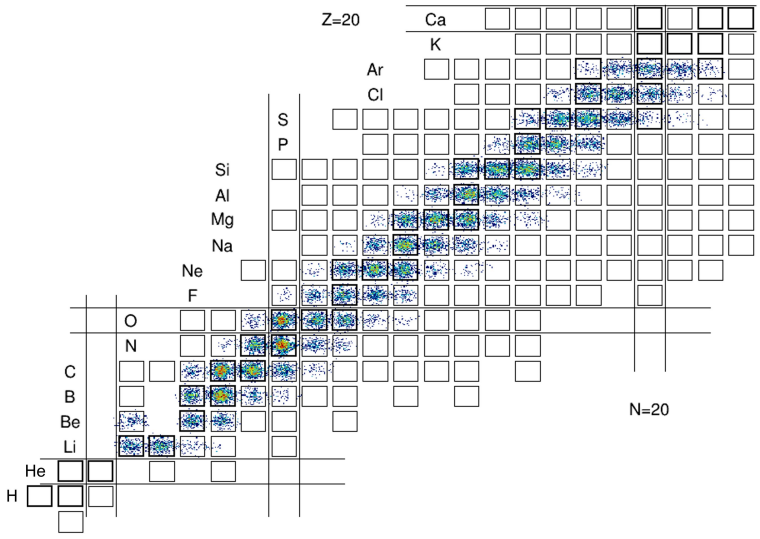

(b) Nuclide chart

Figure 3.7: Si1 PSA identification with a FAZIA telescope for the ^{58}Ni+^{58}Ni reaction at 32 AMeV. Panel (a) shows a Si1 current PSA matrix with its corresponding identification grid plotted in black and the graphical contours to delineate the zone of Z and A identification (green) and the region without identification (red). Panel (b) presents the nuclide chart of the particles identified within the green contour.

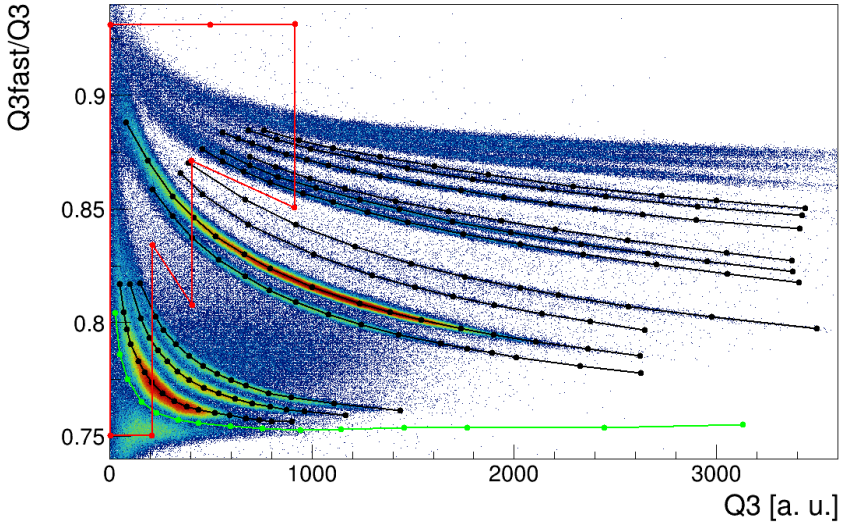

Figure 3.8: CsI PSA correlation matrix (Q3fast/Q3 vs Q3) for a FAZIA telescope. The identification grid is plotted in black. Events below the green cut line are excluded. The red contour delimits the area where the ΔE-E method is applied.

shown for the E789 experiment correspond to the standard silicon thicknesses of 300 and 500 μm, while for E818 the configuration with a 750 μm Si2 detector is shown. The use of a thicker Si2 extends the energy domain where the Si1-Si2 correlation can be applied. A second noticeable difference between the two experiments concerns the ΔE-E correlations with the CsI(Tl) stage: by using the Si1+Si2-CsI correlation, instead of the standard Si2-CsI one, the isotopic identification improves significantly, from $Z \sim 18$ up to $Z \sim 25$. Regarding INDRA, no PSA on silicon detector is applied, so the thresholds of the Si-CsI method naturally depend on the silicon thickness, as illustrated for 150μm (solid line) and 300μm (dashed line). The improvement in isotopic separation between E789 and E818 is evident, extending from $Z \sim 6$ in the left panel to $Z \sim 10$ in the right one. Finally, it should be noted that the identification region corresponding to the PSA in CsI(Tl) is not included in Fig. 3.9. Qualitatively, the CsI PSA extends the identification of the light fragments above ∼100 MeV, where the energy deposited in the silicon layers becomes too low for use of the ΔE-E method, and, in rings 10-17 of INDRA, it enables the identification of all detected light particles.

Considering the 192 FAZIA telescopes and the four different identification techniques applied, almost 800 identification grids were produced. Addition-

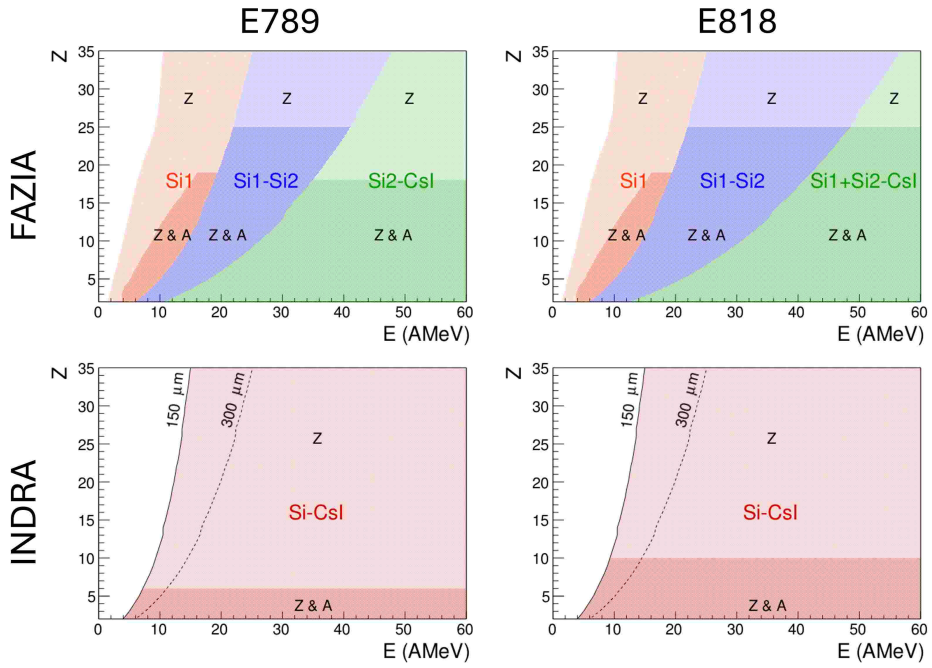

Figure 3.9: FAZIA (upper row) and INDRA (lower row) identification energy thresholds obtained by combining all the identification methods for the E789 (left panels) and E818 (right panels) experiments. The identification via CsI PSA is not included in this plot.

ally, for the fragments stopped in the first four rings of INDRA (rings 6-9), corresponding to 96 telescopes, the Si-CsI ΔE-E and CsI PSA methods were used, resulting in about 200 additional grids. A further 144 INDRA CsI detectors from rings 10 to 17 ring required grids based on the PSA technique. Overall, more than one thousand identification grids had to be manually drawn, keeping also in mind that minor shifts in correlation, caused by slight variations in detector response during data acquisition, must be taken into account.

3.2 Energy calibration

The amount of energy deposited by a particle in a detector is a fundamental piece of information that can only be obtained through an energy calibration process, which requires a set of reference points with known energies. Correlating these known energies with their corresponding signal amplitudes and knowing the functional form for the detector response, one can determine the calibration parameters for each detector. In the E818 experiment, the energy

calibration was performed using both α source runs and ^{12}C beam runs. The α source consisted in a mixture of ^{239}Pu, ^{241}Am, and ^{244}Cm. These radionuclides decays via α emission, producing an energy spectrum characterized by a three main structures (one for each nuclide) with finer substructures depending on the different probabilities associated to each transition that cannot be resolved with the INDRA-FAZIA setup. Therefore, an average energy is adopted for each radionuclide, as shown in Table 3.2. The source

Radionuclide	Average Energy (Mev)
^{239}Pu	5.147
^{241}Am	5.479
^{244}Cm	5.796

Table 3.2: Average energies associated with each radionuclide.

was placed on a target holder inside the chamber, replacing a standard target. Considering the limited range of such α particles (below 30 μm) and its 4π solid angle emission, the α source allowed for the calibration of the Si1 detectors of FAZIA as well as the silicon detectors of INDRA. In addition, also two ^{12}C beams at 8.75 AMeV and 13.75 AMeV scattered on a ^{197}Au target with a thickness of 980 μm were used. In the case of the ^{12}C beam at 8.75 AMeV, also ^{15}N and ^{18}O contaminant nuclei were observed. These nuclei have the same A/Q ratio and therefore are not well separated from the beam during acceleration. When sufficient statistics are available, these nuclei can be taken into account during calibration as additional reference points. All scattered products from the 8.75 AMeV beam stop in the FAZIA Si1 detectors and the 300 μm silicon detectors of INDRA. The products from the 13.75 AMeV beam pass through both the Si1 and Si2 detectors of FAZIA, as well as all the silicon detectors of INDRA.

Si calibration

The FAZIA Si1 and INDRA Si detectors were calibrated using the combination of α source and elastic scattered nuclei of the ^{12}C beam at 8.75 AMeV, with also the contaminants, as everything stops in the first layer. This is crucial to perform an energy calibration which is independent from the silicon thickness, which is known only within few % of precision.

Since the response of silicon detectors is linear, a linear fit can be used to determine a calibration parameter for each detector, as shown in the upper panel of Fig. 3.10. As shown in the lower panel, the residues between experimental points and the proposed calibration are typically at most 0.2-0.3 MeV.

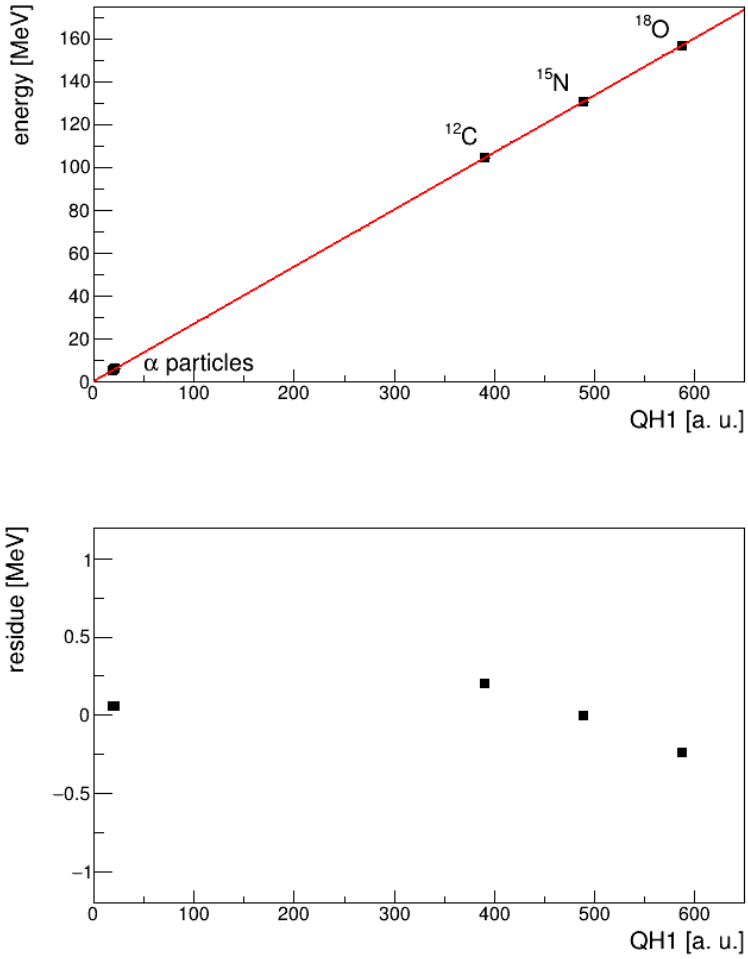

Figure 3.10: Energy vs ADC units calibration plot for a FAZIA Si1 detector. The linear fit result is drawn with the red line and the fit residues are plotted in the bottom panel.

Once the energy calibration of Si1 is completed, an independent measurement of its thickness is essential, as it is a key parameter for calibrating the Si2 and CsI detectors. This was performed using the 13.75 AMeV ^{12}C calibration beam, which punches through the Si1, making the energy deposition sensitive to its thickness. By simulating the energy deposited by this beam as a function of silicon thickness, as shown in the left panel of Fig. 3.11, and comparing it with the experimental deposited energy, the thickness of each silicon detector was determined. The resulting distribution of Si1 thicknesses

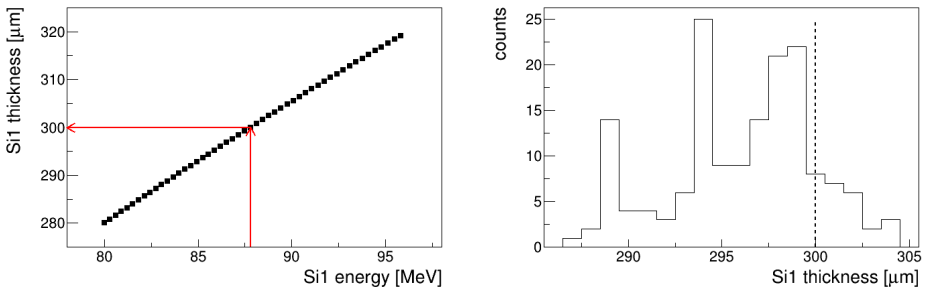

Figure 3.11: Left panel: Si1 thickness as a function of the energy released by the 13.75 AMeV ^{12}C beam . Right panel: obtained distribution of the Si1 thicknesses with the dashed black line corresponding to the nominal value of 300μm.

is shown Fig. 3.11. Deviations of up $\sim$5% from the nominal thickness (dashed line) were found.

After determining the Si1 thickness, the energy calibration of the FAZIA Si2 detectors was obtained using the ^{12}C beam at 13.75 AMeV.

As already discussed for Si1, the knowledge of the Si2 thickness is also important for the energy calibration of the following layer. However, the situation is different: while an elastically scattered ^{12}C beam punching through the layer was available for Si1, no analogous beam could be used for Si2. Although many isotopes produced in the Ni+Ni reactions punch through the Si2 layer, their punch-through points cannot sufficiently constrain the Si2 thickness, as already demonstrated in [83]. For this reason, the nominal thickness values are adopted for the FAZIA Si2 detectors, as it is also done for the INDRA Si detectors.

CsI calibration

When the CsI is part of a ΔE-E telescope, once the silicon stages have been calibrated, the energy released in CsI can be calculated from the ΔE in the

previous silicon layers using energy-loss tables. This makes, in principle, the energy calibration of the CsI, which is particularly complicated, not necessary. This procedure is employed for FAZIA, which includes both Si1 and Si2 layers, as well as for INDRA rings 6-9, where a single silicon layer precedes the CsI(Tl) crystal. Therefore, for many ions, the energy calibration of the CsI is not required. However, for high-energy light particles, the signal amplitude released in the silicon stages can be comparable with the electronic noise. Therefore, for particles with Z=1,2 an energy calibration of the CsI detector is necessary in order to obtain a reliable reconstruction of the deposited energy. There is no dedicated beam for calibrating the CsI detectors, so data from physical runs must be used. In particular, fragments that punch through the silicon stages of the telescopes and stop in the CsI detectors were employed for this purpose. For each isotope, the energy deposited in the CsI calculated from the energy released in the previous silicon layers (E_{res}) and the Light Output (LO) in arbitrary units have been correlated. The CsI detectors do not have a linear response and depends on the (Z,A) of the detected ion [88]. Therefore, a formula is needed to predict the LO as a function of E_{res} for each fragment (Z,A). The FAZIA collaboration uses the formula proposed in [88]:

$$LO = a_1\left\{E_{res}\left[1 - a_2\frac{AZ^2}{E_{res}}ln\left(1+\frac{E_{res}}{a_2AZ^2}\right)\right] + a_4a_2AZ^2ln\left(\frac{E_{res}+a_2AZ^2}{Aa_3+a_2AZ^2}\right)\right\} \tag{3.1}$$

where the parameter a_1 depends on the electronic gain, while a_2, a_3, a_4 are characteristic of the CsI crystal. In particular, a_2 is the parameter used to take into account the quenching effect in the crystal, a_3 is the energy per nucleon threshold for δ-ray production, and a_4 is the fractional energy loss due to the δ-rays. This is a general formula developed by the INDRA collaboration to account for ions ranging from protons to uranium. In the present case, only the calibration points corresponding to isotopes with Z=1,2 were considered in the fitting procedure, which simultaneously fits the points for H isotopes and those for He isotopes. Fig. 3.12 shows the results of the calibration fit in the upper panels and the corresponding residues in the bottom panels. It should be noted that, although the formula employed is quite complex, the fit for protons remains nearly linear, confirming that the quenching effect is negligible for protons [80].

For the CsI(Tl) crystals of the INDRA rings from 10 up to 17, no active layer in present in front of them. In fact, as previously discussed, a silicon layer is absent and the IC were not working during these experiments. Therefore, calibration requires dedicated beams in order to apply Eq. 3.1. Considering that all CsI(Tl) crystals and photomultipliers were dismounted

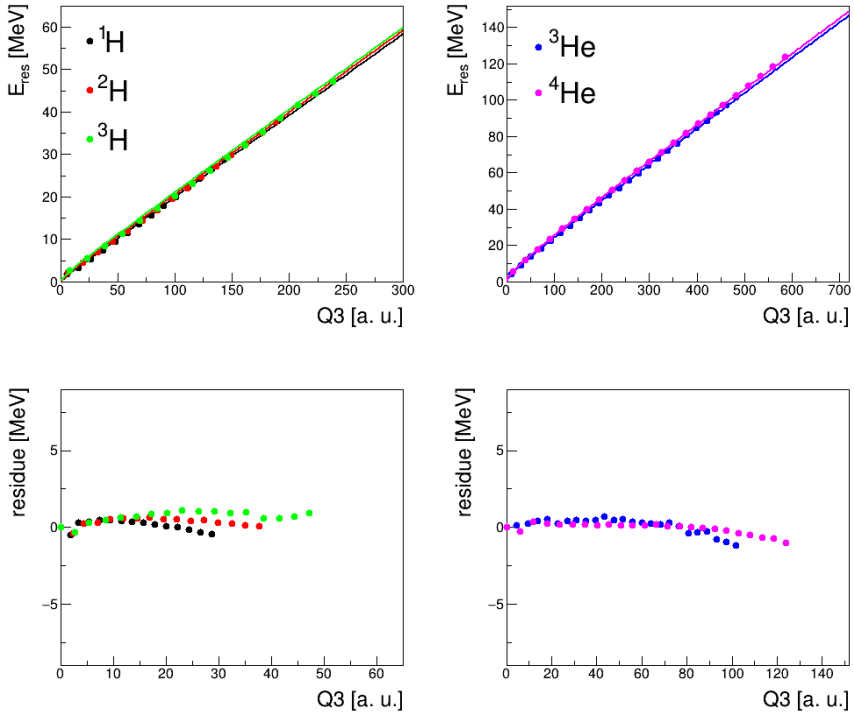

Figure 3.12: Upper panels: CsI energy vs Light Output plots for a FAZIA CsI with the results of the fit procedure for the calibration of Z=1 (left) and Z=2 (right) isotopes. The corresponding residues are plotted in the bottom panels.

and reassembled just before the E789 experiment, the old datasets of elastically scattered calibration beams could not be directly used. Consequently, the only way to perform an energy calibration was to compare the results of these new experiments with old ones, in which the same ^{58}Ni+^{58}Ni reaction at the same energies had been measured. At that time, the CsI crystals were calibrated with a cocktail beam selecting different energies. Since the detectors are the same, the parameters a2, a3, a4, which depend mainly on the properties of the crystals, remain unchanged. Only the gain parameter a_1 has changed, due to the replacement of the electronics and refurbishment of the crystals. Therefore, by comparing the energy spectra of protons and α particles from the old and new datasets, a correction factor accounting for the gain variation can be determined. This factor allows the measured energies in the new data to be converted to match those from the old dataset. Once this correction is applied, the original calibration parameters from the old data can also be used to calibrate the new dataset.

Chapter 4

Theoretical models and simulations

In order to investigate the mechanisms governing nuclear reactions in the Fermi energy regime, a comparison between experimental data and theoretical models is essential. A widely adopted framework involves a two-step simulation procedure. The first step, known as the dynamical phase, describes the interaction between projectile and target nuclei and the production of excited primary fragments. In the second step, the statistical phase, the hot primary fragments undergo statistical de-excitation, producing the so-called secondary fragments. In this stage, the primary nuclei are treated as excited systems in thermal equilibrium that evolve towards their ground state, dissipating energy through the open de-excitation channels according to the branching ratios.

The dynamical phase is usually simulated with transport models, which can be grouped into two main classes: models based on a mean-field approach, such as the Boltzmann-Uehling-Uhlenbeck (BUU) equation [89, 90], and those based on the molecular dynamics, which explicitly follow the evolution of nucleon coordinates and momenta, as the Antisymmetrized Molecular Dynamics model (AMD) [91–95] used in the following. The AMD model has already been successfully used for the description of reactions at Fermi energies [34, 96, 97] also by our collaboration [33, 40, 58]. The AMD simulation is typically stopped at 500 fm/c, a timescale sufficient to consider the dynamical evolution as completed. The resulting primary fragments are subsequently de-excited using a statistical decay model, used as afterburner. For this purpose, the GEMINI++ code [98] is adopted in the present analysis. The AMD code is heavily CPU time consuming. Therefore, the number of primary events produced by AMD was limited to about 20000 per system, which required approximately two months of computation time, and

then the de-excitation was simulated with GEMINI++, generating 100 secondary events - randomly distributed in the azimuthal direction - for each primary event in order to increase the statistics. The secondary fragments produced in the simulation at the end of the statistical phase correspond to those experimentally detected, since the characteristic time of the primary interaction and particle decay (well below $\sim 10^{-6}$ ns) is much shorter than the fragment flight time towards the detectors ($\sim$10 ns).

AMD offers a reliable framework for describing nuclear collisions at intermediate energies, providing also the possibility to recognise the fragments during the dynamical phase at different times (see Section 4.5). In this work, AMD is used as the reference for comparison with the experimental results throughout the analysis, also including a replica of the apparatus response to allow a direct comparison between simulation and experimental data (see Section 4.4). In the following, unfiltered simulations will be referred to as "4π" to distinguish them from the detector-filtered results. Furthermore, the AMD+GEMINI++ model is used to determine efficiency corrections for the experimental data, by comparing particle distributions from filtered and 4π simulations, as described in detail in Section 6.2.1. These corrections are essential for the source reconstruction analysis (discussed in Chapter 7), where the properties of the light particles are used to achieve information on the nuclear dynamics. To estimate possible systematic uncertainties associated with the efficiency correction, a second model has also been employed for the reaction at 74 AMeV: HIPSE [99] coupled to SIMON [100] as afterburner. HIPSE is a phenomenological model frequently adopted in literature [101–103] to obtain a general description of the fragments produced in the reaction, with the advantage of being significantly less CPU demanding than AMD, requiring only few days instead of months to produce the same statistics.

The next sections provide a detailed description of the AMD and GEMINI++ models, followed by a brief overview of HIPSE and SIMON. Finally, the characteristics of the dynamical phase within AMD of the ^{58}Ni+^{58}Ni reaction at 32, 52 and 74 AMeV is investigated.

4.1 Antisymmetrized Molecular Dynamics

AMD is a molecular dynamics based model whose characteristic feature is the full antisymmetrization of the multinucleon wave function, also including the treatment of the nucleon-nucleon collisions. Recently, also the formation of light clusters has been implemented [94]. A detailed presentation of the model can be found in [91]; here we provide only a brief overview.

AMD describes nucleons as Gaussian wave packets. The wave function of

the system of A nucleons is described by a Slater determinant

$$|\Phi(Z)\rangle = \det\left[\exp\left\{-\nu\left(\mathbf{r}_j - \frac{\mathbf{Z}_i}{\sqrt{\nu}}\right)^2 + \frac{1}{2}\mathbf{Z}_i^2\right\}\chi_{\alpha_i}(j)\right] \tag{4.1}$$

where $\mathbf{r}_j$ are the coordinates of the particles, $Z \equiv \{\mathbf{Z}_i; i = 1, ..., A\}$ are complex variables corresponding to the position (real part) and momentum (imaginary part) of the centroids of the Gaussian wave packets, ν is the width of a packet ($\nu = 0.16$ fm^{-2}), and $\chi_{\alpha_i}(j)$ are the spin-isospin states with $\alpha_i = p\uparrow, p\downarrow, n\uparrow, n\downarrow$.

The time evolution of the wave packet centroids Z is determined by the time-dependent variational principle

$$\delta\int_{t_1}^{t_2} dt\,\frac{\langle\Phi(Z)|i\hbar\frac{d}{dt} - H|\Phi(Z)\rangle}{\langle\Phi(Z)|\Phi(Z)\rangle} = 0 \quad \text{with} \quad \delta Z(t_1) = \delta Z(t_2) = 0 \tag{4.2}$$

from which the equation of motion for Z can be derived

$$i\hbar\sum_{j\tau} C_{i\sigma,j\tau}\frac{dZ_{j\tau}}{dt} = \frac{\partial H}{\partial Z^*_{i\sigma}} \tag{4.3}$$

where $C_{i\sigma,j\tau}$ with $\sigma, \tau = x, y, z$ is a Hermitian matrix given by

$$C_{i\sigma,j\tau} = \frac{\partial^2}{\partial Z^*_{i\sigma}\partial Z_{j\tau}}\log\langle\Phi(Z)|\Phi(Z)\rangle, \tag{4.4}$$

and $H(Z)$ is the expectation value of the Hamiltonian

$$H = \sum_{i=1}^{A}\frac{\mathbf{p}_i^2}{2M} + \sum_{i<j} v_{ij} \tag{4.5}$$

where v_{ij} is the effective force between nucleons.

The mean field contributions can be included in the Hamiltonian by adopting different expressions of the effective interaction. The AMD version used in this work implements the mean field via the Skyrme SLy4 effective interaction [104], with incompressibility modulus K_0=230 MeV and saturation density ρ_0=0.16 fm^{-3}. For the symmetry energy, the asy-stiff parametrisation is employed, with E_{sym}=32 MeV and L_{sym}=108 MeV. Only a single parametrization is adopted in this study. In the past, comparisons between AMD (or other transport models) with different parametrizations of the symmetry energy and experimental data have often been used to place constraints on the NEoS parameters [8, 40, 58, 105–107]. Unfortunately, the sensitivity

to the symmetry energy parametrization is very weak at these bombarding energies and it requires specific efforts and reaction combinations (such as ^{58,64}Ni+^{58,64}Ni of Refs. [59, 60]) to achieve reliable and useful conclusions on the subject [82]. Therefore, in the following, we will employ AMD with a single standard parametrization, which is sufficient for the purpose of this work.

Since we are interested in the description of heavy ion collisions at intermediate energies, it is very important that AMD includes also nucleon-nucleon (n-n) collisions beyond the mean field effects. The n-n collisions are treated as stochastic transitions from an AMD state to another, taking into account the Pauli blocking. The transition probability depends on the in-medium n-n cross section, which is a free parameter of the model. In the version used in this work, the parametrisation proposed in [108] is adopted

$$\sigma = \sigma_0 \tanh(\frac{\sigma_{free}}{\sigma_0}), \quad \sigma_0 = y\rho^{-2/3} \tag{4.6}$$

with the screening parameter y=0.85 (see [108]).

In the used version of the model, the final states may also include clusters. The cluster correlations have been introduced because the first version of AMD does not well reproduce the fragmentation yields in central collisions, underestimating the production of α particles in favour of nucleons [94]. Therefore, for each two-nucleon collision, cluster formation is considered for the final state. The differential cross section for the collision of two nucleons N_1 and N_2 with relative velocity v_{NN} forming two clusters (N_1 with nucleon B_1 form cluster C_1 and N_2 with nucleon B_2 form cluster C_2) is given by:

$$v_{NN} d\sigma(N_1 B_1 N_2 B_2 \rightarrow C_1 C_2) = \frac{2\pi}{\hbar} |M|_2 \delta(E_f - E_i) \frac{p_{rel}^2 dp_{rel} d\Omega}{(2\pi\hbar)^3} \tag{4.7}$$

where $\mathcal{M}$ is the scattering matrix for two nucleons with relative momentum p_{rel} and $\delta(E_f - E_i)$ enforces the conservation of energy. This approach also includes collisions without cluster formation where $N_j = C_j$. The final state is still represented by a Slater determinant and propagated by the AMD equation of motion. Moreover, a cluster can be broken colliding with other nucleons in the system.

The primary fragments produced by AMD are in a highly excited state. In this work the AMD calculations is stopped at 500 fm/c after the beginning of the interaction, as commonly done. In fact, that time is long enough to be sure that the dynamical phase is concluded and the mutual Coulomb repulsion between the primary reaction products is negligible. However, as it will be shown in Section 4.5, the actual interaction time approximately ends before 150-200 fm/c. Therefore, the statistical decay of reseparated fragments can start already within the AMD simulation.

4.2 GEMINI

Fragments produced within the dynamical code are still excited, well beyond the particles separation energies. For a complete description of the reaction we need to produce final state configurations, thus the following evolution is simulated by a statistical code used as afterburner. In our community, one of the most commonly used code is GEMINI [109], that is a Monte Carlo code developed by R. J. Charity for the description of the statistical decay of a compound nucleus. In this work, we used the C++ implementation of the code, GEMINI++ [98]. In general, GEMINI accepts as input a nucleus with charge Z, mass A, angular momentum J and excitation energy E^*. In this case, the output file of AMD is used as input for GEMINI. The procedure can be repeated many times for each primary events in order to increase the statistics. GEMINI treats each primary fragment as an excited system in thermal equilibrium. The de-excitation of the isolated excited source is performed through sequential decays until further decays are forbidden by the energy conservation laws. In GEMINI different formalisms are implemented in order to treat both the particle evaporation and the fission as possible decay channels. In particular, the particle evaporation is described with the Hauser-Feshbach formalism [110]. The fission probability is instead calculated within the Bohr-Wheeler formalism [111], except for the fission of light systems or the asymmetric fission of the heavier ones, for which the Moretto binary decay approach [112] is used. However, in the AMD+GEMINI++ simulation of Ni+Ni systems at 32, 52 and 74, as we will see in Section 5.3.1, about 85% of the QP breakups are produced by AMD during the dynamical phase of the reaction. Consequently, we can state that the primary role of GEMINI consists in the particle evaporation. For this reason, in the following we will only briefly describe how the Hauser-Feshbach formalism is implemented in GEMINI (more details in Ref. [98]). In the Hauser-Feshbach formalism, for the i-th particle evaporated from a nucleus with excitation energy E^* and total angular momentum J_{CN}, the partial decay width can be written as [109]:

$$\Gamma_i(E^*, J_{CN}) = \frac{1}{2\pi\rho_{CN}(E^*, J_{CN})} \int d\varepsilon \sum_{J_d=0}^{\infty} \sum_{J=|J_{CN}-J_d|}^{J_{CN}+J_d} \sum_{l=|J-S_i|}^{J+S_i} T_\ell(\varepsilon)\rho_d(E^*-B_i-\varepsilon, J_d) \tag{4.8}$$

where J_d is the total angular momentum of the daughter nucleus, S_i, J and ℓ are the spin, the total angular and orbital momentum of the evaporated particle, ε and B_i its kinetic and separation energies, T_ℓ its transmission coefficient and ρ_{CN} and ρ_d are the level densities of the compound nucleus and of the daughter nucleus. All the possible angular momentum couplings

between the initial and final states are included. In GEMINI, the Hauser-Feshbach formalism is implemented for n, p, d, t, ^{3,4,6}He, ^{6,7,8}Li, ^{7,9,10}Be. The level density is given by the Fermi-gas formula:

$$\rho_{Fg}(E^*, J) = \frac{2J+1}{24\sqrt{2}a^{1/4}U^{5/4}\sigma^3}e^S \quad \text{with} \quad S = 2\sqrt{aU} \tag{4.9}$$

where S is the nuclear entropy, a the level density parameter and U is the thermal energy obtained as :

$$U = E^* - E_{rot} = E^* - \frac{J(J+1)\hbar^2}{2I_{rig}} \tag{4.10}$$

namely the difference between the excitation energy and the rotational energy of a rigid rotor with the nuclear density and with a momentum of inertia I_{rig}. GEMINI generalizes Eq. 4.10 by replacing $E_{rot}(J)$, the rotational energy of a spherical nucleus of fixed moment of inertia, with the Yrast energy $E_{yrast}(J)$, in order take into account the rotation-induced nuclear deformation. The transmission coefficient T_ℓ is determined from the experimental available data of the inverse reaction by using the incoming-wave boundary-condition (IWBC) model [98]. In order to fit the low-energy region of the experimental light-particle kinetic energy spectra, a distribution of Coulomb barriers must be introduced. This distribution could arise from thermal fluctuations of the nucleus shape and/or fluctuations in the diffuseness of the nuclear surface or nuclear size. In GEMINI, in order to include the effects of barrier distribution, the transmission coefficients are calculated averaging over three IWBC transmission coefficients associated with three different radii (R_0 and $R_0 \pm \delta r$) of the nuclear potential:

$$T_\ell(\varepsilon) = \frac{T_\ell^{R_0-\delta r}(\varepsilon) + T_\ell^{R_0}(\varepsilon) + T_\ell^{R_0+\delta r}(\varepsilon)}{3} \tag{4.11}$$

where R_0 is the nuclear potential radius of the initial nucleus and δr is proportional to the square root of the temperature of the daughter nucleus. In this work the standard parameters, tuned to reproduce experimental data from complete fusion reactions [98], are used.

It is worth mentioning that the evaporation process can substantially alter the characteristics of the primary fragments, as also their isospin content. In fact, the fragments obtained from the de-excitation of the hot primary fragments via particle evaporation tend to move in the chart of nuclides towards the so called Evaporation Attractor Line (EAL) [113], plotted on the chart of nuclides with a dotted line in Fig. 4.1. The solid curves show the evolution of the average Z and N of the secondary fragments, starting from

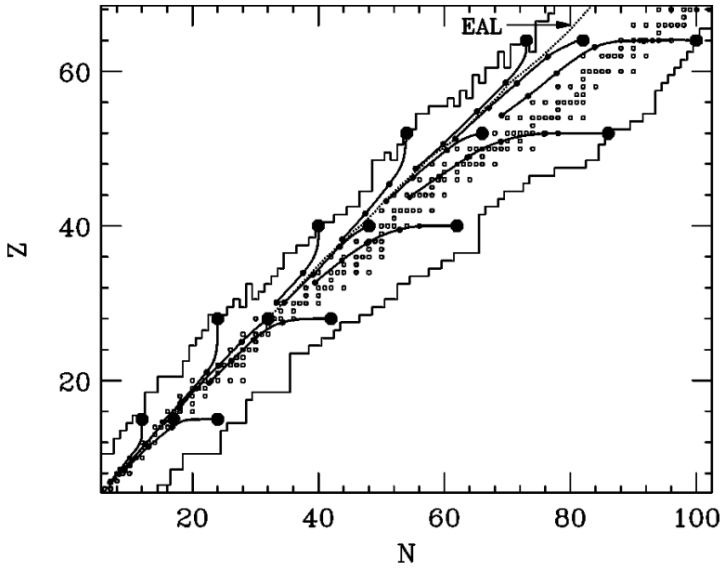

Figure 4.1: . The Evaporation Attractor Line plotted on the chart of nuclides (dotted line). The curves show the loci of the predicted average locations of secondary fragments for the compound nuclei indicated by the large solid points. The small points correspond to the average location of secondary fragments as the excitation energy increases. Figure taken from [113].

different compound nuclei (large solid points). For compound nuclei on the neutron-rich (neutron-poor) side of the line, neutron (proton) emission prevails and this drives the system towards the line. The final position of the secondary fragments depends also on its excitation energy: the average location of the residues as the excitation energy increases are shown with small solid markers. The lines clearly approach the EAL. The evaporation attractor line obtained from the GEMINI calculations can be well approximated by

$$Z = 0.909N - 1.12 \cdot 10^{-3}N^2 \tag{4.12}$$

and for light and medium mass nuclei is quite close to the beta stability.

4.3 HIPSE and SIMON

HIPSE (Heavy-Ion Phase-Space Exploration) [99] is an event generator dedicated to the description of nuclear collisions in the Fermi energy domain. Unlike AMD that is a microscopic transport model, HIPSE is a phenomenological model in between the statistical and the microscopic approaches. It

describe the reaction in three steps:

- The first step is the approaching phase of the collision which ends when the two colliding nuclei are at the maximum overlap. This phase is simulated by solving the classical equation of motion of the two partners in their mutual interaction potential. At that time, the two nuclei are described by a collection of nucleons whose momentum and space distributions correspond to their ground-state boosted by the relative momentum and distance associated with maximum overlap between the two incoming nuclei.

- Successively, during the partition-formation phase, the rearrangement of the nucleons into several clusters and light particles takes place. The partition is built following coalescence rules in momentum and position spaces with the consequence that the characteristics of the species produced in highly fragmented collisions will keep memory of the entrance channel.

- The last step is the exit channel and afterburner phase. The partition is propagated taking into account re-aggregation effects due to the nuclear and Coulomb interactions among the various species of the partition. Since these latter can be produced in excited states, the secondary decays are taken into account by SIMON [100], an evaporation code that simulates all the possible decay channels using an approach similar to that of GEMINI.

It is worth noting that in HIPSE the isospin transport phenomena are not included. More detail about these three stages can be found in [99].

4.4 Filter and first comparison with experimental data

The simulated data to be compared with the experimental ones must be filtered through a software replica of the apparatus. The filter accounts for the geometrical coverage of the setup, the energy thresholds for both the Z and A identification (extracted for each detector from the experimental data), the energy resolution and the working status of each detector. For this purpose we used kaliveda-sim, a software which is part of the Kaliveda package. This software allows to filter the simulated data according to the specific experimental conditions of each campaign.

As an example, the effect of the filter is illustrated in Fig. 4.2, which shows the correlation between the charge Z and the component of centre of mass velocity along the beam axis v_z^{cm} for the simulated AMD+GEMINI++ secondary fragments in the ^{58}Ni+^{58}Ni reaction at 74 AMeV. In panel (a) the 4π distribution is displayed, while panel (b) shows the result after applying the filter. The absence of neutrons, which cannot be detected by the apparatus, is evident, as well as the depletion in the QT region due to the identification thresholds.

The filtered simulated secondary fragments are now directly comparable with the experimental data and will be treated in the same way.

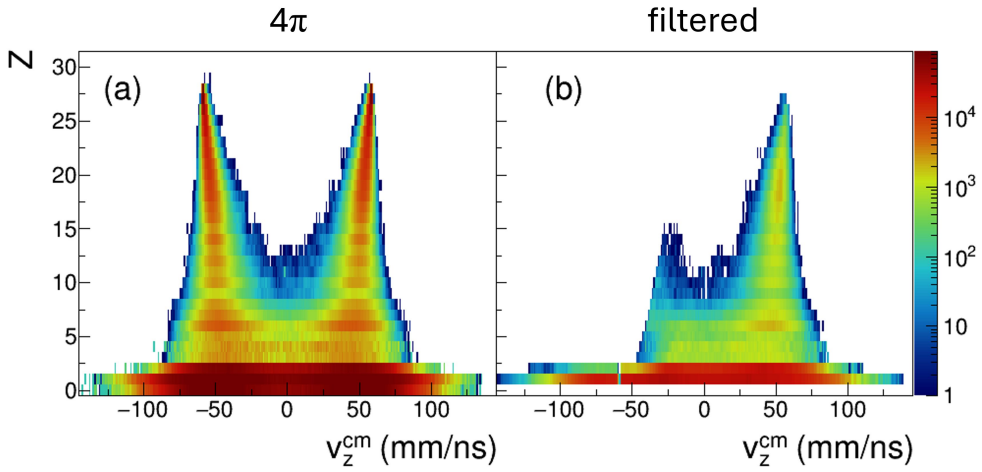

Figure 4.2: Z vs v_z^{cm} correlation of the AMD+GEMINI++ secondary fragments for the ^{58}Ni+^{58}Ni reaction at 74 AMeV. Panel (a): 4π simulation. Panel (b): filtered simulation. The colour scale is logarithmic and indicates the number of fragments in each bin.

For a preliminary comparison between experimental and simulated observables, both AMD+GEMINI++ and HIPSE models are considered. Fig. 4.3 provides a general overview of the particles produced in the reaction using the Z vs v_z^{cm} correlation for the reaction at 74 AMeV. Panel (a) corresponds to experimental data, while panels (b) and (c) show the results of the AMD+GEMINI++ and HIPSE filtered simulations, respectively Both simulations well reproduce the main features of the experimental distribution. However, some differences are clearly noticeable though qualitatively. The AMD+GEMINI++ simulation tends to less populate the region around $v_z^{cm} \sim 0$. Instead, the HIPSE simulation underestimates the production of heavy QP residues especially with Z>10.

The differences can be more quantitatively appreciated in Fig. 4.4, where

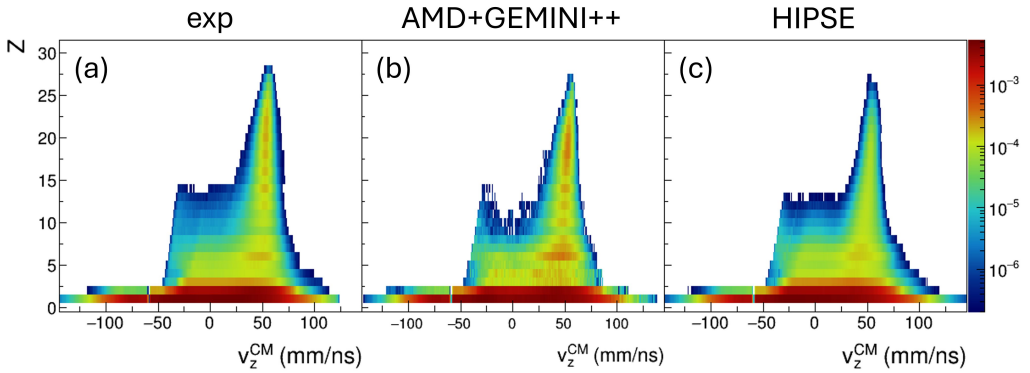

Figure 4.3: Z vs v_z^{cm} correlation of fragments produced in the ^{58}Ni+^{58}Ni reaction at 74 AMeV for the experimental data (panel (a)) and the filtered AMD+GEMINI++ (panel (b)) and HIPSE (panel (c)) simulations. The plots are normalised to their integral. The colour scale is logarithmic and indicates the probability of each bin.

the projections of the correlations of Fig. 4.3 are shown. From the charge distributions in panel (a), we observe a good agreement between AMD+GEMINI++ and the experimental data, with only a slight underestimation of the heavier fragments in the simulation. Also, in the region up to Z around 16, the yield odd-even staggering in the experimental data is well reproduced by the model. Instead, HIPSE favours too dissipative events as indicated by the strong underestimation of the heavy fragment yields and doesn't reproduce the staggering perhaps for a less accurate description of final-state nuclei after the decay. The velocity distributions (panel (b)) further confirm this trend: HIPSE underpredicts the peak associated with quasi-projectile region, while overestimates the yield in the midvelocity region ($v_z^{CM} \sim 0$). The AMD+GEMINI++ simulation, on the other hand, tends to underpopulate this mid-velocity region with respect to the experimental data, as it will be shown in Chapter 7 with a more complex and dedicated analysis. Overall, however, the agreement between experiment and AMD+GEMINI++ simulations is satisfactory, whereas HIPSE shows more significant discrepancies. The AMD+GEMINI++ simulations at 32 and 52 AMeV, not shown here, also display good agreement with the experimental data, as previously reported in [86].

In the following chapters, we will adopt AMD+GEMINI++ as the main reference model; however, for the reaction at 74 AMeV we will also exploit the events produced by HIPSE to double-check the efficiency estimation for the light fragments (Z<5) as discussed in Section 6.2.1.

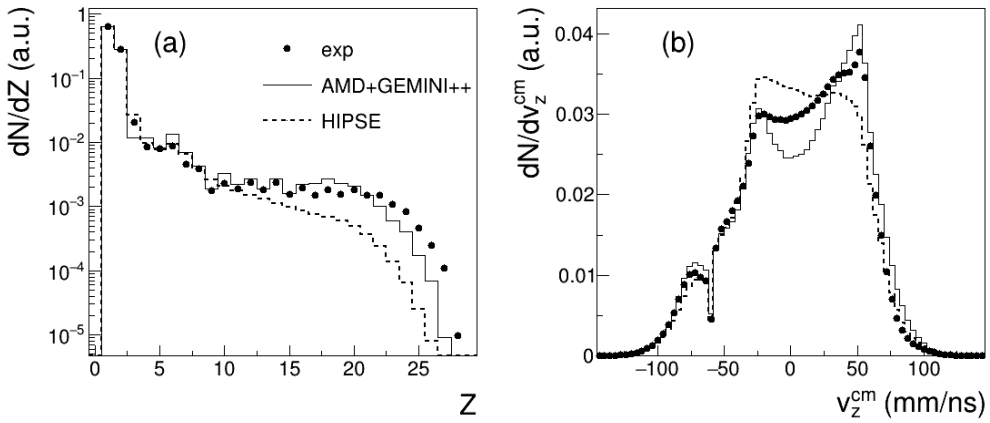

Figure 4.4: Experimental data vs model predictions for the Z (panel (a)) and v_z^{cm} (panel (b)) distributions for the ^{58}Ni+^{58}Ni reaction at 74 AMeV. The histograms are normalized to their integral.

4.5 The dynamical phase within AMD

Before proceeding with the analysis of the experimental data, we can take advantage of the AMD events to describe some predicted features of the dynamical phase of the ^{58}Ni+^{58}Ni reaction at 32, 52, and 74 AMeV, as the very important investigation of the reaction times.

As already mentioned, the AMD calculations are stopped at 500 fm/c, that is a duration longer than typical separation times for our reactions. Thus, it is useful to investigate in more details when the interaction effectively ends for the two reaction channels investigated in this work: the QP evaporation (QPr) and the QP breakup (QPb) channels. For this purpose, the AMD fragment recognition algorithm was applied every 20 fm/c in the interval between 0 and 500 fm/c. This procedure makes it possible to identify the separation time, defined as the earliest time at which at least two heavy fragments re-emerge from a single hot reacting system. The selection criteria for the two channels of interest were slightly modified compared to those used for the experimental data (described in Chapter 5) to adapt them to the 4π case. For the QPr channel, events are required to contain a secondary fragment with Z>14 emitted forward in the centre of mass reference frame, accompanied only by light fragments with Z<5. For the QPb channel, events containing two big secondary fragments (Z>4), both emitted forward in the c.m. reference frame and with a total charge of at least 15, are selected.

The average separation times $\langle t_{sep} \rangle$ for these selected channels are shown in Fig. 4.5 as a function of the reduced impact parameter b_{red}. Each colour

corresponds to a different beam energy, while the full and open markers refer to the QPr and QPb channels, respectively. Since the analysis focuses on semiperipheral collisions, the figure is limited to $b_{red} \geq 0.4$. The extracted

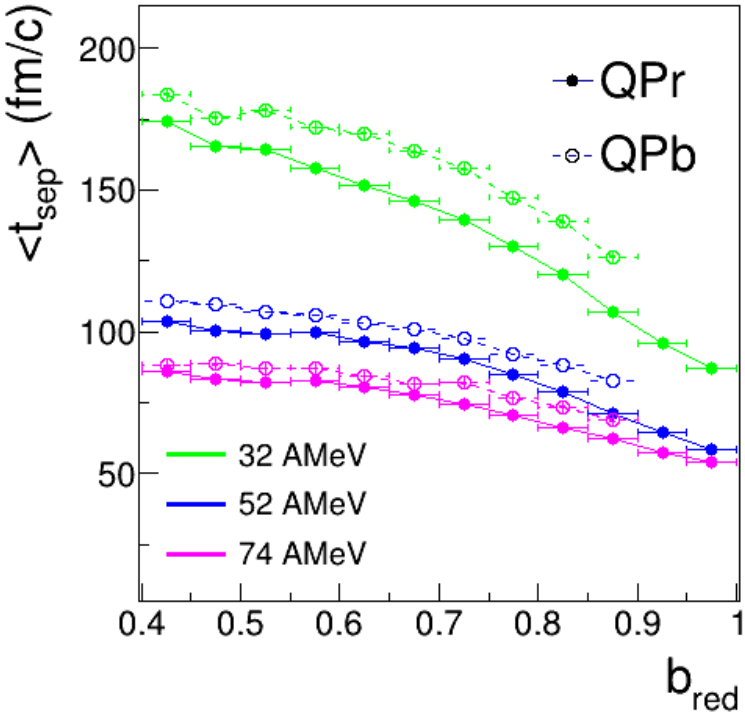

Figure 4.5: Average separation times $\langle t_{sep} \rangle$ as a function of b_{red} extracted from the 4π AMD+GEMINI++ simulations for the QPr (full markers) and the QPb (open markers) channels at 32 (green), 52 (blue) and 74 (magenta) AMeV.

$\langle t_{sep} \rangle$ values, well below 500 fm/c as expected, increase with the centrality of the reaction and scale correctly with the beam energy. Furthermore, as already pointed out in [60], slightly longer separation times appear, on average, to be associated with the QPb channel compared to the QPr channel, consistently for all beam energies.

Assuming that the separation time in AMD approximately corresponds to the end of the dynamical phase, it is interesting to examine the properties of the excited QP* at that moment and compare them with those at later times.

Fig. 4.6 displays the average atomic number $\langle Z \rangle$ as a function of b_{red} for the QP in the QPr (left column) and QPb channels (right column) at different times: at the separation time, at 500 fm/c and after the statistical

de-excitation. As a reference, the black line indicates the charge of the projectile ($Z = 28$). In the QPr channel, at the separation time, the charge of the QP in the most peripheral collisions ($b_{red} > 0.7$) remains close to that of the initial projectile and, despite the different average separation times obtained at the three incident energies for a given b_{red} bin, the average QP charge shows no dependence on the beam energy. With increasing centrality, however, a different behaviour emerges: at 74 AMeV the QP size decreases as expected, while at 32 AMeV it increases due to the contribution of incomplete fusion (see Fig. 5.1), with a smaller effect also visible at 52 AMeV. For the QPb channel, the trend of $\langle Z \rangle$ shows a slight decrease with centrality and no dependence on the beam energy. Apart the contribution of incomplete fusion observed in the QPr channel, the overall trend in the two channels is similar. At 500 fm/c, when the AMD calculation is stopped, the $\langle Z \rangle$ of the QP has significantly decreased in both channels. This indicates that, after separation (or shortly afterwards), the de-excitation already takes place within AMD. The nature of these emissions is expected to be predominantly statistical, as the separated sources are assumed to be close to equilibrium at such times. In both QPr and QPb channels, larger QPs are observed at 32 AMeV compared to the higher energies, which instead display very similar values. However, while in the QPr channel this difference can again be traced back to possible incomplete fusion, such contamination cannot be present in the QPb channel. Finally, similar considerations can be drawn for the charge of the QP after statistical evaporation, whose size is further reduced.

Fig. 4.7 shows the average excitation energy per nucleon $\langle E^*/A \rangle$ as a function of b_{red} for the QP in the QPr (left column) and QPb channels (right column) at the separation time and at 500 fm/c. At the separation time, in both channels the excitation energy evolves with the impact parameter. At 32 AMeV the $\langle E^*/A \rangle$ is systematically lower than at the higher energies, which are very similar to each other. Unlike what was observed for the QP charge, differences appear between the two channels for the higher beam energies: the QPb channel is characterized by larger $\langle E^*/A \rangle$ values compared to the QPr one. At 500 fm/c the excitation energy per nucleon has decreased, reaching very similar values across the two channels and for all incident energies.

In summary, an interesting observation can be done in the model predictions. In the QPb channel. Up to 500 fm/c, the behaviour at 32 AMeV is quite different from that at higher energies; namely at t_{sep} the excitation energy deposited at 32 MeV is lower. Thus, the initial decay, starting from almost equal charge nuclei, leads to heavier residues at 32 AMeV than at 52 and 74 AMeV at 500fm/c; as a consequence a compensation effect occurs, leading to a similar excitation energy density at this time for all beam energies. Finally, the footprint of the initially lower excitation energy density at

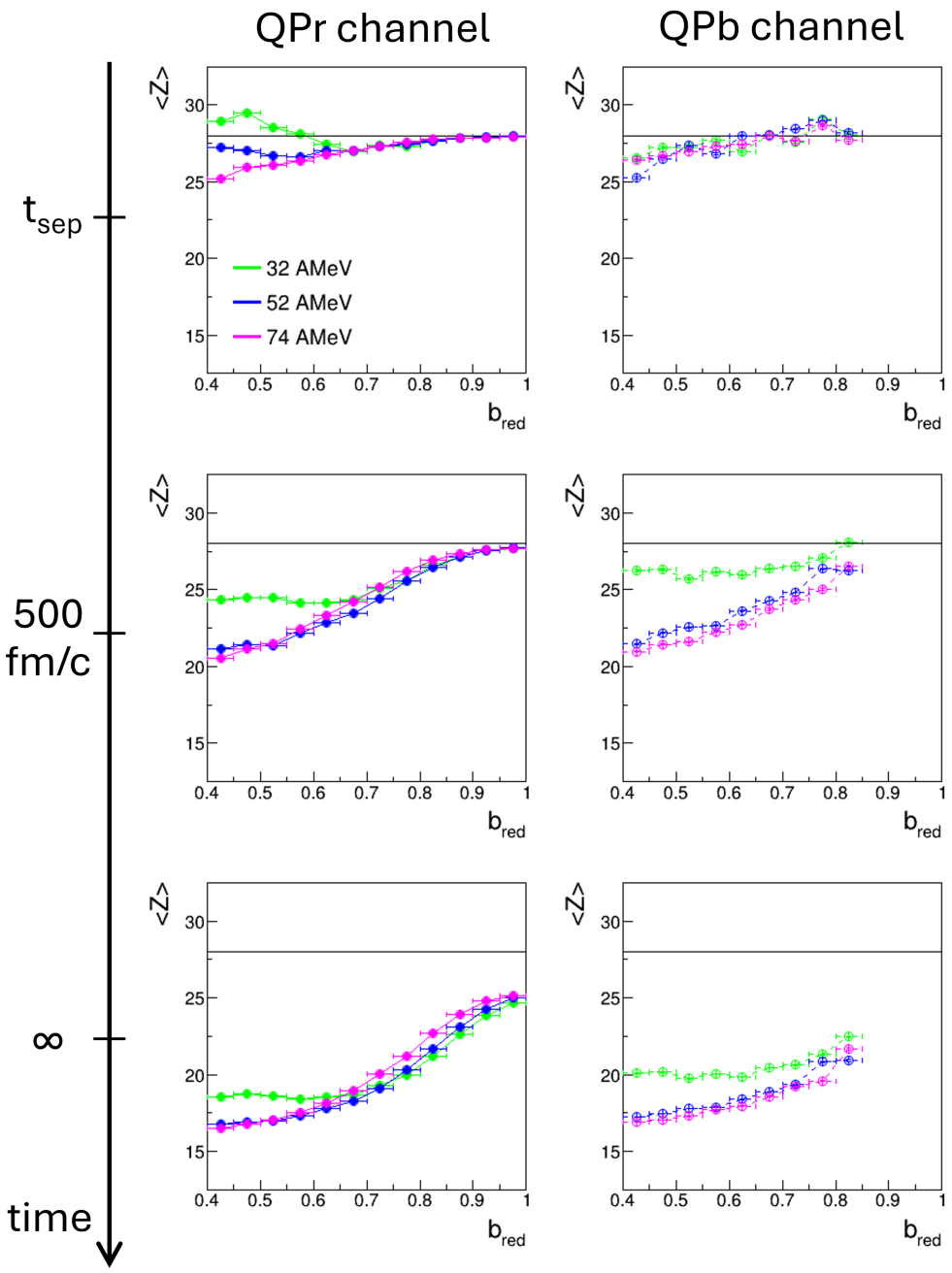

Figure 4.6: Average atomic number $\langle Z \rangle$ of the QP as a function of b_{red} for the QPr (left) and QPb (right) channels at different times: at the separation time, at 500 fm/c and after the afterburner. The black lines show the charge of the projectile (Z=28).

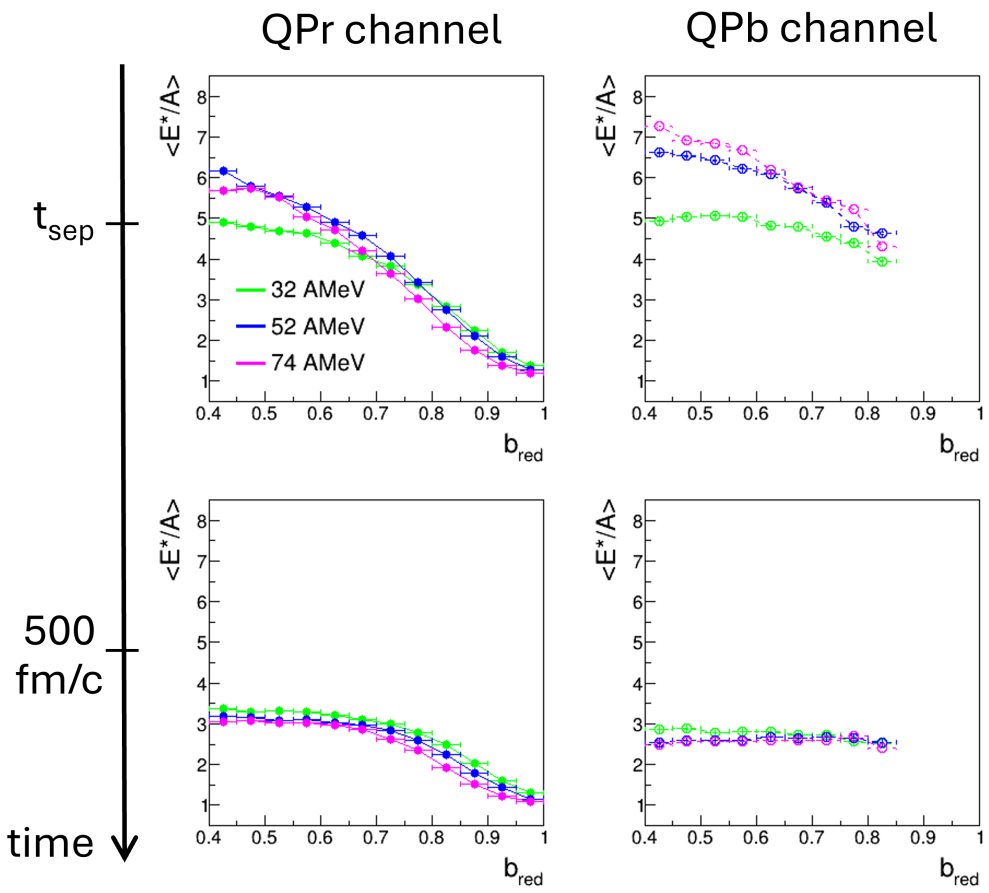

Figure 4.7: Average excitation energy per nucleon $\langle E^*/A \rangle$ of the QP as a function of b_{red} for the QPr (left panel) and QPb (right panel) channels at different times: at the separation time and at 500 fm/c.

32 AMeV persists in the model prediction of heavier secondary nuclei compared to the 52 and 74 AMeV reactions. A similar trend is observed also for the less peripheral collisions in the QPr channel, although in this case some contamination from incomplete fusion may be present.

In Chapter 7, the reconstruction of the primary excited QP* in the QPr and QPb selected channels will be attempted for both the experimental and simulated data. It is worth noting that the simulation results, treated in the same way as the experimental data, will yield characteristics of the primary QP* that are intermediate between those observed here at t_{sep} and 500 fm/c.

Chapter 5

Selection and characterization of the reaction channels

In the first chapter, the possible exit channels of a semiperipheral heavy ion collision at Fermi energies have been described. It is well known that the most probable reaction channel is the binary one, leading to the formation of a quasi-projectile and quasi-target. In some cases, the system can evolve into highly deformed configurations, resulting in the breakup of the QP and/or QT. Since the QT phase space is less accessible due to the identification thresholds of the setup, this analysis will focus on the particles associated with the QP phase space, keeping in mind that, considering the symmetry of the reaction, the characteristics of the QT are expected to be similar to those of the QP.

The aim of this chapter is to select the QP evaporation (QPr) and the QP breakup (QPb) channels. The detailed criteria adopted for the selection of these channels are presented below, together with a description of their general characteristics. In addition, the predictions of the AMD+GEMINI++ transport model, analysed using the same selection procedure, are compared with the experimental results.

To select the two reaction channels, the multiplicities of different particle types must be evaluated for each event. For clarity, in the following the fragments will be classified as:

- Z=1,2 Light Charged Particle (LCP)
- Z$\leq$4 light particles/fragments
- Z>4 Big Fragment (BF)
- Z>14 QP-like Fragment (QP)

5.1 Preliminary event selection

Before selecting the channels of interest, a preliminary event selection based on global variables was performed.

Since the trigger condition in the E789 experiment required M≥2 in FAZIA, the same selection criterion was consistently applied across all energies for both experimental and simulated data. Additionally, some spurious coincidences were discarded by requiring that the total charge, mass, and momentum along the beam axis of the detected particles do not violate conservation laws by exceeding those of the initial system: $Z_{tot} \leq 56$, $A_{tot} \leq 116$ and $p_z^{tot}/p^{beam} \leq 1.1$, to account for possible energy calibration errors. Finally, the most incomplete events were excluded by imposing a condition on the total detected charge: $Z_{tot} \geq 12$.

Tab. 5.1 reports the percentages of selected events for both the experimental and simulated data. The lower percentages of selected events in the AMD+GEMINI++ filtered simulations at 32 and 52 AMeV are due to the fact that the M≥2 condition is applied as a selection criterion, rather than as a trigger condition as in the experimental data. At 74 AMeV, where a minimum-bias trigger was used, the percentages are more similar.

	exp	**simul**
32 AMeV	52 %	23 %
52 AMeV	57 %	33 %
74 AMeV	43 %	42 %

Table 5.1: Percentages of selected events, as defined in the text, with respect to the total number of events for experimental data and AMD+GEMINI++ filtered simulations.

All further selections in the following analysis will be applied within this set of selected events.

5.2 Selection of the QP evaporation channel

In the QP evaporation channel, after the interaction between the projectile and the target, a primary quasi-projectile is formed, which subsequently decays through the evaporation of light particles. This channel, after the secondary decay, is therefore characterized by the presence of a single big fragment, namely the QP remnant, accompanied only by light fragments (Z<5). In the following, we will refer to this channels as QPr channel. To be identified as the QP remnant, the big fragment must be emitted forward in

the centre of mass reference frame and must have $Z > 14$, corresponding to at least 50% of the original projectile charge. This lower limit is consistent with the criteria adopted in previous works [40, 58, 59].

Summarizing, the conditions for a QPr event are:

- $M_{BF} = 1$
- $Z_{BF} > 14$
- $v_z^{cm} > 0$

The percentages of QPr events for both the experimental and simulated data are reported in Tab. 5.2. For experimental data and filtered simulations, the percentages are calculated with respect to the number of selected events at each energy, while for the 4π simulations they are normalized to the total number of events. From the 4π simulations it is confirmed that, for all incident energies, the QPr channel is the dominant one. However, these percentages are significantly reduced when considering the experimental and filtered simulation data, mainly due to the lack of coverage at very forward polar angles in the FAZIA setup ($\theta_{lab}^{min} \sim 1.4°$ for the reaction at 32 and 52 AMeV and 1.9° at 74 AMeV).

	exp	**simul**	**simul 4π**
32 AMeV	39 %	45 %	72 %
52 AMeV	27 %	32 %	65 %
74 AMeV	20 %	21 %	68 %

Table 5.2: Percentages of QPr events for experimental and filtered AMD+GEMINI++ simulation data with respect to the selected events. For the 4π AMD+GEMINI++ simulations, the percentages are calculated with respect to the total number of events.

In principle, the selection of the QPr channel may be contaminated by events in which two or more BFs are produced, but only one - satisfying the imposed conditions - is detected. Nevertheless, the simulations indicate that nearly 99% of the events selected in this way correspond to QP evaporation. Only a small fraction, slightly above 1%, are misclassified as QPr events due to the limited geometrical coverage of the apparatus.

As first inspection of this event class, Fig. 5.1 displays the correlations between the atomic number Z and the velocity along the beam axis in the centre of mass reference frame v_z^{cm} of the QP remnant, for experimental data (upper panels) and filtered AMD+GEMINI++ simulations (lower panels).

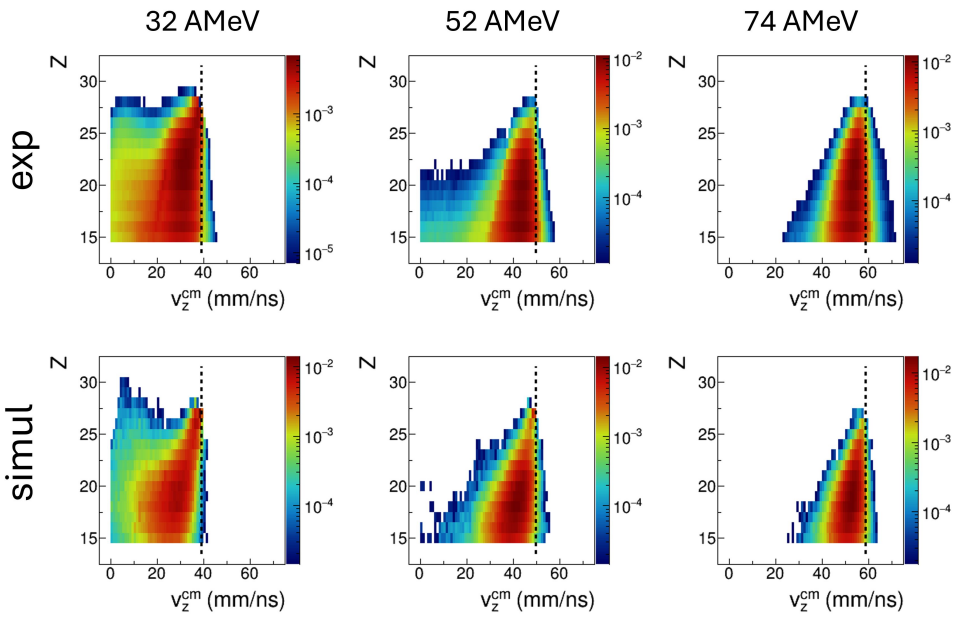

Figure 5.1: Experimental and filtered AMD+GEMINI++ correlations between the atomic number Z of the QP remnant and its velocity along the beam axis in the centre of mass reference frame v_z^{cm}. All correlations are normalized to their integral. The dashed black line represents the velocity of the projectile (Z=28).

The black lines indicate the projectile velocity in the cm reference frame v_{proj}^{cm}. In each correlation, the QP remnant tends to the velocity of the original projectile. For the reaction at 32 AMeV, also the region at $Z \gtrsim Z_{proj}$ and $v_z^{cm} \sim 0$ is partially populated, which is consistent with incomplete fusion processes. With increasing incident energy, this channel gradually disappears, as central collisions become dominated by multifragmentation or even vaporization processes. Overall, a good agreement can be observed between the experimental and simulated QPr events across all incident energies.

A more detailed view of the QP remnant properties is provided in Fig. 5.2, where the distributions of the charge Z (panel (a)), the velocity component along the beam axis v_z^{cm} (panel (b)), and the scattering angle θ^{cm} (panel (c)) are displayed. The different colours correspond to the three incident energies. Histograms plotted with markers represent the experimental data, while those drawn with lines correspond to the AMD+GEMINI++ simulations. All distributions are normalized to unit area. Some differences between the model predictions and the experimental observations can be noticed in the Z distributions (panel (a) of Fig. 5.2). In particular, the QP remnants in

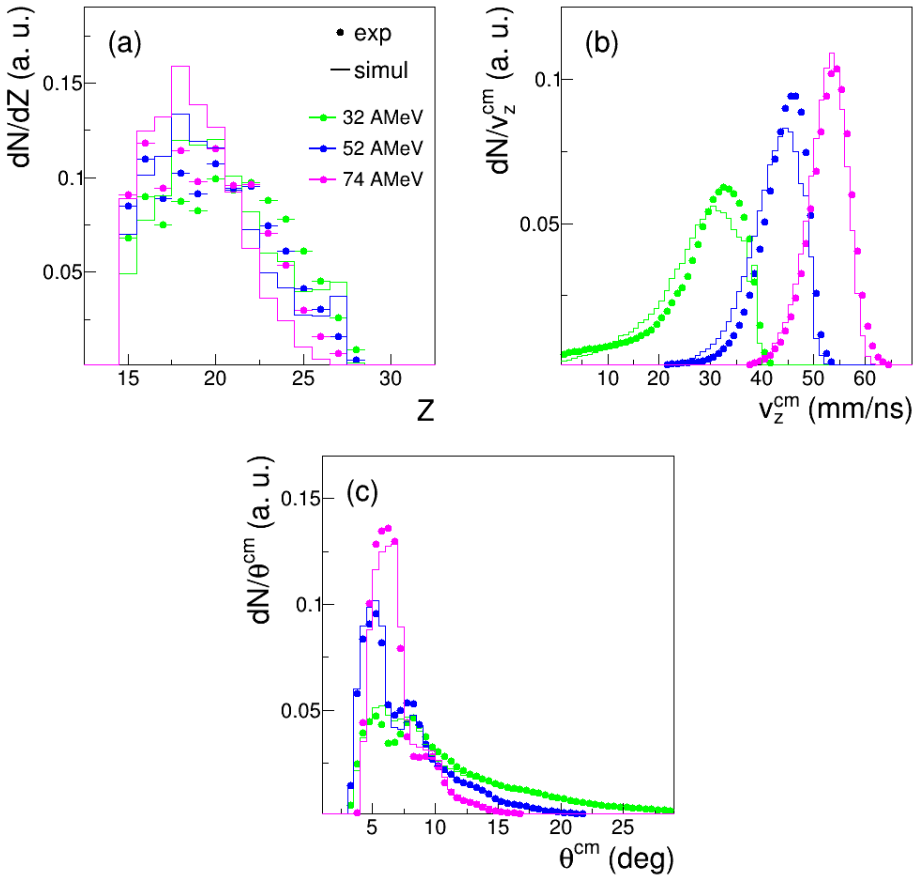

Figure 5.2: Comparison between the experimental (markers) and simulated (lines) distributions of Z (panel (a)), v_z^{cm} (panel (b)) and θ^{cm} (panel (c)) of the QP remnant in the QPr channel. All histograms are normalised to their integral.

the experimental data tend to be slightly heavier than those in the simulations, suggesting a higher degree of dissipation in the model. Across the three energies, the Z distributions appear rather similar, although the selected QPr remnants at 32 AMeV are on average slightly heavier, likely due to a contamination from incomplete fusion. For the v_z^{cm} distributions (panel (b)), the agreement between experimental and simulated data is generally good. However, the simulated QP exhibit on average a slightly lower velocity than in the experimental data, again pointing to an overestimation of dissipation in the model. This effect is most evident at 32 AMeV and becomes progressively less significant with increasing beam energy, nearly vanishing at 74 AMeV. Finally, the θ^{cm} distributions (panel (c)) show very good agreement

between experiment and simulations, reproducing well the trend and the cut-off at low θ^{cm} which reflects the absence of coverage at small forward angles. The excellent match between experimental and simulated data demonstrates both the good reproduction of this parameter by the model and how the experimental filter is able to correctly reproduce the geometrical acceptance of the apparatus. The differences observed in the distributions of the three incident energies can be attributed to the different reaction kinematics.

Further insight into the QPr events can be obtained by analysing the emission pattern of the light fragments detected in coincidence with the evaporation residue. For such a reason, it is necessary to select, as best as possible, light fragments which can be attributed to the QP phase-space using a kinematic constrain: fragments are required to be emitted in the forward hemisphere of the centre of mass reference frame , i.e. $v_{\parallel}^{cm} > 0$, where $v_{\parallel}^{cm}$ is the velocity component (in the cm frame) along the asymptotic QP-QT separation axis. The proposed selection is sketched in Fig. 5.3 as the non-dashed region. This selection strongly suppresses contributions

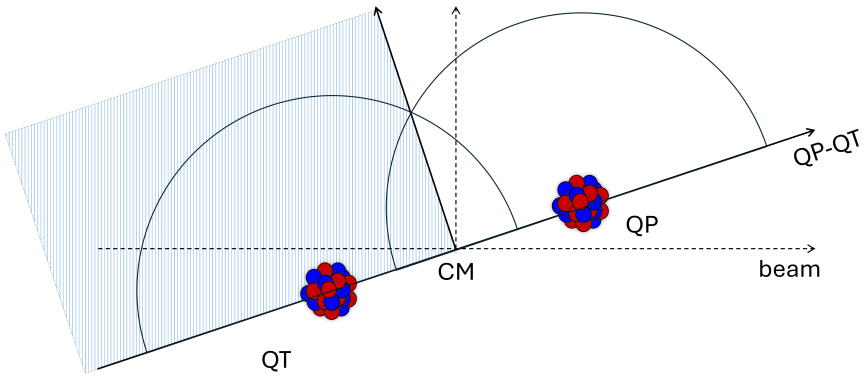

Figure 5.3: Sketch of the kinematic selection used to identify light fragments associated with the QP phase-space. The non-shaded region, corresponding to particles with a centre of mass velocity component along the QP-QT axis $v_{\parallel}^{cm} > 0$, represents the adopted the selection.

from the QT. However, using this selection a part of the QP kinematic circle is missing, while a part of the QT one is included. Nonetheless, due to the symmetry of the system, any residual QT contribution is expected to have average yields and multiplicities identical to those of the QP particles excluded by this selection.

Fig. 5.4 shows the correlations between the velocity components parallel ($v_{\parallel}$) and perpendicular ($v_{\perp}$) to the beam direction in the QP reference frame for protons, deuterons, α particles and lithium detected in the QPr channel,

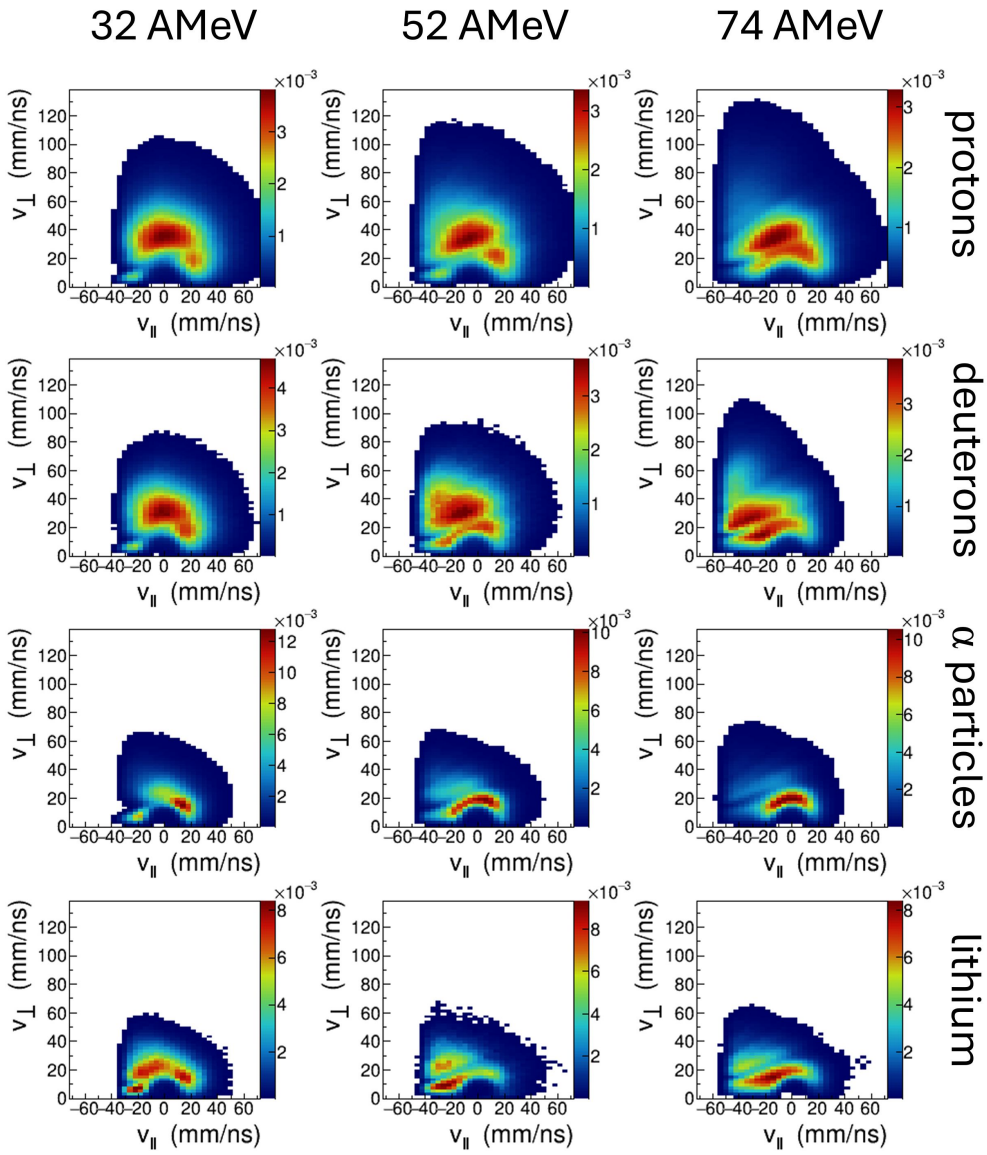

Figure 5.4: Experimental correlations for the three beam energies between the perpendicular $v_\perp$ and parallel $v_\parallel$ components of the velocities in the QP reference frame for protons, deuterons, α particles and lithium in coincidence with the QP remnant. The correlations are normalised to their integral.

using the kinematic condition illustrated in Fig. 5.3. To properly account for relativistic kinematics, $v_{\parallel}$ and $v_{\perp}$ are actually replaced by the rapidity y and the transverse velocity $\beta_{\perp}$. The rapidity is defined as

$$y = \frac{1}{2} \ln[\frac{1+\beta_{\parallel}}{1-\beta_{\parallel}}] \tag{5.1}$$

where $\beta_{\parallel}$ is the velocity component parallel to the beam axis, normalized to the speed of light c, and $\beta_{\perp}$ is the corresponding component perpendicular to the beam. In the following, in all plots y and $\beta_{\perp}$ multiplied by c will be used; for simplicity they will be denoted as $v_{\parallel}$ and $v_{\perp}$.

As shown in Fig. 1.2, the thermal emission from a source is expected to produce well defined Coulomb circles, but in Fig. 5.4, particularly at higher energies, clear distortions are observed, mainly due to some inefficiencies in the experimental apparatus (the dead zone between the FAZIA and INDRA apparatuses and the limitations in the Z=1 mass identification in some of the INDRA CsI(Tl) crystals).

The corresponding plots for the filtered AMD+GEMINI++, an example is shown in the left panel of Fig. 5.5 for protons at 74 AMeV, look very similar to the experimental ones, demonstrating that the efficiency effects are well under control in the apparatus filter. For comparison, the right panel shows the well-defined Coulomb circle obtained from the full 4π simulation.

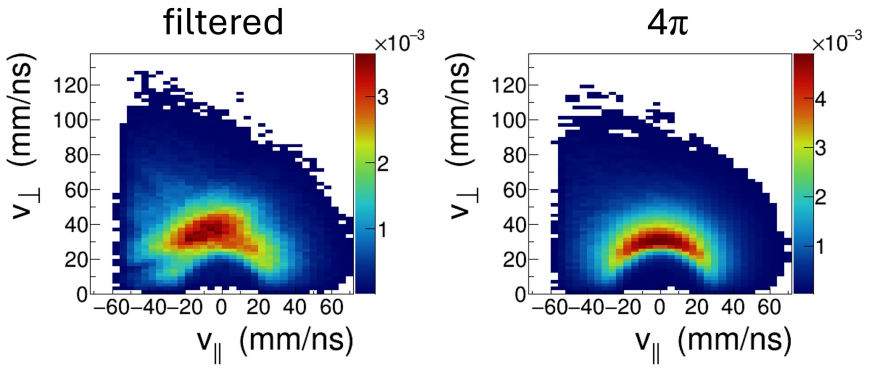

Figure 5.5: Filtered (left panel) and 4π (right panel) simulated correlations ($v_{\parallel}$,$v_{\perp}$) for protons at 74 AMeV. The correlations are normalised to their integral.

As discussed in Chapter 1, an enhancement of particle yield is observed at velocities intermediate between those of the QP and QT (corresponding to the region $v_{\parallel} < 0$ in Fig. 5.4). Although present for all particle species, this component is particularly pronounced for neutron-rich particles, such

as deuterons, and for the lithium ions. Moreover, one can observe that the relative population of the midvelocity component increases with the incident energy. Indeed, despite the distortions introduced by the experimental setup, at 32 AMeV the distributions remain closer to ideal Coulomb circles compared to those at 52 and 74 AMeV, where the midvelocity contribution is more significant. A more quantitative estimation of this component will be provided in Chapter 7.

5.3 Selection of the QP breakup channel

To select the QP breakup channel, events in which two big fragments are identified must be selected. Two different scenarios are then possible:

- QP breakup event: both detected BFs originate from the breakup of the QP.
- mixed event: one BF is related to the QP, while the other comes from the breakup of the QT.

Other possible scenarios, such as the presence of a QT remnant or the simultaneous detection of both the QT breakup fragments, are strongly suppressed by the geometrical acceptance of the apparatus and can therefore be neglected.

To distinguish between these two cases, we analyse the correlation between the relative angle (θ_{rel}) of the two BFs in the cm frame and their relative velocity (v_{rel}), as shown in the upper panels of Fig. 5.6 for the experimental data at the three energies. If both BFs originate from the QP breakup, θ_{rel} is expected to be small, whereas mixed events should exhibit larger θ_{rel} values, close to 180°. Additionally, v_{rel} in QP breakup events should be consistent with Coulomb-driven repulsion, while mixed events can show v_{rel} values exceeding those predicted by the Viola systematics [114]. In fact, applying an additional condition that selects only BFs emitted forward in the cm reference frame, thus making their attribution to the QP more probable, as shown in the lower row of Fig. 5.6, removes the component at large θ_{rel} and v_{rel}, particularly evident at 52 and 74 AMeV. Under this condition, a clean sample of QP breakup events was isolated by selecting those within the black rectangles.

Once the common origin of two fragments is confirmed, the quasi-projectile can be reconstructed. The two fragments were sorted according to their atomic number Z (and, in the case of equal charge, by their mass number). The heavier fragment is labelled with Heavy Fragment (HF), while the lighter

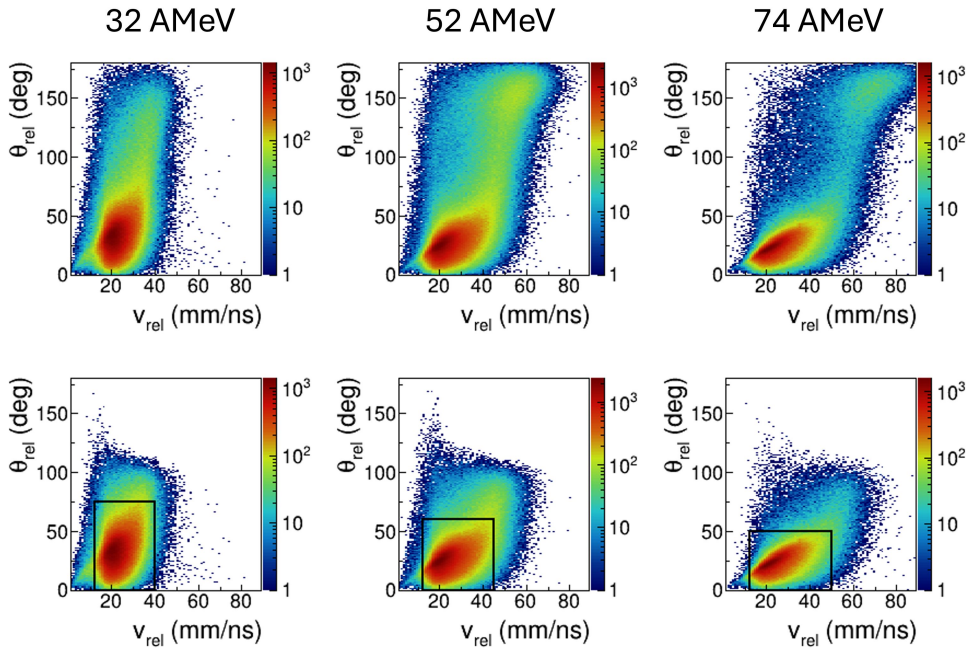

Figure 5.6: Upper row: experimental correlations between the relative angle in the cm reference frame θ_{rel} and the relative velocity v_{rel} of the two BFs for the three beam energies. Lower row: the same correlations restricted to events in which both BFs are forward emitted. The black rectangles mark the region used to select a clean sample of QP breakup events.

one (the second heavier fragment) is referred to as Light Fragment (LF). The QP is then reconstructed as a nucleus with charge $Z_{rec} = Z_{HF} + Z_{LF}$, mass $A_{rec} = A_{HF} + A_{LF}$, and velocity $\vec{v}_{rec}$ equal to the centre of mass velocity of the HF and the LF. The reconstructed QP is required to be emitted forward in the cm reference frame and to have a charge of at least 15.

In summary, the conditions adopted for the QP breakup event selection are:

- $M_{BF} = 2$
- $v_{BF_z}^{cm} > 0$
- $0 < \theta_{rel} < \theta_{rel}^{max}$
- 12 mm/ns $< v_{rel} < v_{rel}^{max}$
- Z_{rec}=Z_{HF}+Z_{LF} >14
- $v_{rec_z}^{cm} > 0$

where $\theta_{rel}^{max} = 75, 60, 50°$ and $v_{rel}^{max} = 40, 45, 50$ mm/ns for the reactions at 32, 52 and 74 AMeV, respectively.

This class represents a minor fraction of the statistics, as shown by the percentages reported in Tab. 5.3. The percentages for both experimental and simulated data are evaluated with respect to the total number of selected events.

	exp	**simul**
32 AMeV	4.2 %	3.6 %
52 AMeV	3.2 %	2.9 %
74 AMeV	2.2 %	2.7 %

Table 5.3: Percentages of the QPb channel with respect to the number of preliminary selected events for experimental data and filtered AMD+GEMINI++ simulations.

Similarly to Fig. 5.2, Fig. 5.7 shows the comparison between the charge Z, the velocity v_z^{cm}, and the diffusion angle θ^{cm} distributions of the reconstructed QP at all beam energies, for the experimental data (markers) and the AMD+GEMINI++ simulations (lines). The Z distributions (panel (a)) indicate a reconstructed QP heavier for the reaction at 32 AMeV, while at higher energies the distributions become rather similar. It is worth noting that, particularly at 74 AMeV, the mean value of the distribution coincides with the imposed cut at Z=15, which could make difficult the interpretation of mean values in the following chapters. However, as will be shown in Chapter 6 (see Fig. 6.5), this effect only partially affects the centralities that will be selected.

As already discussed for the QP remnant, the AMD+GEMINI++ simulations appear to be more dissipative: the reconstructed QP in the experimental data is, on average, heavier and faster than in the simulations. This discrepancy is more pronounced at 32 AMeV and gradually decreases with increasing beam energy, leading to a much better agreement at 74 AMeV. Concerning the θ^{cm} distributions of the reconstructed QP (panel (c)), the cutoff in the angular distributions due to the geometrical acceptance of the apparatus is not evident, since in this case the angular information is reconstructed from the diffusion angles of the two breakup fragments.

Comparing the distributions observed in the two reaction channels, the charge distributions (panels (a) of Figs. 5.7 and 5.2) are rather similar, especially at 32 AMeV. At 52 and 74 AMeV, however, the reconstructed QP from the breakup channel exhibits, on average, slightly lower charges compared to the QP remnant. A clearer difference emerges in the velocity distributions

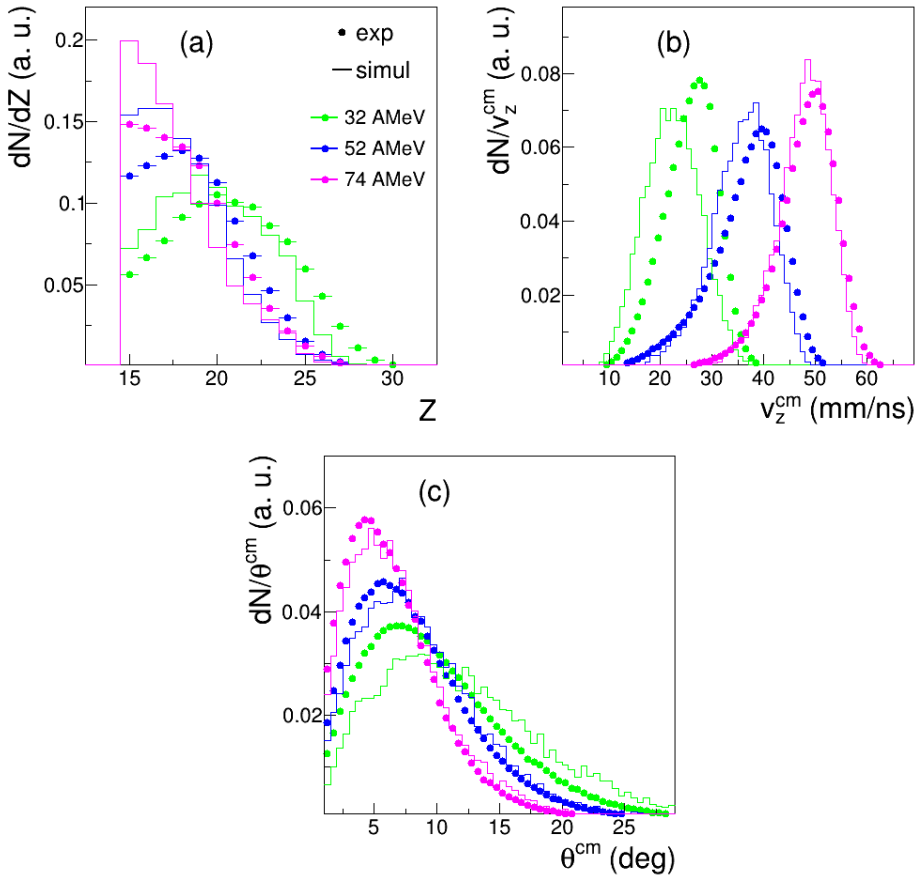

Figure 5.7: Experimental (markers) and simulated (lines) distributions of Z (panel (a)), v_z^{cm} (panel (b)) and θ^{cm} (panel (c)) of the reconstructed QP in the QPb channel. All histograms are normalised to their integral.

(panels (b) of Figs. 5.7 and 5.2): the velocities of the QP remnant are systematically higher than those of the reconstructed QP, suggesting that less dissipative events are selected in the QPr channel. These trends will be further discussed in Chapter 6, where a more systematic comparison between the two channels as a function of centrality will be presented.

5.3.1 Statistical vs dynamical origin of the breakup

The events selected in this channel can be generally interpreted as QP fissions. However, their dynamical or statistical origin remains to be clarified. It is therefore useful to investigate the properties of the two breakup fragments, since their characteristics may provide indications about the under-

lying mechanism.

As discussed in Chapter 1, to explore these decays, the relative angle α, defined such that $\cos(\alpha) = +1$ corresponds to the case of complete alignment with the LF emitted backward with respect to the HF, is commonly used [28–34]. In fact, the $\cos(\alpha)$ distributions can give insight into the statistical or dynamical origin of the breakup. In fact, for statistical processes one expects an isotropic distribution since it does not preserve the memory of the entrance channel and of the QP-QT separation axis. On the contrary, dynamical fissions occur in preferentially aligned HF-LF configurations, with the LF emitted backward, as the highly elongated and deformed QP is expected to break apart on a short timescale along the QP-QT separation axis.

To confirm this interpretation of the α angle, we can exploit the information provided by the AMD+GEMINI++ 4π simulations, which allow a direct separation of fissions of dynamical origin (produced by AMD) from those of statistical origin (produced by GEMINI++). Fig. 5.8 compares the total $\cos(\alpha)$ distributions (black) with the separate contributions of AMD (red) and GEMINI++ (green). The GEMINI++ distributions are flat, as

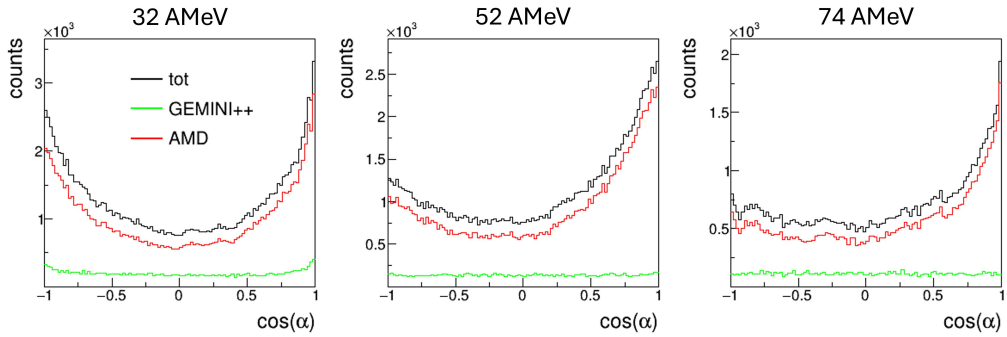

Figure 5.8: AMD+GEMINI++ 4π simulations: total $\cos(\alpha)$ distributions (black) compared with the separate contributions of AMD (red) and GEMINI++ (green). AMD breakups display anisotropy peaked at $\cos(\alpha) = 1$, consistent with dynamical fission, while GEMINI++ shows isotropic distributions.

expected for an isotropic statistical decay. The statistical component accounts for about 15% of the total yield, with only minor variations across the investigated energies. In contrast, the fissions produced in AMD display an anisotropic emission pattern fully consistent with a dynamical origin. At 32 AMeV, the AMD distribution exhibits a double-peaked structure with maxima at $\cos(\alpha) = \pm 1$. This behaviour indicates that the alignment along the QP-QT axis is still preserved, but the forward-backward emission of the LF remains nearly equiprobable. At higher energies, 52 and 74 AMeV,

the distribution becomes more asymmetric, with a clear enhancement at $\cos(\alpha) = 1$, indicating a preferential backward emission of the LF and a stronger dynamical character of the breakup.

Unfortunately, in the experimental data it is not possible to directly distinguish between dynamical and statistical breakups. In this case, however, the $\cos(\alpha)$ observable can be studied as a function of the charge asymmetry parameter η, defined as:

$$\eta = \frac{Z_{HF} - Z_{LF}}{Z_{HF} + Z_{LF}}. \tag{5.2}$$

where $\eta = 0$ corresponds to a symmetric split. In fact, the preferential asymmetry of the breakup represents another signature of a dynamical fission process. Fig. 5.9 shows the experimental $\cos(\alpha)$ distributions for three η intervals. For the most charge-symmetric splits ($0 \leq \eta \leq 0.2$), the $\cos(\alpha)$

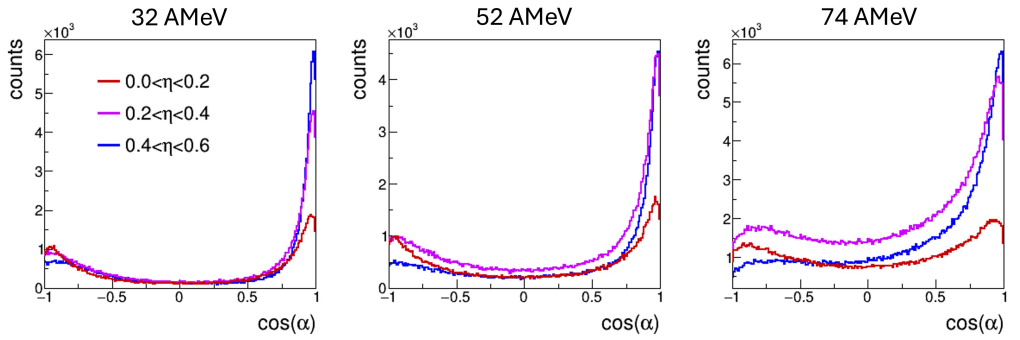

Figure 5.9: Experimental $\cos(\alpha)$ distributions for three intervals of charge asymmetry η.

distributions are nearly isotropic, consistent with a statistical process. On the contrary, more asymmetric breakups occur in preferentially aligned HF-LF configurations, with the LF emitted backward, in agreement with the a dynamical breakup. In the experimental data, symmetric splits account for about 25% of the QPb events, and comparable results are found for the filtered AMD+GEMINI++ simulations. However, it should be stressed that the correlation of the α angle to a time-clock of the process is not straightforward (see Ref. [33]); consequently, a symmetric split does not necessarily imply a purely statistical breakup.

5.4 Reaction centrality estimation

To investigate the evolution of the reaction dynamics, a key step is to achieve an event sorting according to the impact parameter b, which is the funda-

mental variable describing the centrality of a reaction. Since b cannot be measured directly, one has to rely on indirect methods, exploiting experimental observables strongly correlated with it.

Several impact parameter estimators are commonly employed. For instance, the LCP multiplicity M_{LCP} [115] and the transverse kinetic energy E_{trans}^{LCP} [2, 37] are widely used, provided that the apparatus ensures a good angular coverage to detect the emitted particles. Another frequently used estimator is the flow angle θ_{flow} [116], which reflects the global shape and orientation of the event and is particularly effective for the selection of central collisions [117]. When the angular coverage is limited, or when the focus is on semiperipheral collisions, observables related to the properties of the quasi-projectile can be adopted, such as the reduced momentum p_{red} [58], defined as:

$$p_{red} = \left(\frac{p_z^{QP}}{p^{beam}} \right)_{cm} \tag{5.3}$$

i.e. the component of QP momentum along the beam axis normalised to the beam momentum, both evaluated in the cm reference frame. Peripheral collisions are expected to correspond to smaller kinetic energy dissipation and smaller QP scattering angles, leading to p_{red} values closer to 1.

The correlation between p_{red} and the reduced impact parameter b_{red} can be tested using the filtered AMD+GEMINI++ simulations, which, as already shown in Figs. 5.7 and 5.2, are able to well reproduce the characteristics of both the QP remnant and the reconstructed QP in the QPr and QPb channels. Fig. 5.10 shows the correlation between p_{red} and b_{red} for the three beam energies, obtained from filtered AMD+GEMINI++ simulations using the QPr and QPb events. A clear correlation between the two variables is

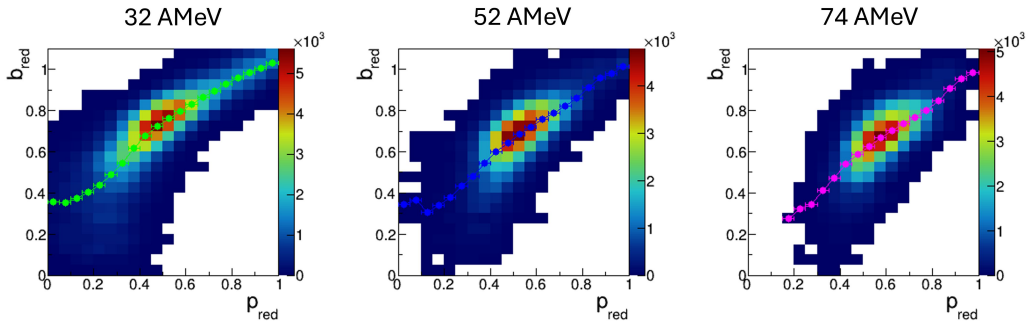

Figure 5.10: Correlation between p_{red} and b_{red} for AMD+GEMINI++ filtered simulations. Solid markers represent the average b_{red} as a function of p_{red}.

observed at all energies, particularly well defined for semiperipheral and pe-

ripheral collisions ($b_{red} > 0.4$). Under this value, the correlation is no more significant. For $b_{red} > 0.4$, the three beam energies show a similar behaviour, while for small impact parameters the distributions become progressively less populated with increasing beam energy. This trend can be understood considering that, for central collisions at 32 AMeV incomplete fusion may be misclassified as a QPr event, while at higher energies multifragmentation dominates and cannot be mistaken for QPr or QPb event. In Fig. 5.10, for each p_{red} the average b_{red} is also plotted with solid markers. To better appreciate the differences in the mean values between the three beam energies, those average b_{red} values as a function of p_{red} are also reported in Fig. 5.11, showing a weak dependence on the incident energy. This minor differences

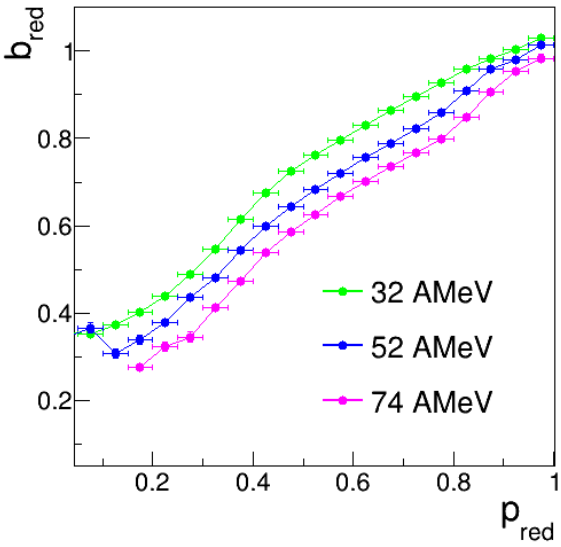

Figure 5.11: Average b_{red} as a function of p_{red} as predicted by AMD+GEMINI++ filtered simulations for the reaction at 32 (green), 52 (blue) and 74 AMeV (magenta).

should be keep in mind in the next chapters, when the analysis of the QP characteristics as a function of the centrality will be discussed. It is also important to verify, according to AMD+GEMINI++ predictions, whether this correlation depends on the reaction channel. Fig. 5.12 compares the average b_{red} as a function of p_{red} for the QPr and QPb channels. The two distributions are very similar, confirming that the $p_{red} - b_{red}$ correlation does not significantly depend on the QP de-excitation mode.

In conclusion, p_{red} can be considered a reliable sorting parameter for semiperipheral and peripheral reactions, both in QPr and QPb channels. It will be extensively used as centrality estimator in the following analysis,

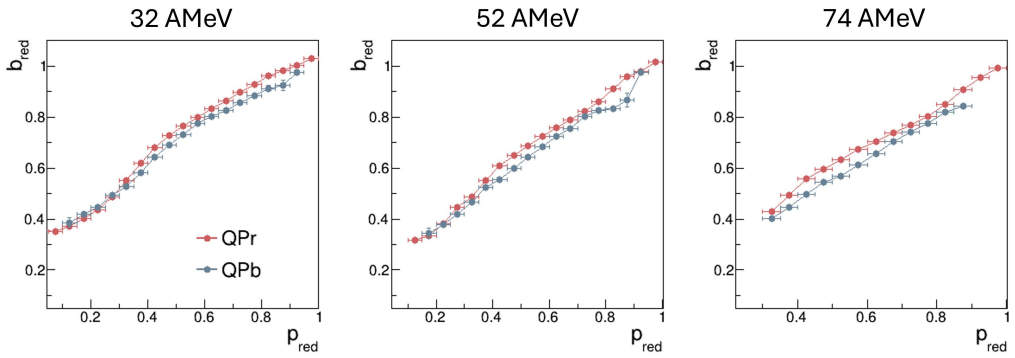

Figure 5.12: Average b_{red} as a function of p_{red} for the QPr (red) and QPb (blue) events as predicted by AMD+GEMINI++ filtered simulations.

focusing on events with $p_{red} > 0.4$.

Chapter 6

Characterization of secondary fragments as a function of centrality

The main aim of this work is to study how the reaction dynamics evolves with centrality and beam energy in both the QPr and QPb channels. As discussed in Chapter 1, extracting information on the primary sources from experiments is particularly challenging. In fact, from an experimental point of view, the secondary fragments are the only observables that can be directly measured. However, these fragments correspond to the final cold residues detected long after their formation and produced at the end of long de-excitation chains, making the connection to the underlying dynamics non-trivial. Nevertheless, the investigation of the detected fragment properties, while being aware of the interplay between dynamical and statistical effects in shaping their characteristics, as a function of centrality, beam energy, and reaction channel, is of interest.

In particular, we will examine the properties of the quasi-projectile (QP), either directly detected as remnant or reconstructed from its breakup fragments, focusing on its size and isospin. Subsequently, we will analyse the light fragments emitted in coincidence with it. After correcting for detection efficiency, these particles are classified according to their emission pattern in order to roughly separate the midvelocity and the evaporative emissions. Special attention is devoted to their isospin properties, with the aim of exploring the manifestation of the isospin drift phenomenon.

Beyond providing preliminary insights into the underlying reaction mechanisms, this study serves as the foundation for the reconstruction of the primary sources, which will be discussed in the next chapter.

6.1 Characteristics of the QP fragments

In Chapter 5, some general characteristics of the QP fragments were presented by means of histograms integrated over all centralities. However, drawing conclusions from these integrated distributions is not straightforward, since they do not account for the different cross sections of the reaction channels as a function of centrality and also because the reaction proceeds differently with centrality. This effect is clearly illustrated in Fig. 6.1, which shows the percentage of QPr (red) and QPb (blue) events with respect to the total number of prelimary selected events as a function of p_{red}. The

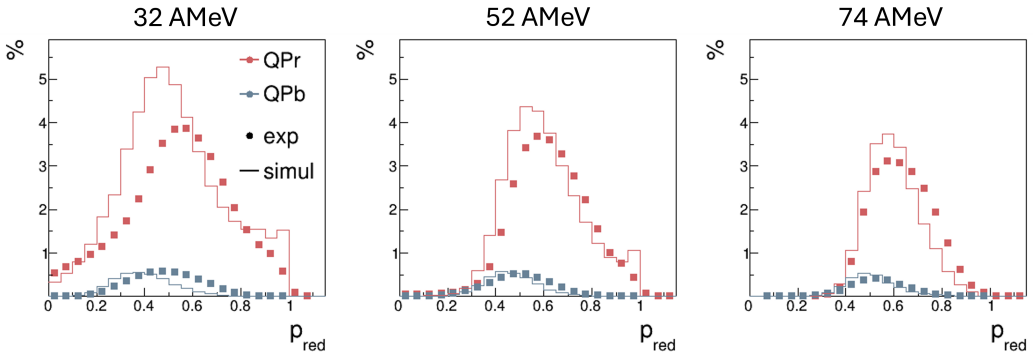

Figure 6.1: Comparison between experimental data (markers) and AMD+GEMINI++ filtered simulations (lines) for the relative cross sections of QPr (red) and QPb (blue) events as a function of p_{red}.

agreement between simulations (solid lines) and experimental data (markers) is not perfect, although it improves with increasing beam energy. This discrepancy is related to the fact that p_{red}, being a normalized momentum, is linked to the QP velocity, which was shown in panel (b) of Fig. 5.2 to be slightly underestimated in the simulations, indicating that the model generates more dissipative events, i.e. more central collisions, compared to the experimental data. Moreover, Fig. 6.1 suggests that the QPr selection pins out more peripheral reactions than the QPb one, producing the observed higher velocities of the QP remnants (panels (b) of Figs. 5.7 and 5.2).

To obtain more detailed information, in the following we will compare the same observables discussed in the previous chapter, together with new ones, as a function of the centrality estimator p_{red}.

6.1.1 QPr channel

In the selection of the QPr channel discussed in Section 5.2 the mass identification of the quasi-projectile is not required. However, since in this section we aim to study isospin observables, this condition must be included. The resulting effects are illustrated in Fig. 6.2, which shows the experimental average charge $\langle Z \rangle$ as a function of p_{red} for all QPr (solid markers) and for those with identified mass (open markers). At 32 and 52 AMeV, the plots are truncated before p_{red}=1, and a clear reduction in the average charge is observed when mass identification is required. This occurs because the heaviest fragments are often not identified in mass: depending on the bombarding energy, the heaviest QP residues can be mainly identified using different methods, with a significant influence in terms of mass-identification capability. At 32 AMeV and 52 AMeV, the Si1-Si2 and Si2-CsI(Tl) correlations are used; the latter, which is predominantly employed at 52 AMeV, spoils the mass resolution. Fortunately, for the 74 AMeV reaction, the use of thicker Si2 detectors (750 μm instead of 500 μm) for the four inner blocks and the introduction of the new Si1+Si2 vs CsI(Tl) correlation enable the mass identification of the QP residue in almost all cases, except for the most peripheral collisions ($p_{red} > 0.9$).

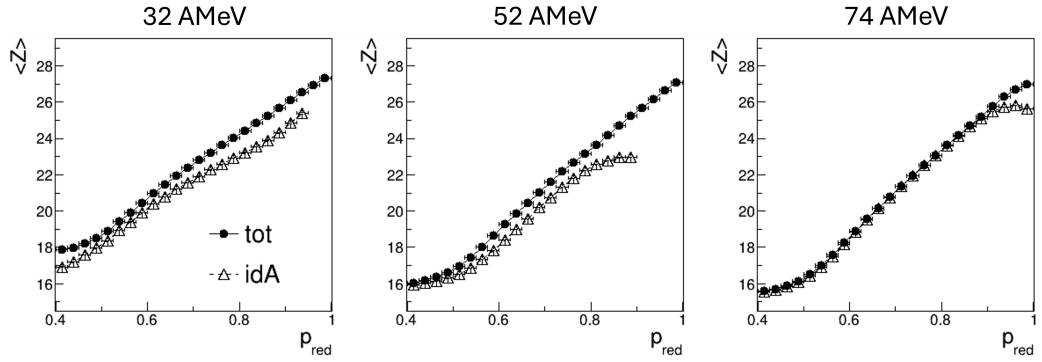

Figure 6.2: Experimental average charge $\langle Z \rangle$ of the QP as a function of p_{red} for QPr events at the three beam energies. Solid markers represent $\langle Z \rangle$ values obtained by considering all detected QP remnant, while open markers correspond to QP with identified mass.

For this reason, in the following analysis, whenever the mass identification of the QPr is required, the results at 32 and 52 AMeV will be presented only up to lower p_{red} values than those considered for the reaction at 74 AMeV. Furthermore, it should be noted that this mass identification requirement may also affect the comparison of the average charge $\langle Z \rangle$ of the QP remnant at the different bombarding energies. This effect can be appreciated

by comparing panels (a) and (b) of Fig. 6.3, which show again the experimental average charge $\langle Z \rangle$ as a function of p_{red}, without (panel (a)) and with (panel (b)) the mass identification requirement, for the three available energies. Fixing p_{red}, the $\langle Z \rangle$ of the QP fragments clearly depends on the

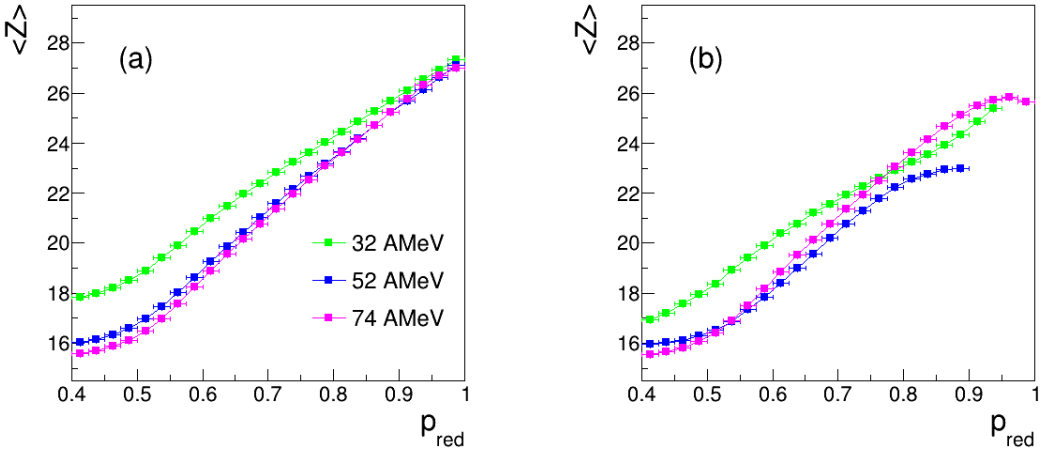

Figure 6.3: Experimental average charge $\langle Z \rangle$ for all the detected QP remnant (panel (a)) and for those identified in mass (panel (b)).

beam energy: at 32 AMeV, the QP fragments are on average larger, while only very small differences are observed between the two highest energies. This trend is evident in panel (a), but the mass identification requirement in panel (b) reduces the gap between 32 and 52 AMeV, up to loose completely this effect for peripheral collisions ($p_{red} > 0.8$), where heaviest QP remnant are produced. Finally, it is worth mentioning that, as discussed in Chapter 5, the slight dependence of the $b_{red} - p_{red}$ correlation on the beam energy could introduce some effects: at the same p_{red} value, a slightly different b_{red} corresponds. Therefore, this effect may reduce the observed differences among the three energies. Nevertheless, the trends of $\langle Z \rangle$ as a function of the centrality presented in Fig. 6.3 appear sufficiently robust to indicate that the behaviour at 32 AMeV differs from that observed higher energies.

To further investigate the characteristics of the QP remnant, its isospin content is analysed. As commonly done in the literature, Fig. 6.4 shows the experimental average neutron to proton ratio $\langle N/Z \rangle$ of the QP remnant, used as isospin-related observable, as a function of p_{red}.

Before discussing these results in detail, it is important to recall that the isospin values are influenced by both the dynamical and statistical stages of the reaction. The initial N/Z of the projectile (1.07) may be modified during the dynamical phase. In this symmetric system, on average, isospin diffusion is absent, and thus only fast emissions and/or other processes like

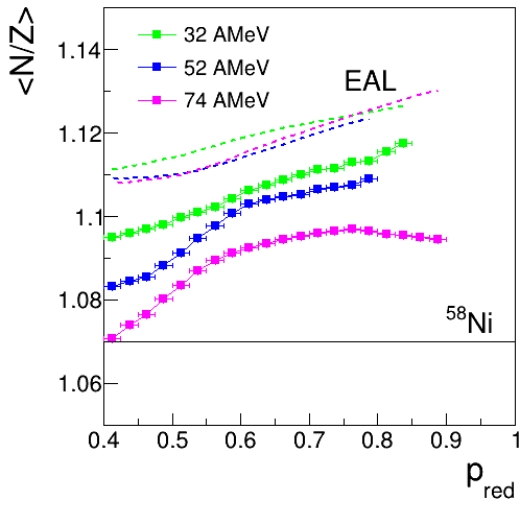

Figure 6.4: Experimental plots of $\langle N/Z \rangle$ vs p_{red} for the QP remnant in the QPr channel selection. The coloured dotted lines represent an estimation of the isospin content assuming that the QP remnant reaches the EAL, while the black line indicates the N/Z of the initial projectile.

isospin drift can alter the N/Z of the primary quasi-projectile. Then, the statistical evaporation of the primary quasi-projectile further modifies its neutron content, driving the system towards the Evaporation Attractor Line [109].

Looking at Fig. 6.4, the $\langle N/Z \rangle$ of the QP remnants is generally slightly larger than that of the projectile (1.07), reflecting the effect of the statistical evaporation that favours daughter nuclei with a larger N/Z with respect to the initial relatively neutron deficient ^{58}Ni isotope. Also the decreasing trend of the isospin content as a function of the centrality (smaller p_{red}), already observed in Refs. [58, 59], can be primarily ascribed to the statistical emission. In fact, the behaviour of $\langle N/Z \rangle$ of the QP remnant reflects the trend of the EAL, shown one for each energy with dotted lines in the corresponding colour. The EAL is calculated according to the parametrization of Ref. [109], assuming the average Z obtained for each p_{red} bin. Concerning the dependence on the bombarding energy, the $\langle N/Z \rangle$ values at 74 MeV are closer to that of the initial projectile, while they progressively deviate toward the EAL as the incident energy decreases. As already pointed out, this behaviour cannot be attributed solely to differences in either the dynamical or statistical phases of the reaction. On one hand, it may reflect a different production of fragments from the neck region. On the other hand, variations in the initial conditions of the excited primary QP* affect its subsequent evaporation pattern, thus also influencing the final isospin of the QP remnant.

6.1.2 QPb channel

As already mentioned in Chapter 5, the mean value of the Z distribution of the reconstructed quasi-projectile in the QPb channel at 74 AMeV can potentially be affected by the requirement $Z \geq 15$ (see panel (a) of Fig. 5.7). Therefore, before presenting mean values, as done for the QPr channel which is less sensitive to this issue, it is necessary, at least in this critical case, to verify whether the charge distribution of the selected events for different centrality bins is representative of the entire charge distribution. In Fig. 6.5, the reconstructed charge distributions for the reaction at 74 AMeV are shown for some p_{red} selections. These distributions show that up to $p_{red} = 0.5$ the

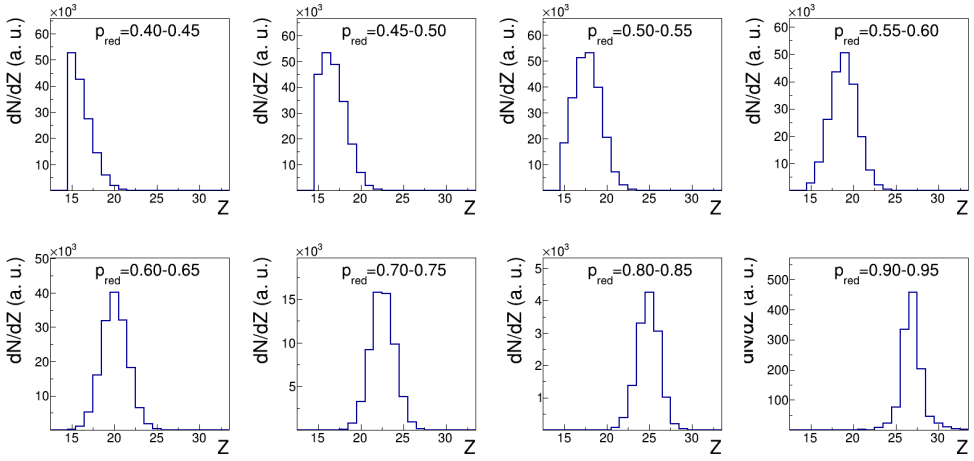

Figure 6.5: Experimental Z distributions of the reconstructed QP in the QPb channel at 74 AMeV for some centrality bins.

distributions are still affected by the $Z \geq 15$ condition, while for $p_{red} \geq 0.5$ the mean values can be reliably determined. Therefore, in the following, all plots will be shown for $p_{red} \geq 0.5$, where the mean values are meaningful.

Fig. 6.6 displays the average number of protons of the reconstructed QP as a function of p_{red}.

In this case, the masses of the two detected fragments are smaller than those measured for the QP remnant and consequently there are no identification limitations. Of course, in this case the mass identification is always required (see Section 5.3) to allow a correct reconstruction of the QP.

As already observed for the QPr channel, a dependence of $\langle Z \rangle$ on the incident energy is evident: the size of the reconstructed QP decreases as the beam energy increases. Their average neutron to proton ratio $\langle N/Z \rangle$ is shown in Fig. 6.7 as a function of p_{red}. The $\langle N/Z \rangle$ values obtained for

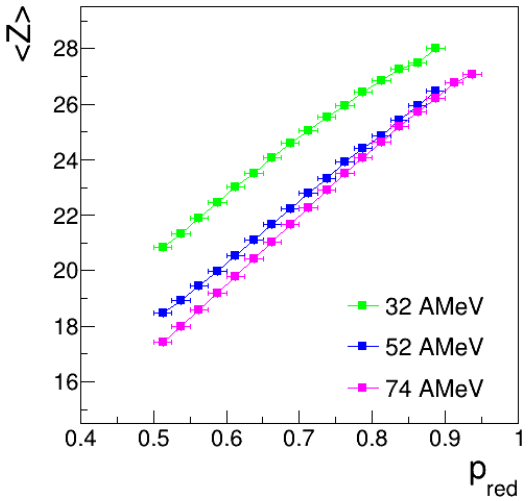

Figure 6.6: Experimental $\langle Z \rangle$ as a function of p_{red} for the reconstructed QP in the QPb channel.

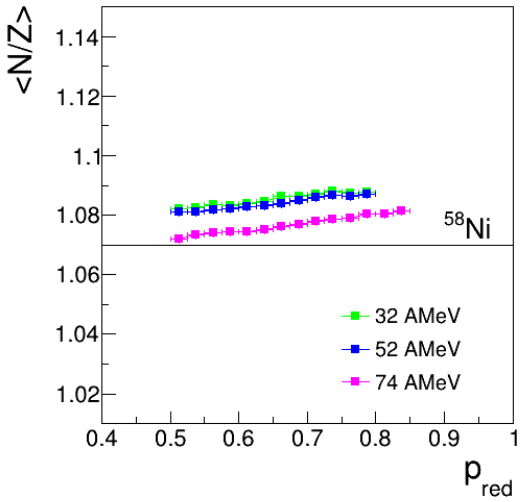

Figure 6.7: Experimental plots of $\langle N/Z \rangle$ vs p_{red} for the reconstructed QP in the QPb channel selection. The black line indicates the N/Z of the initial projectile.

this channel are generally closer to the initial projectile ratio (1.07) and less dependent on the centrality. Regarding the incident energy dependence, as already observed for the QPr channel, the $\langle N/Z \rangle$ values at higher energies remain closer to 1.07. In this case, even at 32 and 52 AMeV the values stay near the initial ratio, and the difference between these two energies is very small.

6.1.3 Comparison between QPr and QPb channels

After the separate discussion of the QPr and QPb channels, it is now time to make a direct comparison, as proposed in Fig. 6.8, in order to better highlight their similarities and differences. In these panels, both the experimental data (solid markers) and the AMD+GEMINI++ simulation results (open markers) are presented. The upper panels display the average charge $\langle Z \rangle$ of

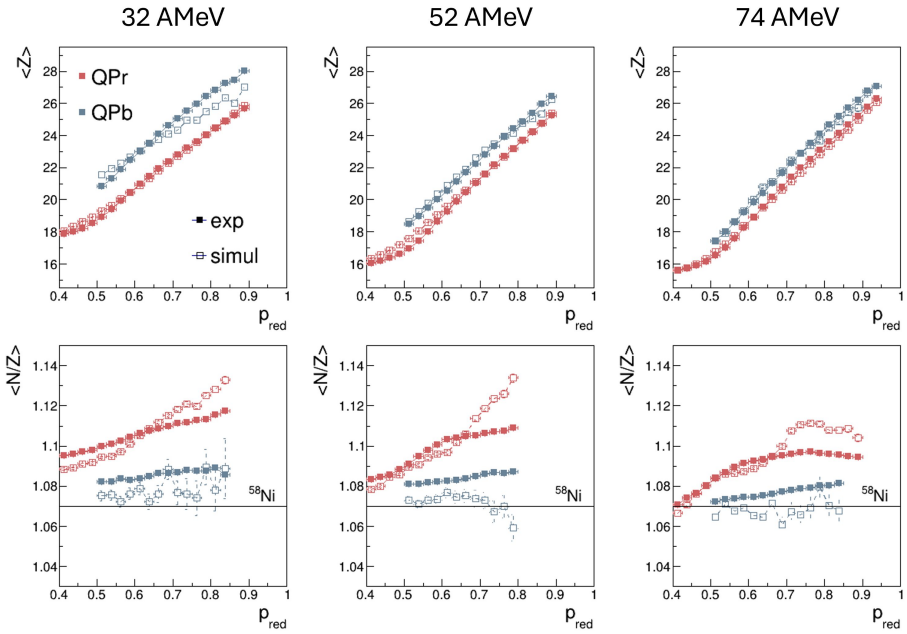

Figure 6.8: Experimental (solid markers) and simulated (open markers) $\langle Z \rangle$ (upper row) and $\langle N/Z \rangle$ (lower row) as a function of the centrality estimator p_{red} for QPr (red) and QPb (blue) event selections.

the QP remnant (red) or reconstructed (blue), while the lower row shows their average neutron to proton ratio $\langle N/Z \rangle$, both as a function of the centrality estimator p_{red}.

Concerning the comparison between experimental data and AMD+GEMINI++ simulations, the overall agreement in reproducing $\langle Z \rangle$ (and $\langle N \rangle$) is satisfac-

tory for both channels, although some discrepancies are observed particularly in the QPb channel at 32 AMeV. Nevertheless, they fail to reproduce the detailed behaviour of the $\langle N/Z \rangle$ as a function of p_{red}, indicating that, despite comparable mean values, they exhibit different isotopic distributions, mainly in the tails. The fail to quantitatively reproduce the experimental $\langle N/Z \rangle$ values has already been reported in Ref. [33].

Moving to the comparison between different selected channels, $\langle Z \rangle$ is larger in the QPb channel, suggesting a larger average size. This difference decreases with increasing energy. Moreover, the comparison of the average neutron to proton ratio $\langle N/Z \rangle$ reveals a clear distinction: the reconstructed QP in the QPb channel is always less neutron rich than the QP remnant of the QPr channel, regardless beam energy and centrality, although the magnitude of this difference decreases for more central collisions.

The origin of these differences observed in both size and isospin between the two channels is not straightforward to interpret, as they could be related to both a different dynamical phase and/or a different statistical de-excitation process. In fact, a different dynamical phase could occur before the breakup or not of the primary quasi-projectile, leading to different conditions for the subsequent de-excitation. Moreover, for the QPb breakup channel the source of evaporation process is less defined: evaporation may take place before or after the breakup. However, if the breakup has a dynamical origin, it is expected to develop on a very short timescale, so that any subsequent evaporation would proceed from the breakup fragments themselves (if still excited). It is worth also noting that the breakup requires energy, which is subtracted from the available internal excitation. Consequently, in the QPb channel, the evaporation may act on sources that differs from the QP remnant. The combination of possible different size and excitation energy in the QPb channel can impact the evaporation process, which could have less "room" to drive the system towards the EAL, which in case of lighter fragments itself lies at lower N/Z. These effects could also explain the larger size of the reconstructed QP compared to the QP remnant.

6.2 Light particles in coincidence with the QP

In this section the characteristics of the light fragments (Z<5) emitted in coincidence with the QP remnant or with the reconstructed QP are analysed. These particles carry rich information about the collision, as they can be produced from the evaporation of the QP (and QT) or from dynamical

processes.

As discussed in Section 5.2, our analysis focuses on the QP phase space. Therefore, in each event, only light particles with $v_{\parallel}^{cm} > 0$ are selected, where $v_{\parallel}^{cm}$ is the component of velocity, in the cm frame, along the asymptotic QP-QT separation axis (see Fig. 5.3).

As already illustrated in Fig. 1.2, particles evaporated by the QP typically exhibit a rather symmetric forward-backward distribution in the QP reference frame, whereas those produced by dynamical processes populate the velocity region intermediate between the QP and QT. Consequently, their study is often performed according to their emission pattern [37, 39, 40, 55].

In this section, we investigate the isospin characteristics of these light particles. To strongly suppress any effect related to the experimental setup, the data are corrected for the geometrical acceptance and for the low-energy identification thresholds. Moreover, the experimental proton yields are corrected for the Incomplete Energy Deposition effects in the FAZIA CsI detectors (see Appendix B for details). These corrections will play an even more important role in the next chapter, where a detailed separation of the evaporative and midvelocity components and the full reconstruction of the sources through an average nuclear calorimetry procedure will be performed.

6.2.1 Efficiency correction

For the following analysis, it is necessary to correct the yields of light particles detected in the QPr and QPb channels and emitted forward in the centre of mass reference frame, accounting for the limited geometrical coverage of the setup and the low-energy identification thresholds. As previously mentioned, the efficiency correction is obtained using AMD+GEMINI++ simulations for all three beam energies.

Average correction factors for light particles are estimated for each bin of p_{red} and for each cell in the ($v_{\parallel}$, $v_{\perp}$) space by comparing the yields from the 4π and the filtered simulations for a given channel (QPr or QPb). For particles with $Z = 1$, the statistics is sufficient to allow the estimation of separate correction factors for each isotope, while for particles with $Z > 1$ correction factors are estimated for each element. It is worth mentioning that only particles identified both in charge and mass are considered for the efficiency estimation and in the subsequent analysis. As an example, Fig. 6.9 shows the experimental bidimensional velocity correlations ($v_{\parallel}$,$v_{\perp}$) in the QP frame for protons, selected with the condition $v_{\parallel}^{cm} > 0$, at the 32 (left) and 74 (right) AMeV for the centrality bin $p_{red} = 0.6 - 0.7$. One clearly observes the typical Coulomb ring, corresponding to the emission from a hot source

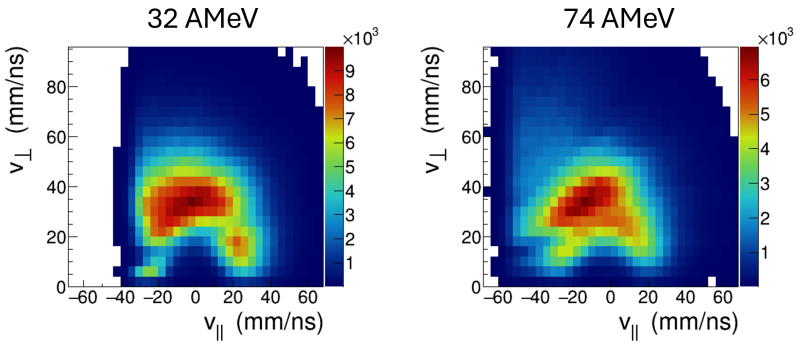

Figure 6.9: Experimental correlation $v_{\parallel}$ vs $v_{\perp}$ for protons in the centrality bin p_{red}=0.6-0.7 in the QPr channel.

located around $v_{\parallel} = 0$. However, the rings appear incomplete, showing regions of reduced efficiency whose position varies with the beam energy due to different kinematics. After applying the efficiency correction, the same correlations become much more uniform, as shown in Fig. 6.10. Here, the

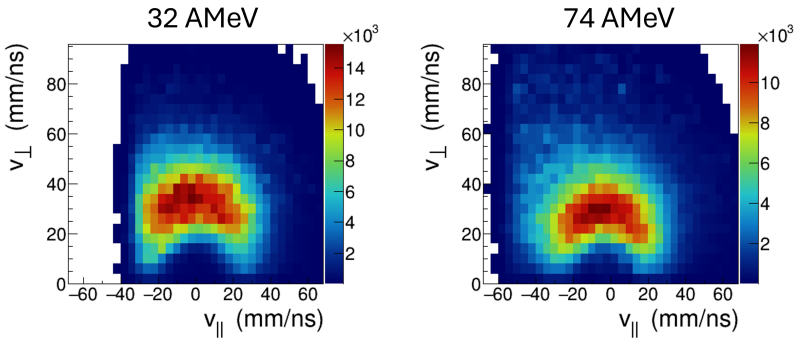

Figure 6.10: Experimental correlation $v_{\parallel}$ vs $v_{\perp}$ for protons in the centrality bin p_{red}=0.6-0.7 in the QPr channel corrected using the efficiency factors estimated with AMD+GEMINI++ simulations.

distortions related to the apparatus disappear and the distributions become homogeneous around the QP position. Similar corrections are made for all the particle species. The same procedure is consistently applied to both experimental data and filtered simulations.

The quality of this efficiency correction will be tested in Section 7.1, where, by exploiting the symmetry of the studied system, the charges of the forward-emitted light particles are added to the quasi-projectile charge to reproduce, on average, that of the initial projectile.

In principle, the estimated detection efficiency and the corresponding correction should be independent of the simulation model used. However, the response function of a multidetector under specific event selections, such as those adopted here, is a complex function of many parameters. As a result, systematic effects and distortions may be introduced when different event generators are used. Therefore, to strengthen the reliability of our procedure, the HIPSE simulation has been employed as a test in the case of 74 AMeV. Fig. 6.11 shows the average multiplicities of different light particles as a function of p_{red} for the 74 AMeV reaction after applying the efficiency correction. Solid markers correspond to corrections derived from AMD+GEMINI++ simulations, while open markers correspond to those obtained using HIPSE. The average multiplicities obtained with the two different efficiency correc-

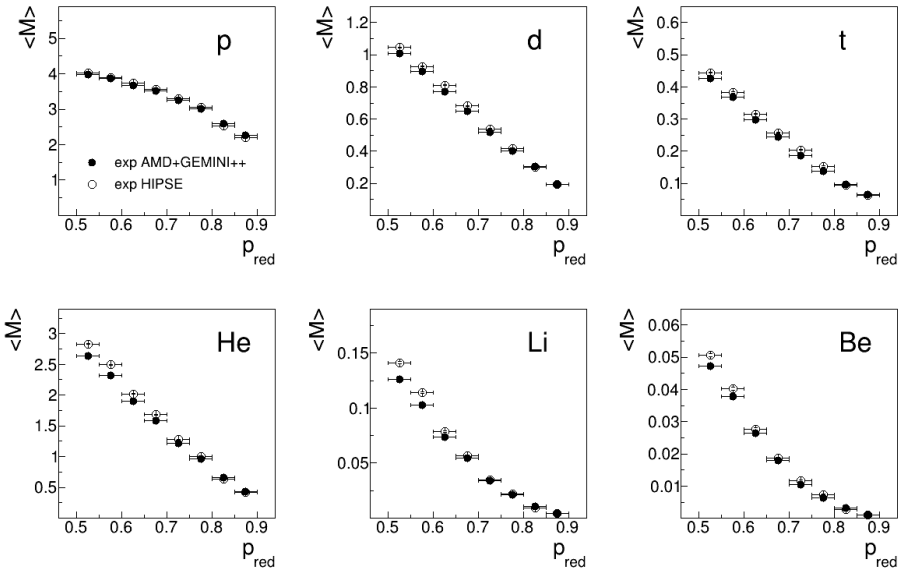

Figure 6.11: Experimental average multiplicities for the 74 AMeV reaction as a function of p_{red} for different light particles corrected for the detection efficiency using AMD+GEMINI++ (solid markers) and HIPSE (open markers) simulations.

tions show similar trends and values, but not always compatible within statistical uncertainties. The differences depend on both the particle species and the centrality, and they can reach up to 10%. However, the largest systematic effects are associated with the less abundant particles. The impact of using different models on the final results will be further discussed in the next chapter.

In the following, unless stated otherwise, all results are presented using efficiency corrections derived from AMD+GEMINI++ simulations.

6.2.2 Isospin characteristics of light particles

In this section, the isospin content of light fragments emitted forward in the centre of mass (i.e. with $v_{\parallel}^{cm} > 0$) will be analysed. In general, it reflects that of the emitting source and is generally studied comparing those of the particles emitted forward ($v_{\parallel} > 0$) and backward ($v_{\parallel} < 0$) in the QP frame [37, 39, 40]. In fact, the particles emitted forward with respect to the QP can be considered mostly related to the evaporative emissions of the excited QP. Instead, the particles emitted backward can be a mixture of midvelocity emission and QP decay. The relative contribution of the two emission components varies as a function of several parameters, the most relevant being the particle type, the beam energy, and the impact parameter. Since the evaporative emission is forward-backward symmetric, any difference between these two components can be attributed to the midvelocity emissions. A variety of isospin-sensitive observables have been proposed in the literature to characterize light-particle emissions [2, 5, 8, 17, 37–40]. In this work, we adopt the isospin ratio of complex particles [8, 19, 41, 59].

Isospin ratio of complex particles

An observable sensitive to the isospin of light particles is the isospin ratio for complex particles, proposed in [8]. In Ref. [8], the isospin ratio, for each centrality bin, is averaged on all complex emitted particles being defined as:

$$\langle N \rangle / \langle Z \rangle_{CP} = \frac{\sum_i \sum_\nu N_\nu^i}{\sum_i \sum_\nu Z_\nu^i} \tag{6.1}$$

where the outer sum runs over all the events in the selected p_{red} bin, and the inner sum runs over all complex particles in the i-th event. N_ν^i and Z_ν^i are the numbers of neutrons and protons bound in the particle ν. The considered complex particles are d, t, ^{3}He, ^{4}He, ^{6}He, ^{6}Li, ^{7}Li, ^{8}Li, ^{9}Li, ^{7}Be, ^{9}Be, ^{10}Be. Free protons are excluded as well as free neutrons which are not detected. The $\langle N \rangle / \langle Z \rangle_{CP}$ can be evaluated separately for complex particles emitted forward or backward with respect to the QP.

Fig. 6.12 shows the experimental $\langle N \rangle / \langle Z \rangle_{CP}$ as a function of p_{red} for the QPr (panel (a)) and QPb (panel (b)) channels. Forward-emitted particles (full markers) are systematically more neutron-poor than the backward-emitted ones (open markers) at all beam energies. As already pointed out, this behaviour is consistent with their origin: forward particles mostly reflect

the evaporative decay of the excited QP, while backward ones include contributions from both evaporation and midvelocity emissions, which is expected to be more neutron-rich. Moreover, a smooth increase in the neutron content

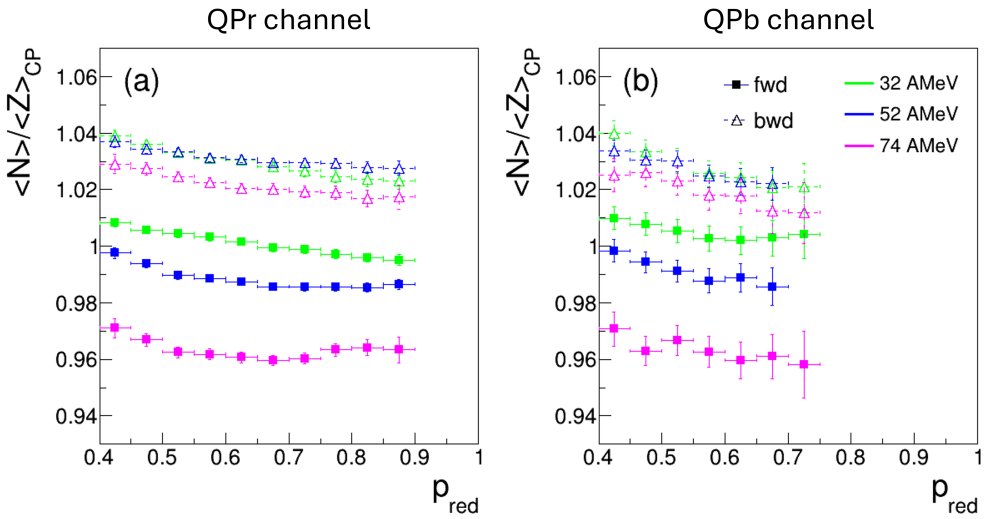

Figure 6.12: Experimental $\langle N\rangle/\langle Z\rangle_{CP}$ of complex particles forward (full square markers) and backward (open triangle markers) emitted with respect to the quasi-projectile as a function of p_{red} for the QPr (panel (a)) and QPb (panel(b)) channels.

with centrality is observed for both the forward and backward components. Concerning the dependence on the bombarding energy, a clear trend emerges for the forward-emitted component: the neutron content of evaporated complex particles decreases as the beam energy increases. It is worth noting that a similar behaviour of $\langle N/Z\rangle$ as a function of beam energy was already observed in Fig. 6.4, where the isospin of the QP remnant was analysed, and, although less pronounced, in Fig. 6.7, which shows the reconstructed QP isospin. However, a detailed interpretation of these effects at this stage of the analysis is challenging. A qualitative attempt to disentangle statistical and dynamical contributions will be addressed in Chapter 7.

To better illustrate the similarities, between QPr and QPb channels, Fig. 6.13 compares their $\langle N\rangle/\langle Z\rangle_{CP}$ directly for the three incident energies. Within the statistical uncertainties, the results obtained for the QPr and QPb channels are fully consistent. This agreement suggests that, on average, both evaporative and midvelocity clusters exhibit very similar isotopic properties in the two channels, at least for the complex particles. However, as shown in the lower panels of Fig. 6.8, a systematic difference in the isospin content of the detected or reconstructed QP is observed. It is worth noting

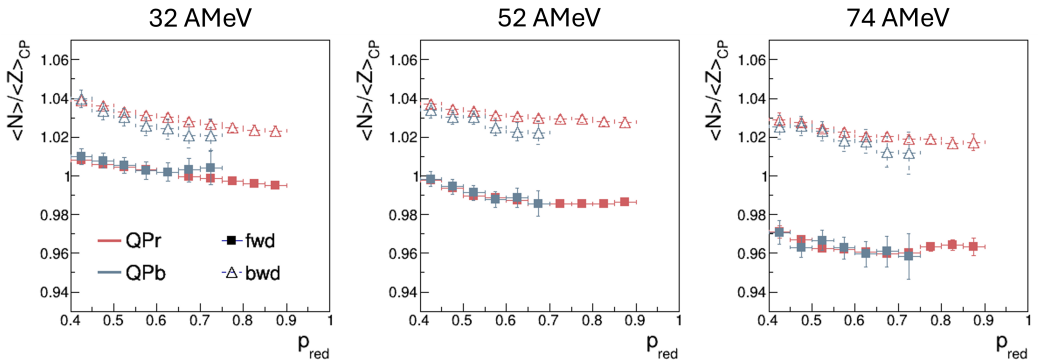

Figure 6.13: Experimental $\langle N\rangle/\langle Z\rangle_{CP}$ of the complex particles forward (full square markers) and backward (open triangle markers) emitted with respect to the quasi-projectile as a function of p_{red} for the QPr (red) and QPb (blue) channels.

that even a difference of one or two nucleons is sufficient to account for the observed $\langle N/Z\rangle$ spread. Considering that Fig. 6.13 includes only bound nucleons, it is reasonable to infer the presence of a small residual difference in the emission of free nucleons between the two channels.

Summarizing, despite the complexity of the reaction mechanisms, some observations can be made. There is a clear indication, as expected and as reported by previous literature, that the backward emitted component in the QP frame exhibit a larger neutron content compared to the forward one. It is therefore plausible that this backward emission is influenced by fast processes occurring before the end of the interaction (the model suggests before 100-150fm/c) from a dilute region where the isospin drift may act to slightly enrich the matter of neutrons. This experimental evidence is consistently observed in both the QPr and QPb channels. Focusing on the dependence on incident energy, the remnant and reconstructed QP and their corresponding forward-emitted light clusters become progressively less neutron-rich as the beam energy increases. This trend suggests that the primary QP* may vary with the beam energy as a consequence of a modified dynamical phase preceding de-excitation. Such a difference in the initial conditions would affect the subsequent statistical decay process. Concerning the comparison between the QPr and QPb channels, the average isospin ratio of the complex particles turns out to be very similar in the two cases. However, since the reconstructed QP channel is systematically less neutron rich than the QP remnant, a small difference must exist in the emission of free nucleons (one or two nucleons of difference are enough to justify the experimental evidence). The differences observed, both in the isospin and in the size of the

quasi-projectile, could be related to a distinct dynamical phase occurring before the breakup, which, whether of dynamical origin, is expected to develop on a short timescale. In this case, the subsequent statistical de-excitation process would also differ, since in the breakup channel part of the excitation energy is consumed by the breakup itself, and the evaporation sources may correspond to the breakup fragments rather than to the original QP residue.

In the next chapter, further insight will be explored through a calorimetric reconstruction of the sources, with an accurate separation of the evaporative and the midvelocity components.

Chapter 7

Primary source reconstruction

In the previous chapter, the directly measured QP remnant and reconstructed and the light fragments emitted in coincidence with them have been investigated in terms of size and isospin content, obtaining a qualitative prove of the isospin drift and some general trends as a function of the bombarding energy to be better understood.

The purpose of this chapter is the quantitative disentanglement of the evaporative and midvelocity emission, in order to attempt the reconstruction in term of size and of excitation energy, through the widely used nuclear calorimetric method [3, 63, 118–120], of the primary QP* and the neck sources in both QPr and QPb channel. It is important to note that this method provides an average calorimetric description rather than a full event-by-event reconstruction, allowing us to extract the global characteristics of the primary nuclear sources.

As shown in Chapter 6, the requirement of isotopic identification of the QP remnant can introduce systematic biases when comparing results at different beam energies and for different reaction channels. For this reason, in the present analysis this condition has been relaxed, since the isotopic composition of the QP is not of interest. Relaxing this constraint inevitably introduces some uncertainty in the average neutron number associated with the QPr, since for fragments identified only in charge, the mass is assigned according to the EAL formula. Nevertheless, simulations indicate that the resulting average neutron number does not differ significantly (within the uncertainties) from that obtained when the mass is measured. Conversely, for light species, identification in both charge and mass is always required, as it is essential for the subsequent isospin analysis.

It is worth noting that, for the first time, this procedure is also applied to the fragments detected in the QPb channel, where the situation is more complex because the emitting source of the evaporated particles is not fully

defined. Specific assumptions are therefore introduced, and the results are discussed accordingly.

The chapter is organized as follows: the first sections describes the adopted procedure; then, the results obtained for both experimental and filtered simulated data are presented and discussed. After the complete disentanglement of the evaporative and midvelocity emissions, the isospin analysis is proposed.

7.1 Reconstruction of the initial projectile

The first step in reconstructing the different sources in the QPr and QPb channels is to verify whether, by combining the remnant or the reconstructed QP (hereafter generically referred to as QP in the formulas) with the light fragments emitted in coincidence and attributable to the QP phase-space, it is possible to recover the characteristics of the initial ^{58}Ni projectile in terms of mass, charge, and kinetic energy. This step is crucial for validating the efficiency correction and for evaluating the emission of free neutrons, and therefore must be performed before proceeding with the analysis.

Since this analysis is performed for event classes defined according to centrality, we refer primarily to average quantities. Hereafter, the brackets $\langle\rangle$ indicate average values over the events within a given centrality bin.

As in the previous chapter, only light fragments (Z<5) identified in charge and mass and assigned to the QP phase-space (those with $v_{//}^{cm} > 0$, as shown in Fig. 5.3) are considered. The average yields of these particles, corrected on average to account for the inefficiencies of the detection setup, including the IED effect of FAZIA CsI for the experimental data, are labelled as M_{C_i}. Due to the symmetry of the system, any possible target contribution in the forward hemisphere can be considered balanced by the loss of projectile particles in the backward hemisphere.

The total charge (in the forward hemisphere) can be estimated as

$$\langle Z_{tot} \rangle = \langle Z_{QP} \rangle + \sum_i Z_{C_i} \langle M_{C_i} \rangle \tag{7.1}$$

where Z_{QP} is the average charge of the QP remnant or reconstructed and Z_{C_i} are the atomic numbers of the charged particles of the i-th species, with the sum extending over all light isotopes (Z<5). In Fig. 7.1, the $\langle Z_{QP} \rangle$ is shown as a function of p_{red} with red square markers, while the $\langle Z_{tot} \rangle$, after the reconstruction process, is drawn with blue circle markers. In both cases, the experimental data are shown with solid markers, while the AMD+GEMINI++ filtered simulations are shown with open ones. Finally, the black line in each panel represent the initial charge of the projectile $Z_{proj} = 28$, which is the

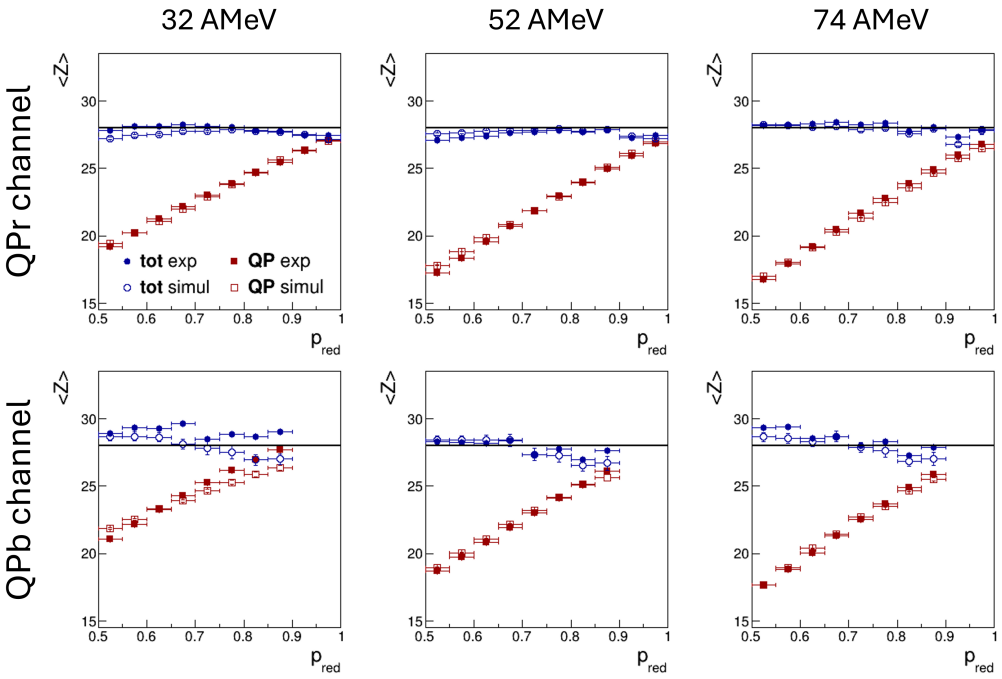

Figure 7.1: The $\langle Z_{QP} \rangle$ (red squares) and the average total charge forward emitted in the cm $\langle Z_{tot} \rangle$ (blue circles) as a function of p_{red} for the QPr (upper panels) and the QPb (lower panels) channels. Solid markers: experimental data. Open markers: AMD+GEMINI++ filtered simulations.

expected value for $\langle Z_{tot} \rangle$. For the QPr channel (upper row), for all centrality bins and incident energies, the projectile charge is well reproduced, within about one charge unit. The rapidly widening gap between $\langle Z_{QP} \rangle$ and $\langle Z_{tot} \rangle$ visually indicates the increasing amount of charge emitted with increasing centrality. Similar results are obtained for the QPb channel (lower row), although in this case the projectile charge reconstruction is reproduced within two charge units.

Analogously to the atomic number, the total average number of neutrons can be estimated as

$$\langle N_{tot} \rangle = \langle N_{QP} \rangle + \sum_i N_{C_i} \langle M_{C_i} \rangle \tag{7.2}$$

where N_{QP} is the average number of neutrons of the QP remnant or reconstructed (displayed with red square markers in Fig. 7.2) and N_{C_i} is the neutron number of a given charged particle species. It is evident from Fig. 7.2 that $\langle N_{tot} \rangle$, for both the QPr (upper row) and QPb (lower row) channels, is systematically lower than $N_{proj} = 30$ (black line), with the discrepancy

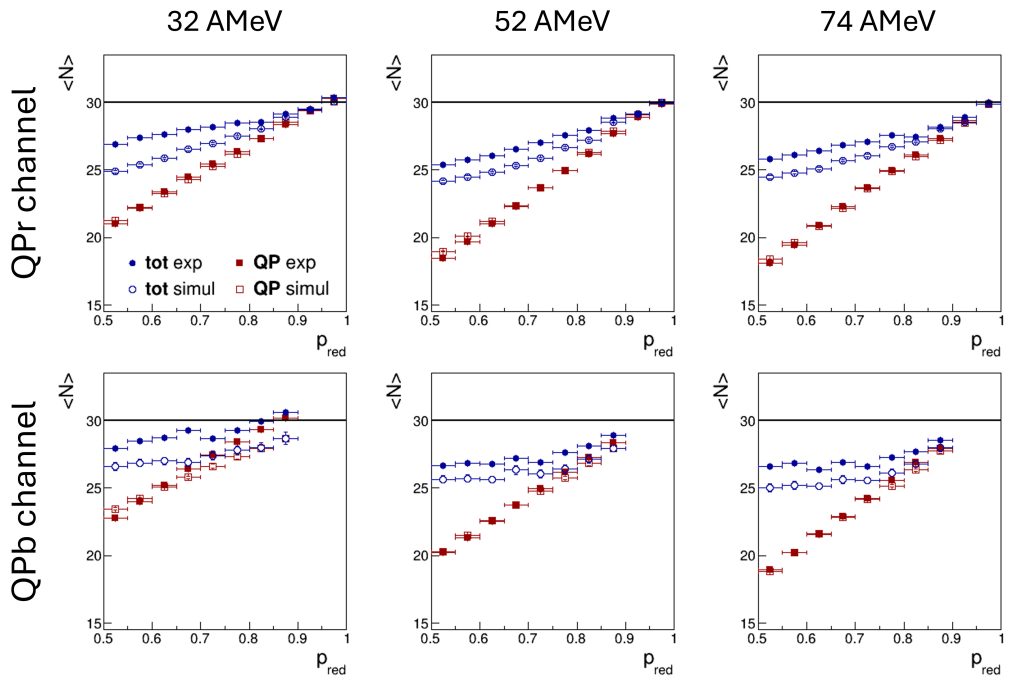

Figure 7.2: The $\langle N_{QP} \rangle$ (red squares) and the average total number of neutron forward emitted in the cm $\langle N_{tot} \rangle$ (blue circles) as a function of p_{red} for the QPr (upper panels) and the QPb (lower panels) channels. Solid markers: experimental data. Open markers: AMD+GEMINI++ filtered simulations.

depending on centrality and incident energy. This happens because free neutrons are not detected, preventing the recovery of the initial projectile neutron number. However, assuming N_{proj} as the reference neutron content, the contribution of free neutrons can be estimated from the conservation law as

$$\langle M_n \rangle = N_{proj} - \langle N_{tot} \rangle \tag{7.3}$$

with $\langle N_{tot} \rangle$ defined as in Eq. 7.2.

The different gaps between $\langle N_{tot} \rangle$ and $\langle N_{QP} \rangle$ observed in experimental and simulated data lead to different estimates of the average free-neutron multiplicities. In particular, the simulations tend to systematically overpredict free-neutron emission, consistent with the excess of free nucleons at the expense of light clusters in AMD+GEMINI++ simulations already observed in previous studies [102, 107]. This behaviour is further supported by the plots of Fig. 7.3, which displays, as representative examples, the average multiplicities of charged particles as function of p_{red} in the QPr channel at 74 AMeV. The average multiplicities of p,d and t are shown separately, while those of clusters with $Z > 1$ are shown without distinguishing

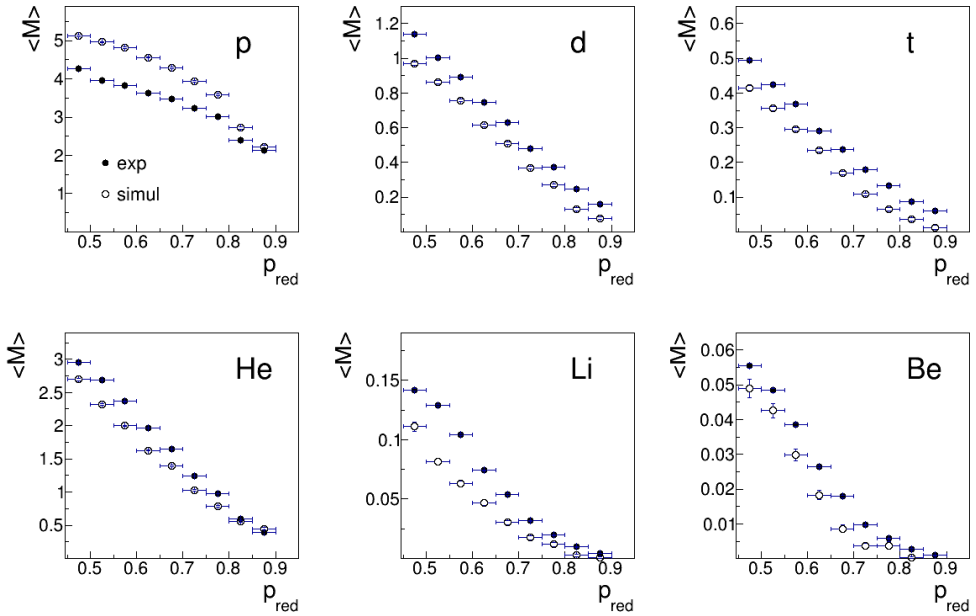

Figure 7.3: Average multiplicities $\langle M \rangle$ of light particles (p, d, t, He, Li and Be) in the QPr channel for the reaction at 74 AMeV. The solid markers represent the experimental data, while the open markers the AMD+GEMINI++ filtered simulation. Solid markers: experimental data. Open markers: AMD+GEMINI++ filtered simulations.

by isotope, although their mass are always measured. The comparison between experiment (solid markers) and simulation (open markers) shows that AMD+GEMINI++ overestimates proton yields while underestimating cluster production (from d to Be). This discrepancy, consistently observed at all studied energies and for both QPr and QPb channels, reflects a general limitation of reaction models that struggle to give correct predictions on cluster production [102, 121, 122].

Using the same principle applied to the proton and neutron content, the total kinetic energy of initial projectile can be obtained as the sum of the cm kinetic energy of the QP and the energy associated to the emission of all forward-going particles:

$$\langle E \rangle = \langle E^{cm}_{QP} \rangle + \langle E^{cm}_{particles} \rangle \tag{7.4}$$

$$\langle E^{cm}_{particles} \rangle = \sum_i \langle k^{cm}_{C_i} \rangle \langle M_{C_i} \rangle + \langle k^{cm}_n \rangle \langle M_n \rangle - Q_{tot} \tag{7.5}$$

where $\langle k^{cm}_{C_i} \rangle$ is the average kinetic energy in the cm of the different charged particle, $\langle k^{cm}_n \rangle$ is the average kinetic energy of the free neutrons (estimated

from that of protons after subtracting the Coulomb barrier), and Q_{tot} is the Q-value for separating the projectile into the average QP remnant or the average breakup fragments and as many neutrons and charged particles as given by their multiplicities. It should be emphasized that, when evaluating the product of two mean quantities, the covariance term should also be taken into account. In the present case, this term was found to be negligible. In this way, the reconstructed energy should approach the projectile cm kinetic energy, having neglected only the possible contribution of gamma rays (mostly emitted at the end of the evaporation chain). The results are presented in Fig. 7.4 for the QPr and QPb channel. Also in this case, the kinetic

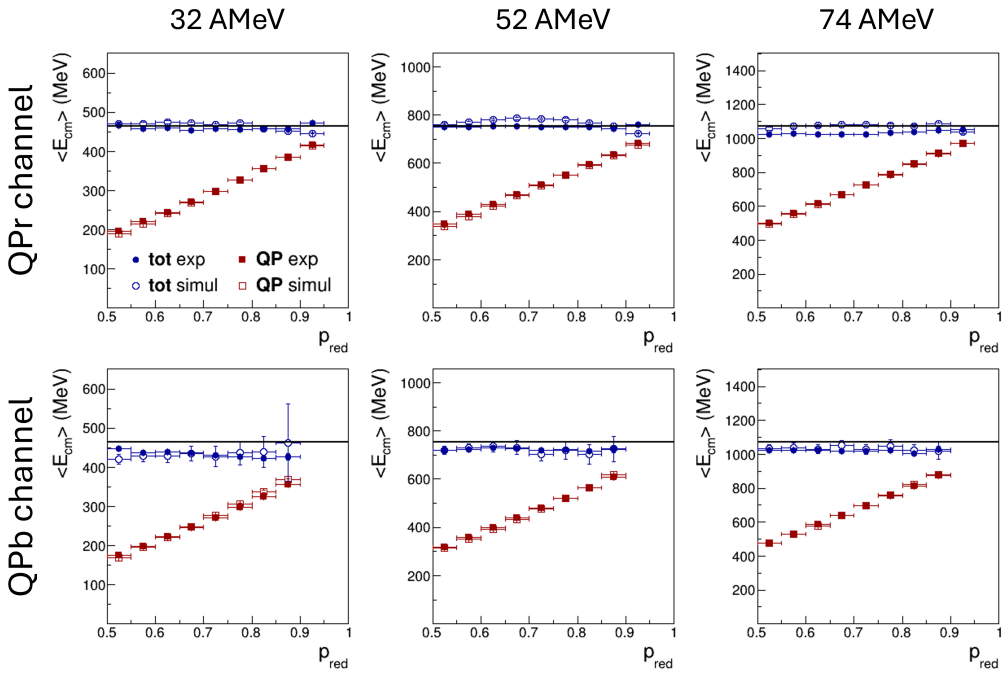

Figure 7.4: The $\langle E_{QP}^{cm} \rangle$ (red squares) and the average total kinetic energy of all fragments forward emitted in the cm $\langle E_{tot}^{cm} \rangle$ (blue circles) as a function of p_{red} for the QPr (upper panels) and the QPb (lower panels) channels. Solid markers: experimental data. Open markers: AMD+GEMINI++ filtered simulations.

energy of the QP is shown with red square markers, while the reconstructed total energy is shown with blue circle markers (solid for experimental data and open for simulations). For the QPr channel (upper panels) the energy balance is globally satisfying, with a deviation within 4% for the simulation at 52 AMeV and a systematic lower final value for the experimental values at 74 AMeV within 5%. This experimental trend at 74 AMeV is observed in-

dependently of whether efficiency corrections are performed, the "standard" one using AMD+GEMINI++ or that one using HIPSE. For the QPb channel a clear behaviour is evident for all the three beam energies both for simulated and experimental data: the reconstructed energies are systematically lower for all energies of about 5%. These discrepancies exceed the statistical uncertainties shown. Nevertheless, possible systematic errors should be taken into account, such as those arising from the evaluation of the neutron multiplicity, which can be slightly different from the estimated one.

7.2 Pre-equilibrium contribution

Another preliminary step before disentangling the midvelocity and evaporative components it to verify whether a contribution from pre-equilibrium emission is present.

As discussed in Chapter 1, pre-equilibrium emission mainly affects free nucleons and depends on both the beam energy and the collision centrality. When present, this component can be identified through the analysis of kinetic energy spectra of emitted particles.

Fig. 7.5 displays the proton kinetic energy spectra in the QP reference frame for forward angles ($10° < \theta < 20°$), where the midvelocity contribution is expected to be negligible. In the case of a pure evaporation process, the kinetic energy spectra are expected to follow a surface Maxwellian distribution:

$$\frac{dN}{dE}(E) = N\frac{(E-B)}{T^2}e^{-\frac{E-B}{T}} \tag{7.6}$$

where N, B, and T are the normalization factor, the Coulomb barrier, and the apparent temperature of the equilibrated source, respectively. However, the Maxwellian fits (red lines) do not fully reproduce the experimental spectra: a harder, high-energy component is clearly visible, consistent with a pre-equilibrium contribution. The intensity of this component decreases for more peripheral and less energetic collisions and scales correctly with the bombarding energy, further supporting its identification as pre-equilibrium emission.

Moreover, this component is observed only for protons, while it is absent for clusters, as illustrated in Fig. 7.6 where the kinetic energy spectra of α particles for the centrality bin $p_{red} = 0.5 - 0.55$ are shown. In this case, the Maxwellian function provides an excellent description of the data, with no indication of a high-energy tail. The temperatures extracted from the Maxwellian fits, indicated in the panels, can be interpreted as the apparent temperature of the equilibrated QP* source. These temperatures decrease

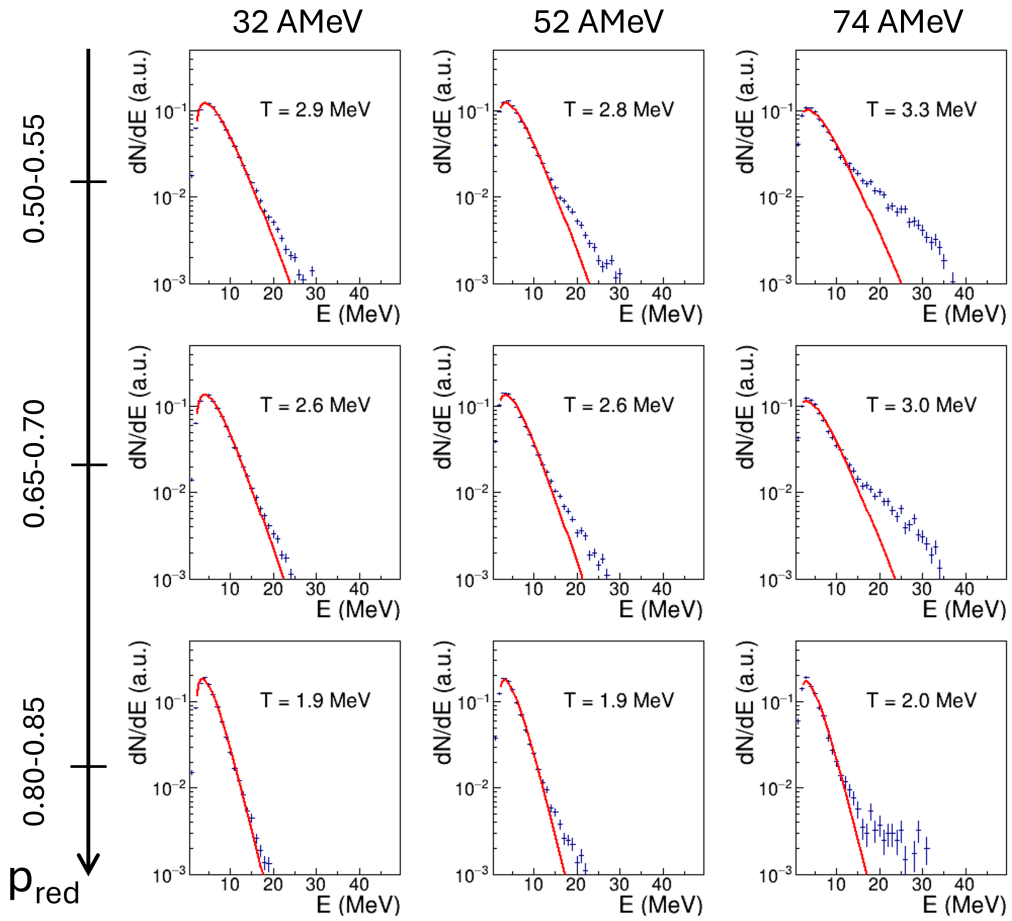

Figure 7.5: Experimental proton kinetic energy spectra in the QP reference frame for $10° < \theta < 20°$ for different centrality bins. The histograms are normalized to unit area. The red lines represent Maxwellian fits.

with increasing centrality and are almost independent of the beam energy. The comparison between proton and α temperatures at the same centrality, as already observed in Ref. [123], reveals systematic differences, possibly indicating that these species are emitted at different stages of the evaporation chain. Moreover, a systematic uncertainty of at least 10% should be considered, as carefully estimated in Ref. [119].

Concerning the AMD+GEMINI++ simulations, the proton spectra are shown in Fig. 7.7 for the centrality bin $p_{red} = 0.5 - 0.55$. In this case, the Maxwellian fits adequately reproduce the simulated spectra, showing no evidence of a high-energy tail. Moreover, the extracted temperatures of the QP* source are slightly higher than the experimental ones.

Despite the evidence of a pre-equilibrium contribution in the experimental

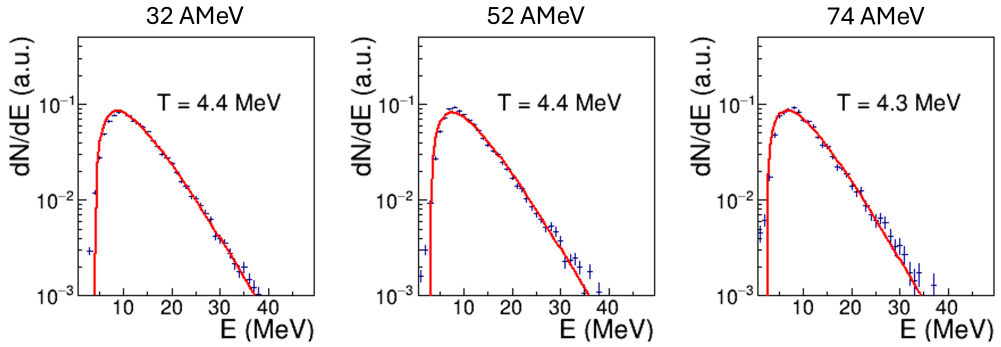

Figure 7.6: Experimental α particles kinetic energy spectra in the QP reference frame for $10° < \theta < 20°$ for $p_{red} = 0.5 - 0.55$. The histograms are normalized to unit area. The red lines show the Maxwellian fit.

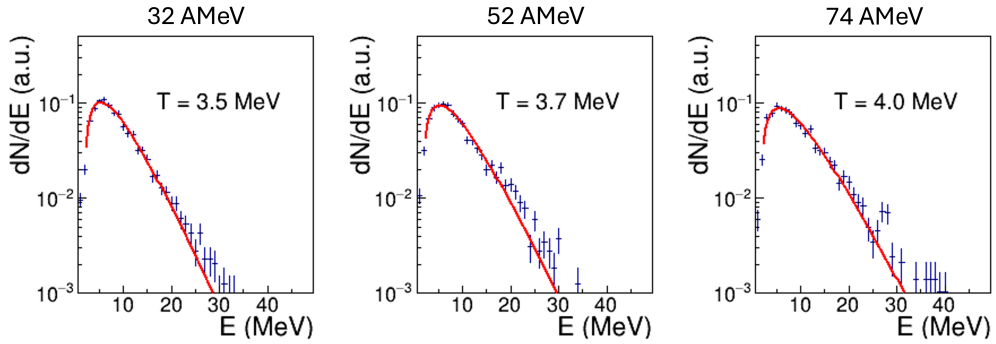

Figure 7.7: Simulated proton kinetic energy spectra in the QP reference frame for $10° < \theta < 20°$ for $p_{red} = 0.5 - 0.55$. The histograms are normalized to unit area. The red lines show the Maxwellian fit.

data, in the following analysis light particles are assumed to originate from two main sources: the excited QP* and a dynamical midvelocity source, associated with the neck region. The pre-equilibrium emission will not be explicitly considered, as it is difficult to quantitatively estimate its contribution due to the fact that its angular distribution is not easily characterized. Nevertheless, one may wonder to what extent this component could affect the results discussed below. Considering that it predominantly affects protons (and neutrons) and that, even in the most unfavourable case, its contribution does not exceed about 15%, a systematic uncertainty on the properties of the primary sources can be roughly estimated to be below 2-3%.

7.3 Disentanglement of evaporation and midvelocity components

Considering as satisfactory the reconstruction of the forward emitted charge and kinetic energy tested previously, in this section the yields and energy contributions associated with the evaporative and the midvelocity components will be evaluated.

As already discussed in Chapter 1, if the evaporative emitting source has low spin values ($< 20\hbar$, as predicted in this case by simulations), isotropic emission is a good approximation. This corresponds to an angular distribution in the QP reference frame (i.e. θ=0 is the QP direction) that can be fitted using the a $\sin(\theta)$ function. Consequently, the deviation from a $\sin\theta$ distribution can be attributed to additional emissions beyond the statistical decay, namely the midvelocity emission.

Fig. 7.8 shows some representative examples of experimental angular distributions in the QP frame for the QPr channel at 74 AMeV for a given centrality selection ($0.5 \leq p_{red} \leq 0.6$). Here, the $\sin\theta$ fit is performed be-

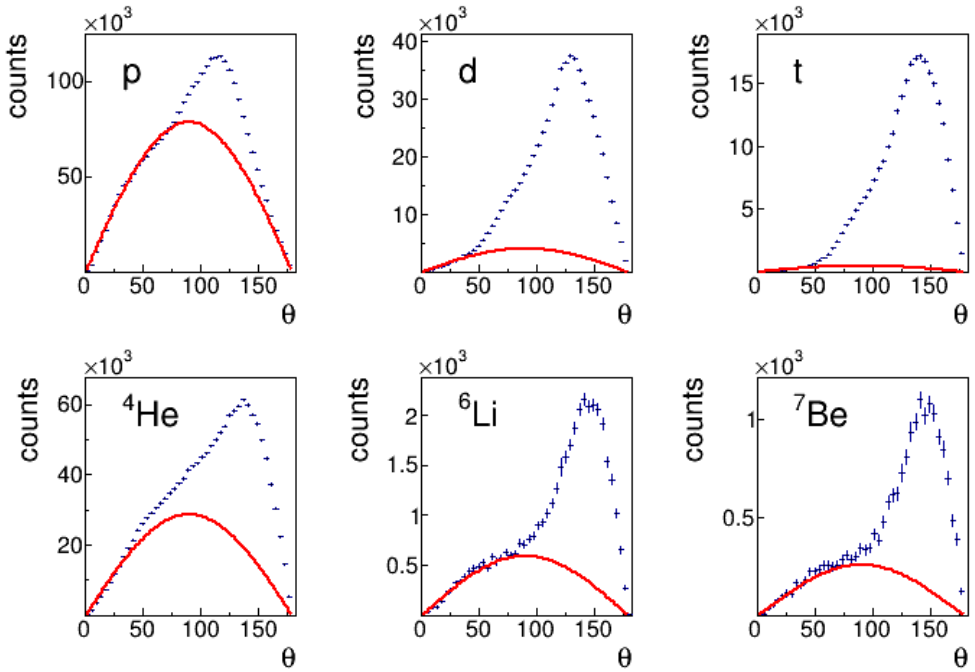

Figure 7.8: Experimental angular distributions (blue markers) in the QP reference frame (θ=0 is the QP direction) for $p_{red} = 0.5 - 0.6$ in the QPr channel at 74 AMeV for p, d, t, ^{4}He, ^{6}Li and ^{7}Be. The red lines show $\sin(\theta)$ fits performed in the angular range $0° < \theta < 45°$.

tween 0° and 45° (red lines), where one could be reasonably confident that only evaporated light fragments are present. The evident excess of emitted particles with respect to the sin(θ) distributions can be ascribed mainly to midvelocity emission. In particular, for the $Z = 1$ isotopes, one observes that the excess at backward angles with respect to the sin(θ) fit increases with the isotope mass. For particles with $Z > 1$ (only the most abundant isotopes are shown) a clear midvelocity excess is observed as well. Similar results are observed for all centralities in both the QPr and QPb channels. Comparable results are obtained also at lower beam energies, although there is a clear increasing of the midvelocity contribution as a function of the increasing bombarding energy. This effect is illustrated in Fig. 7.9, in which the angular distributions of deuterons at the three beam energies, for a specific case ($p_{red} = 0.5 - 0.6$ and QPr channel), are shown.

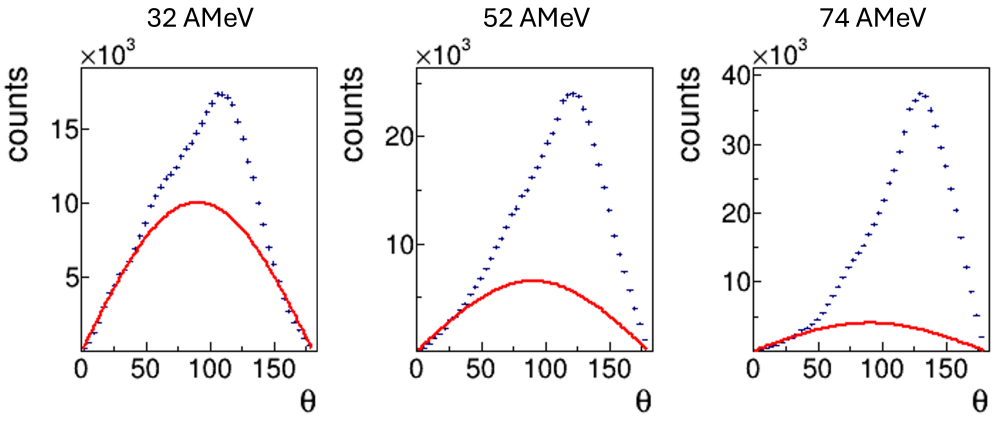

Figure 7.9: Experimental angular distributions of deuterons in the QP reference frame (θ=0 is the QP direction) for $p_{red} = 0.5 - 0.6$ in the QPr channel for the three energies. The red lines indicate $\sin\theta$ fits performed in the range 0 - 45°.

Quantitatively, for the charged particles, the average evaporative multiplicities $\langle M_{C_i}^{evap} \rangle$ are extrapolated from the experimental data measured in the angular range between 0° and 45°. The multiplicities associated with the midvelocity emissions $\langle M_{C_i}^{mid} \rangle$ are then obtained as the difference between the total measured multiplicities and the evaporative ones.

This procedure cannot be applied to neutrons. In the case of neutrons, one must start from the average free neutrons multiplicity estimation $\langle M_n \rangle$ defined in Eq. 7.3 and attempt to assign them to the different sources on the basis of some hypothesis on their neutron content in terms of N/Z. As done in [63], the midvelocity neutron multiplicity $\langle M_n^{mid} \rangle$ is chosen such

that the neck region shares the same N/Z ratio as the entire system (i.e. 1.07). The associated uncertainty is defined as the difference obtained by varying the assumed N/Z ratio of the neck within a reasonable range, from 0.97 to 1.17. The average neutron multiplicity of the evaporative component is then estimated as the difference between the total and the midvelocity multiplicities, namely as $\langle M_n^{ev} \rangle = \langle M_n \rangle - \langle M_n^{mid} \rangle$.

It is now possible to estimate the total mass evaporated from the excited QP* as

$$\langle A_{ev} \rangle = \sum_i A_{C_i} \langle M_{C_i}^{ev} \rangle + \langle M_n^{ev} \rangle \tag{7.7}$$

and by subtracting the evaporative contribution from the total mass of all emitted particles, the mass associated with midvelocity emissions can be estimated as

$$\langle A_{mid} \rangle = \sum_i A_{C_i} \langle M_{C_i} \rangle + \langle M_n \rangle - \langle A_{ev} \rangle. \tag{7.8}$$

Finally, starting from the charge of the QP remnant (QPr channel) or reconstructed (QPb channel) and the corresponding evaporated particles, the charge of the primary excited QP* can be reconstructed as

$$\langle Z_{prim} \rangle = \langle Z_{QP} \rangle + \langle Z_{ev} \rangle \tag{7.9}$$

and analogously for the mass $\langle A_{prim} \rangle$.

For the energy estimation, the average kinetic energies of the evaporative component for the various species are needed. Since, in the emitting system at first order approximation, the kinetic energies of evaporated particles do not depend on the emission angle, the values measured in the range $0^\circ - 45^\circ$ are used to represent the entire evaporative emission. The energy associated to the evaporative emission, namely the initial excitation energy of the QP*, is given by

$$\langle E_{prim} \rangle = \sum_i \langle k_{C_i,ev}^{QP} \rangle \langle M_{C_i}^{ev} \rangle + \langle k_{n,ev}^{QP} \rangle \langle M_n^{ev} \rangle - Q_{ev} \tag{7.10}$$

where $\langle k_{C_i,ev}^{QP} \rangle$ is the average kinetic energy of the evaporated charged particles of the i-th species in the QP frame evaluated in the interval $0^\circ < \theta < 45^\circ$, $\langle k_{n,ev}^{QP} \rangle$ is the average kinetic energy of the evaporated neutrons (estimated from that of the protons after correcting for the Coulomb barrier), and Q_{ev} is the Q-value for separating the primary QP* into the average QP remnant or the average breakup fragments and as many charged particles and neutrons as given by their respective evaporative multiplicities.

By subtracting the evaporative contribution from the total energy of all forward-emitted particles, the energy associated with midvelocity emissions can be estimated as

$$\langle E_{mid} \rangle = \langle E^{cm}_{fwd} \rangle - (\langle E_{prim} \rangle + \langle K_{transl} \rangle). \tag{7.11}$$

where $\langle E^{cm}_{fwd} \rangle$ is the average kinetic energy of the forward emitted light particles evaluated in the cm reference frame, $\langle E_{prim} \rangle$ is the average excitation energy of the primary QP* evaluated in the QP frame and $\langle K_{transl} \rangle$ is the translational kinetic energy of the evaporated particles due to the motion of the source, which can be evaluated as:

$$\langle K_{transl} \rangle \approx \frac{1}{2} m_N \langle A_{ev} \rangle \langle v^2 \rangle \tag{7.12}$$

where m_N is the nucleon mass and v is the velocity of the QP in the cm reference frame.

The final results obtained with the proposed procedure to determine the main properties of the primary QP* prior to its de-excitation, as a function of the selected centrality parameter p_{red}, are shown in Fig. 7.10 for the QPr channel. In this figure, the upper panels display the averaged evaporated mass $\langle A_{ev} \rangle$ (panel (a)), the average charge $\langle Z_{prim} \rangle$ (panel (b)) and the average excitation energy per nucleon $\langle E_{prim} \rangle / \langle A_{prim} \rangle$ (panel (c)) of the primary QP*. The results are shown for the three beam energies (with green, blue and magenta corresponding colours) using the markers for the experimental results and the shaded bands for the simulations. The lower panels of Fig. 7.10 illustrate the properties of the neck region, although its definition as a source is more challenging, namely its average mass $\langle A_{mid} \rangle$ (panel (d)) and average energy per nucleon $\langle E_{mid} \rangle / \langle A_{mid} \rangle$ (panel (e)).

Some comments are needed, starting from the experimental data (solid markers). Concerning panel (a), as expected, the amount of evaporated particles decreases with increasing p_{red}, corresponding to more peripheral and less dissipative collisions. A weak dependence on the beam energy is also observed, with $\langle A_{ev} \rangle$ that weakly increases at lower beam energies. The reconstructed charge of the primary QP* $\langle Z_{prim} \rangle$ (panel (b)), which corresponds to the QP remnant already shown in panel (a) of Fig. 6.3 summed with the evaporated light fragments, shows a decreasing trend with increasing centrality and beam energy. Globally, the experimental QP* remains close to the projectile at 32 AMeV, but becomes much lighter in central collisions at 52 and 74 AMeV. Finally, the average excitation energy per nucleon of the primary QP* (panel (c)) increases with centrality, consistent with the fact that more central collisions correspond to more dissipative processes. Despite differences in the size of the reconstructed QP*, the excitation energy per nucleon remains nearly independent of the beam energy.

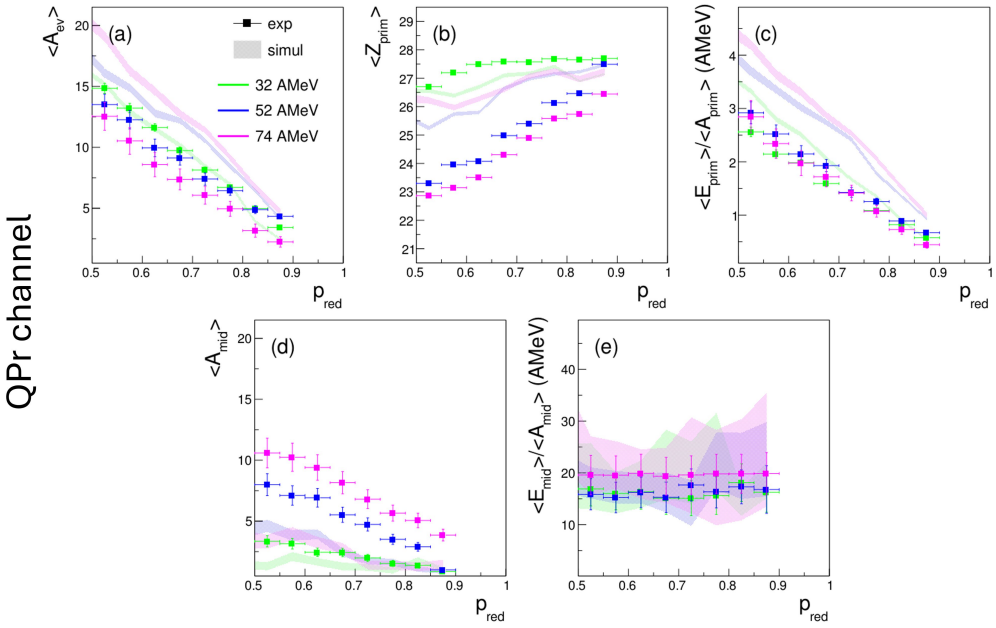

Figure 7.10: Upper row: average mass of the evaporative component $\langle A_{ev} \rangle$ (panel (a)) and average charge $\langle Z_{prim} \rangle$ (panel (b)) and excitation energy per nucleon $\langle E_{prim} \rangle / \langle A_{prim} \rangle$ (panel (c)) of the primary QP* in the QPr channel. Lower row: average mass $\langle A_{mid} \rangle$ (panel (d)) and excitation energy per nucleon $\langle E_{mid} \rangle / \langle A_{mid} \rangle$ (panel (e)) of the midvelocity emission. Solid markers: experimental results; shaded bands: AMD+GEMINI++ simulations.

Concerning the midvelocity component, shown in panel (d) and (e) of Fig. 7.10, it is important to note that the reported quantities refer only to the forward-going midvelocity emission. Considering the symmetry of the system, the energy density can be regarded as fully representative of the total midvelocity emission, whereas the mass corresponds to only half of the total and should be doubled. Turning to the description of the experimental results, at all bombarding energies, the midvelocity contribution increases with centrality. Moreover, the midvelocity component clearly grows with beam energy: starting from a value below 4 amu at 32 AMeV, it reaches around 10 amu at 74 AMeV. The increasing of midvelocity yield with beam energy and centrality, reflects the stronger density gradients that develop in more violent collisions and larger nuclear overlaps. Interestingly, considering the error bars, we find that the midvelocity energy density $\langle E_{mid} \rangle / \langle A_{mid} \rangle$ (panel (e)) is almost independent on the incident energy (with a slight tendency toward larger values at 74 AMeV) and, remarkably, does not depend on centrality, at variance with the QP* source (panel (c)). Although it is not

straightforward to associate this energy density with the thermal excitation energy of a defined nuclear source, its flatness as a function of centrality combined with its large value (around 20 AMeV) strongly supports the hypothesis that the midvelocity emission is of dynamical origin. Similar results, obtained with a different method, were also reported in Ref. [64].

Concerning the model results, the general experimental trends observed in the different panels are reproduced but with a wrong share between the evaporation and the midvelocity contribution. In fact, considering that the simulations reproduce the average charge of the QP remnant (see Fig. 6.3), it is clear that the underestimation of the amount of midvelocity is reflected into an increasing of the evaporation contribution from an hotter primary QP* source. Moreover, the amount of midvelocity emission in this case is less dependent on the bombarding energy compared to the experimental case. Nevertheless, the energy density associated with the dynamical part (panel (e)) is in good agreement with the experimental findings. Finally, the AMD+GEMINI++ results are consistent with the results presented in Chapter 4, where the characteristics of the quasi-projectile are studied at different times within the AMD model. In fact, comparing the results of panel (b) and (c) with Figs. 4.6 and 4.7, although the different centrality estimator, it is evident that the AMD+GEMINI++ results obtained through calorimetry are in agreement with the previous findings. In particular, the calorimetric procedure lead to the estimation of values that are in between those found at t_{sep} and 500 fm/c, confirming that the proposed reconstruction procedure allows to approach the characteristics of the fragments at the end of the dynamical stage.

The same analysis was extended to the QPb channel as presented in Fig. 7.11: the same variables used for the previous figure for the evaporated ($\langle A_{ev}\rangle$, $\langle Z_{prim}\rangle$ and $\langle E_{prim}\rangle/\langle A_{prim}\rangle$) and for the midvelocity ($\langle A_{mid}\rangle$ and $\langle E_{mid}\rangle/\langle A_{mid}\rangle$) components are presented as a function of the p_{red} as centrality estimator. To our knowledge, this is the first time that such a complete reconstruction is attempted for the QPb channel. Of course, in the QPb channel the actual evaporative source is less well defined: particles may be emitted at different times during the fission-like process, i.e. from the splitting phase to the phase of well separated (still excited) breakup fragments. If we assume that the particles are emitted after the breakup, it is very hard to determine from which fission fragment they originate, although they most likely come from the heavier fragment. Nevertheless, using the reconstructed QP as a reference source for the evaporation, the results appear similar to those of the QPr channel: the energy density of evaporated light fragments for each beam energy (panel (c)) shows pronounced dependence on centrality, reaching values up to about 3 AMeV, and a slight dependence on

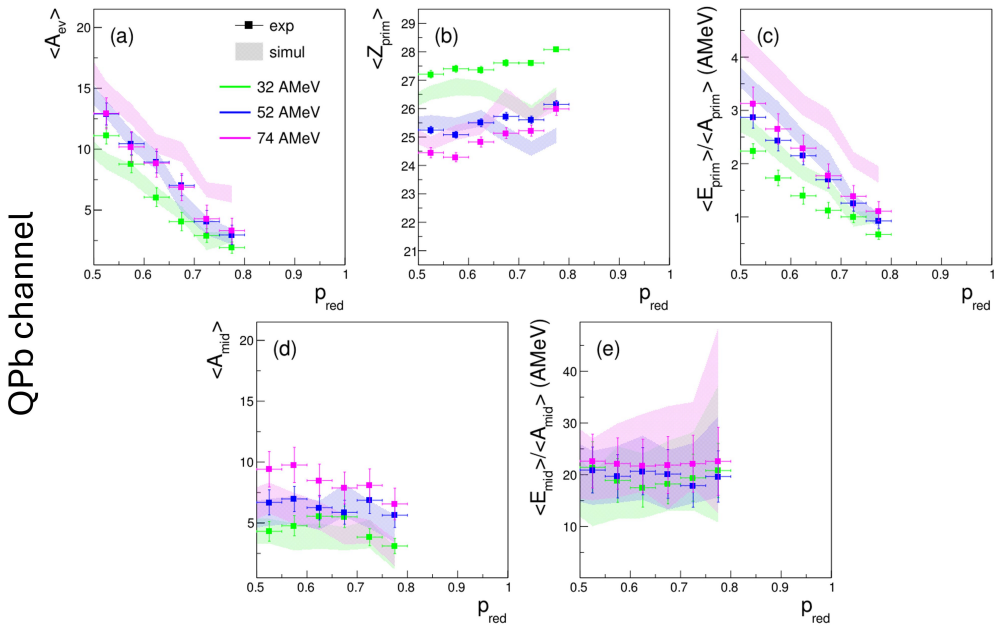

Figure 7.11: Upper row: $\langle A_{ev} \rangle$ (panel (a)), $\langle Z_{prim} \rangle$ (panel (b)) and $\langle E_{prim} \rangle / \langle A_{prim} \rangle$ (panel (c)) of the primary QP* in the QPb channel. Lower row: $\langle A_{mid} \rangle$ (panel (d)) and $\langle E_{mid} \rangle / \langle A_{mid} \rangle$ (panel (e)) of the mid-velocity emission. Solid markers: experimental results; shaded bands: AMD+GEMINI++ simulations.

the incident energy. The behaviour observed for the midvelocity (panel (e)) is markedly different, displaying no dependence on centrality and exhibiting much larger values, around 20 AMeV. Finally, the average mass of the mid-velocity component, $\langle A_{mid} \rangle$ (panel (d)), shows a dependence on beam energy, with higher beam energies corresponding to an increased production of midvelocity fragments.

In Fig. 7.12 the differences between the two selected channels can be more appreciated: using the lowest and highest bombarding energy (32 and 74 AMeV) and some selected panels ($\langle Z_{prim} \rangle$, $\langle E_{prim} \rangle / \langle A_{prim} \rangle$ and $\langle E_{mid} \rangle / \langle A_{mid} \rangle$), the QPr (red) and QPb (blue) experimental values (markers) and simulations (shaded bands) are compared. Comparing the two reaction channels, at 32 AMeV the average charge of the primary QP* (panel (a)) are similar, but the QPb* appear slightly less excited than the QPr* (panel (b)), in agreement with simulations. The energy density of the midvelocity component is instead only marginally different between the two channels. At 74 AMeV, a difference of approximately 1.5 unit between the primary QP* charge (panel (d)) of the QPr and QPb channels is present for the most central collisions,

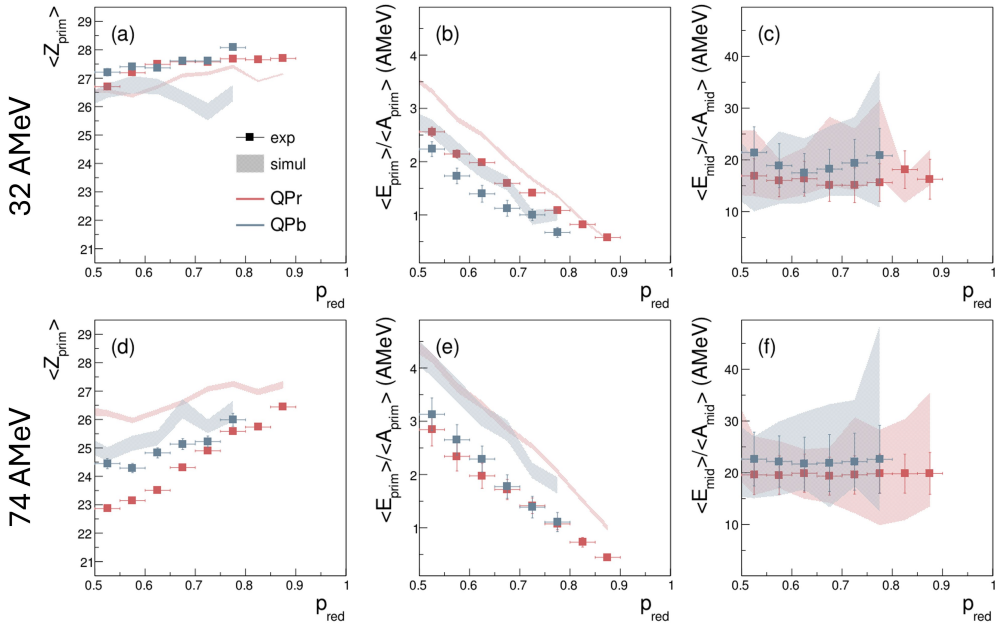

Figure 7.12: Average charge $\langle Z_{prim} \rangle$ (panels (a),(d)) and excitation energy per nucleon $\langle E_{ev} \rangle / \langle A_{prim} \rangle$ (panels (b),(e)) of the primary QP* and energy density of the midvelocity emission $\langle E_{mid} \rangle / \langle A_{mid} \rangle$ (panels (c),(f)) for the QPr (red) and QPb (blue) channels. Upper (lower) row for the reaction at 32 (74) AMeV. Solid markers: experimental results; shaded bands: AMD+GEMINI++ simulations.

while their excitation energies (panel (e)) become more similar. Furthermore, also at 74 AMeV the energy density of the midvelocity component (panel (f)) remains similar in both reaction channels. In any case, the dynamical phase leading to the formation of the QP* appears very similar in the two reaction channels, at least in terms of size and excitation energy, so the resulting excited fragment may or may not undergo breakup.

Finally, in Fig. 7.13 for the 74 AMeV case, the experimental data corrected using AMD+GEMINI++ (solid markers) and HIPSE (open markers) efficiency factors are compared. The agreement between the results obtained with the two corrections is good: only small deviations (less than 1 amu) are observed in $\langle Z_{prim} \rangle$ for the most central QPr events, which may explain the difference observed previously in panel (d) of Fig. 7.12, while all other observables remain fully compatible within errors. This confirms the robustness of the efficiency correction procedure, limiting its impact to small systematic uncertainties. Only the QPr channel is shown, but similar results are obtained for the QPb channel as well.

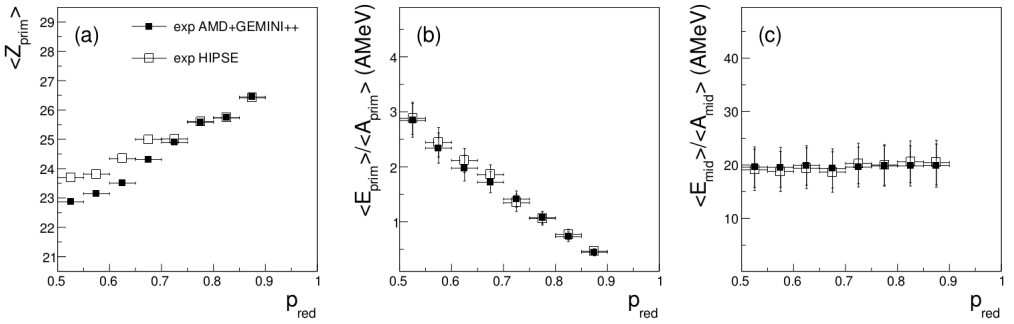

Figure 7.13: Comparison between experimental data corrected with AMD+GEMINI++ (solid markers) and HIPSE (open markers) for the average charge $\langle Z_{prim} \rangle$ (panel (a)) and excitation energy per nucleon $\langle E_{ev} \rangle / \langle A_{prim} \rangle$ (panels (b)) of the primary QP* and energy density of the midvelocity emission $\langle E_{mid} \rangle / \langle A_{mid} \rangle$ (panels (c)) for the QPr channel at 74 AMeV.

In summary, the QP* source behaves consistently as a thermalized source, with an average excitation energy per nucleon strongly dependent on centrality, remaining below 3 AMeV. The mass contribution of the midvelocity source increases with both centrality and beam energy, whereas its energy density is nearly independent on both and takes values of 15-20 AMeV, significantly larger than that of the evaporative source. These findings suggest a dynamical origin for this component, whose yield grows with increasing beam energy. The similarity of results between QPr and QPb channels, especially at higher energies, indicates that the following evolution of the QP*, i.e. its breakup, is largely independent of its mass and excitation energy. Comparison with AMD+GEMINI++ shows that, especially at higher incident energies, the midvelocity component is systematically underestimated by the model relative to the experimental data.

7.4 Isospin characteristics of evaporative and midvelocity emissions

In Chapter 6, we compared the characteristics of particles emitted forward and backward with respect to the QP, providing interesting insights. In addition to the well-known neutron enrichment of the backward-emitted particles, a dependence of the isospin of the forward-emitted component on the beam energy was highlighted. Furthermore, it was observed that the isospin ratio of complex particles emitted forward and backward is the same for both the

QPr and QPb channels.

Here, we extend the study by exploiting the average multiplicities of evaporative and midvelocity emissions to directly compare their isospin content, focusing on complex light particles (CP) with Z<5 and A>1. As in the previous chapter, the isospin analysis excludes free protons and neutrons, since the neutron multiplicities rely on assumptions about their partitioning between evaporative and midvelocity emissions, introducing large uncertainties. Consequently, proton multiplicities are also disregarded.

Fig. 7.14 shows the experimental isospin ratio of complex evaporated particles (solid square markers) and of complex midvelocity emissions (open triangle markers) as a function of p_{red} for the QPr channel. The results are similar to those obtained for the forward/backward-emitted particles (see panel (a) of Fig. 6.12), although some differences are observed.

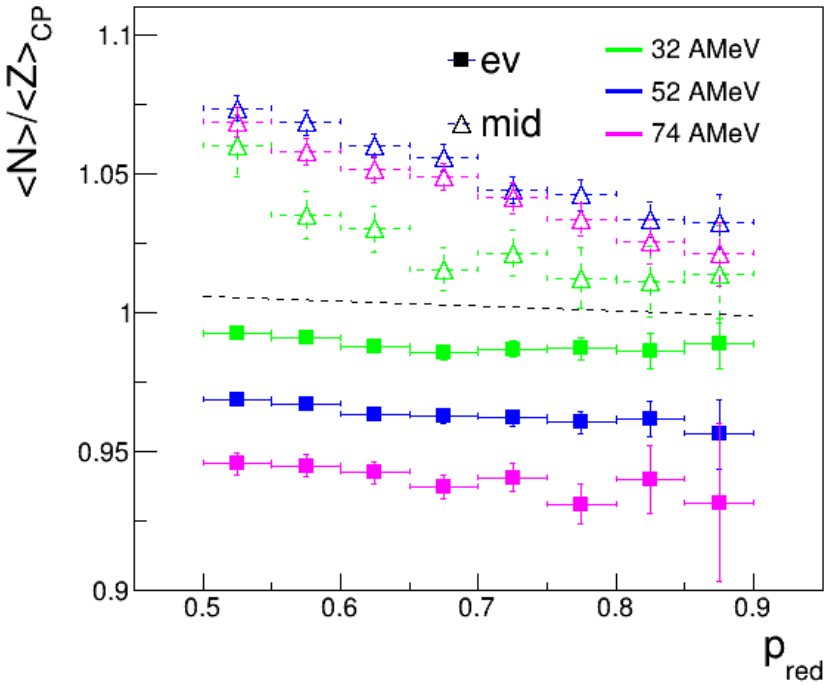

Figure 7.14: Experimental $\langle N\rangle/\langle Z\rangle_{CP}$ of the evaporated complex particles (solid square markers) and those associated with the midvelocity emission (open triangle markers) as a function of p_{red} for the QPr channel. The black dashed lines shows the GEMINI++ results for an excited ^{58}Ni single source at excitation energies between 40 and 120 MeV, with spin below $10\hbar$.

In particular, the absolute values of the midvelocity component, $\langle N\rangle/\langle Z\rangle_{CP}^{mid}$, differ from the backward-emitted component shown in Fig. 6.12, where evap-

oration and midvelocity emissions were mixed. By disentangling these two contributions, it is evident that $\langle N\rangle/\langle Z\rangle_{CP}^{mid}$ shows a clear dependence on centrality, exhibiting a larger neutron enrichment for the most central collisions. Conversely, its dependence on the beam energy is rather weak, with only a noticeable difference between 32 AMeV and the higher energies.

Therefore, the midvelocity yield depends on both centrality and incident energy, while its $\langle N\rangle/\langle Z\rangle_{CP}^{mid}$ is mainly driven by centrality.

Concerning the evaporative component, the more accurate separation between evaporated and midvelocity fragments leads to a slightly neutron-poorer content compared to the forward component shown in Fig. 6.12. The overall trends, however, remain the same, confirming a very weak dependence of the isospin content on centrality, with a clear ordering according to the beam energy. Since the excitation energy per nucleon of the primary QP* at the three energies are similar (panel (c) of Fig. 7.10), it is plausible that the observed differences in the $\langle N\rangle/\langle Z\rangle_{CP}^{ev}$ arise from a different isotopic composition of the emitting QP* source. These variations must be mainly related to different observed midvelocity yields, since the $\langle N\rangle/\langle Z\rangle_{CP}^{mid}$ is essentially independent of the beam energy.

The isospin of the evaporative component can be compared with the results of GEMINI++ simulations considering an excited ^{58}Ni single source at excitation energies between 40 and 120 MeV, with spins assumed below $10\hbar$. In Fig. 7.14, the GEMINI++ results, shown as a dashed black line, are displayed at the centrality values corresponding to the excitation energies estimated via calorimetry. These results tend to be better in agreement with the experimental data at 32 AMeV, where the assumption of a ^{58}Ni QP* is more reliable due to the small contribution of midvelocity emissions. As the beam energy increases, the growing midvelocity contribution results in neutron poorer QP*, and consequently in lower values of $\langle N\rangle/\langle Z\rangle_{CP}^{ev}$.

As already discussed, protons are excluded from the calculation of the isospin ratio used to compare the isospin composition of evaporative and midvelocity emissions. However, it is possible to examine the $Z = 1$ isotope distributions separately to investigate whether a behaviour similar to that shown in Fig. 7.14 can be observed. Fig. 7.15 shows the average mass of $Z = 1$ particles as a function of p_{red} for the midvelocity and evaporative components at the three energies. The $\langle A\rangle$ of H isotopes from the midvelocity emission is consistently higher than that of the evaporative component, reflecting a different mixture of p, d, and t. In particular, the midvelocity emission produces more deuterons and tritons than protons, confirming the neutron enrichment of this component. The $\langle A\rangle$ of the midvelocity component increases with centrality, while its dependence on the incident energy is less clear. In contrast, the average mass of the evaporative component shows

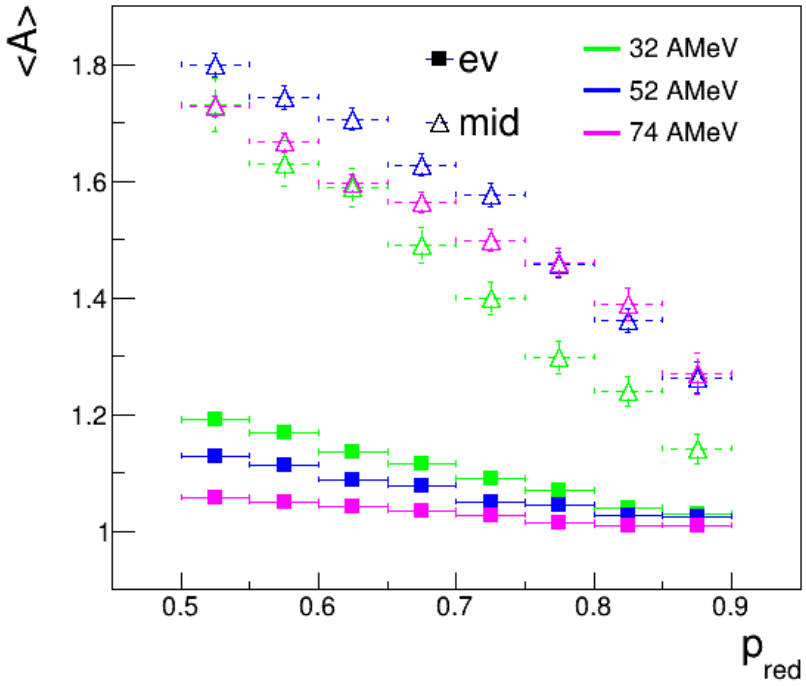

Figure 7.15: Experimental $\langle A \rangle$ of $Z = 1$ evaporated (solid squares) and midvelocity-emitted (open triangles) particles as a function of p_{red} for the QPr channel.

little dependence on centrality, resulting in a growing gap between the two components at higher centralities. In addition, a slight energy dependence is observed for the evaporative component, possibly related to the different amount of midvelocity emission. In conclusion, the analysis of the average mass of $Z = 1$ particles, which allows the inclusion of previously excluded protons, reinforces the previous findings.

Unfortunately, due to the scarce statistics, a complete analysis for the QPb at the three bombarding energies and for all the values of p_{red} similar to those performed for the QPr channel is not possible. Nevertheless, at least in some cases (more central collision at 52 and 74 AMeV) we can compare the results , as proposed in Fig. 7.16. When visible, the overall trend of the QPb channel (blue) is consistent with that of the QPr channel (red), confirming the observations reported in the previous chapter. This further supports the similarity between the QPr and QPb channels. Both the yield and the energy density of the midvelocity component, as well as its isotopic composition, are found to be comparable. Any residual differences could arise from free nucleons, which may explain the variations in the isotopic

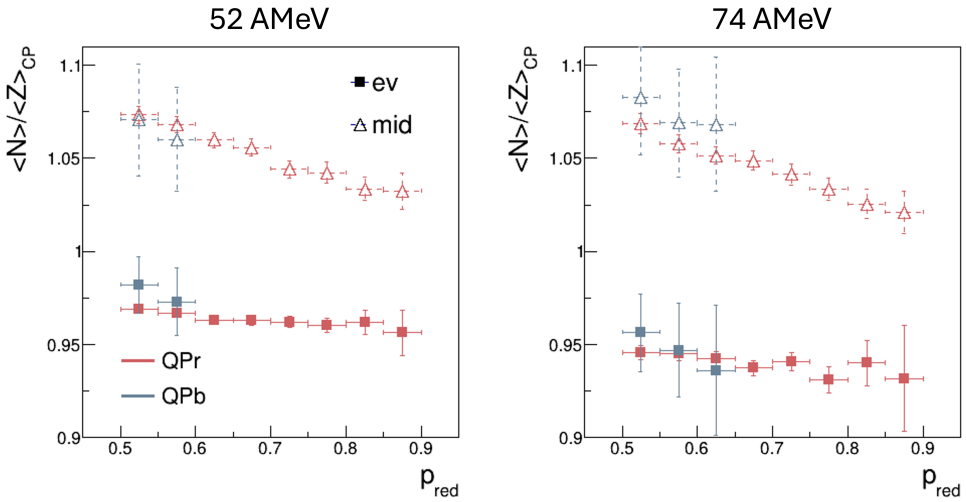

Figure 7.16: Experimental $\langle N\rangle/\langle Z\rangle_{CP}$ of the evaporated (full square markers) and midvelocity (open triangle markers) complex particles as a function of p_{red} for the QPr (red) and QPb (blue) channels.

composition of the remnant and reconstructed QP (see Fig. 6.8).

Conclusions

This work presented a detailed investigation of the semiperipheral ^{58}Ni+^{58}Ni collisions at beam energies of 32, 52, and 74 AMeV, focusing on the evolution of the reaction dynamics as a function of centrality and beam energy.

The experimental data were measured using the coupled INDRA-FAZIA apparatus. The 12 FAZIA blocks at forward angles provide fragment charge and mass identification up to $Z \sim 26$, allowing the isotopic identification of fragments belonging to the QP phase space. INDRA, ensuring an almost 4π angular coverage, provides a reliable global reconstruction of the events.

The use of this apparatus enabled the study of the main reaction channel which, as expected for these collisions at Fermi energies, is the binary dissipative one, where two main excited fragments are produced: the QP and the QT. Since the QP phase space is well measured, it is possible to investigate in detail the properties of the QP as it decays either via particle evaporation, the dominant case, or via a fast breakup process. The former is referred to as the QPr channel, while the latter is denoted as the QPb channel.

The QPr channel is characterized by the presence of a single large fragment, the remnant of the excited primary QP*, accompanied only by light fragments ($Z < 5$). In the QPb channel, two big fragments are emitted forward in the centre of mass frame, from which the breakup source can be reconstructed. This class exhibits the typical features of a dynamical fission, namely the anisotropy of the emission pattern for the most asymmetric splits, with the lighter fragment preferentially emitted backward with respect to the heavier one, i.e., toward the centre of mass [6, 21–27]. Moreover, in both channels, an abundant emission of particles toward the centre of mass (midvelocity emissions) is observed. The selected events are then sorted according to the reduced impact parameter, p_{red}, which is used as a centrality estimator.

The experimental reconstruction of the primary sources, the main goal of this work, starts from a complete characterization of the cold detected fragments as a function of the centrality estimator, for each beam energy. The yields and energies associated with the evaporative and midvelocity emission

were disentangled with the calorimetric method and the primary QP* and the neck sources reconstructed. For the first time such a reconstruction was performed in both the QPr and QPb channels, suggesting similar properties of the primary sources.

The results, presented in Figs. 7.10 and 7.11 for the QPr and QPb channel, respectively, show that the average charge of the reconstructed QP* decreases with increasing centrality and beam energy; consequently, a larger fraction of particles is emitted prior the full thermalization, contributing to the midvelocity source. The excitation energy per nucleon of the QP*, as expected for an equilibrated source, remains below 3 AMeV and increases with centrality while is almost independent on the beam energy. On the contrary, the energy density of the neck source, although in this case the definition of a source is more questionable, is significantly higher, reaching 15-20 AMeV per nucleon, and shows no dependence on either centrality or beam energy. These findings confirm the dynamical origin of this source, which corresponds to a very hot overlapping region formed during the collision.

The similarity of results between QPr and QPb channels suggests that the following evolution of the QP*, namely its breakup, is largely independent of its size and excitation energy.

The same procedure for the primary source reconstruction was applied also to the filtered AMD+GEMINI++ simulations. Despite the overall satisfactory reproduction of characteristics of the secondary fragments, the simulations shows significant differences in the properties of the primary emitting sources. Indeed, the midvelocity contribution is underestimated at higher energies and results only slightly increasing with the beam energy. Nevertheless, they reproduce well the energy density of the neck source. As a consequence, less energy and mass is emitted in the first phases and the resulting primary QP* appear hotter and heavier than those deduced from the experimental data.

Some systematic uncertainties affect these results. One arises from the procedure used for estimating the detection efficiency correction for light fragments. The use of two different corrections, obtained with two different event generators, allowed an estimation of the systematic uncertainty related to this procedure to be below $\sim$5%, while the extracted energy densities remain compatible within the errors. Another systematic uncertainty arises from the fact that in this procedure the possible contribution of the pre-equilibrium emission in neglected. This emission occurs at the very initial stage of the collision, where mainly single nucleons (protons and neutrons) are emitted as a result of direct n-n collisions. This contribution cannot be easily estimated; however, a rough estimation suggests a systematic error in the reconstruction of the primary sources below the 2-3%.

The reaction times accessible through the proposed reconstruction procedure were assessed using AMD+GEMINI++ simulations. Within this model, the properties of the primary QP* source can be independently evaluated as a function of time. The simulation results indicate that the sources reconstructed through the calorimetric procedure correspond to reaction times of approximately 100-300 fm/c from the onset of the collision, confirming that the proposed reconstruction procedure allows to approach the characteristics of the fragments at the end of the dynamical stage.

Concerning the neutron enrichment of the neck, it was clearly observed by comparing the isospin content of the evaporative and midvelocity components in the QPr channel (Fig. 7.14), after having excluded the free nucleons in order to avoid the bias due to the undetected neutrons. Similar behaviour was shown in the QPb channel (Fig. 7.16) in a limited range of centrality, where the statistics was enough to allow a comparison.

For all centralities and beam energies the midvelocity component is more neutron rich than the evaporative one. The N/Z of the midvelocity emission increases with the centrality and is essentially independent on the beam energy. For the evaporative component an interesting dependence on the beam energy emerges. At 32 AMeV the N/Z is close to that expected for the pure statistical evaporation from a ^{58}Ni. As the energy increase, the N/Z decreases. This trend with the incident energy, given the similarities in the excitation energy per nucleon of the QP* source, can be linked to a different isospin content of the QP* source. Since the neutron enrichment of the midvelocity component weakly depends on the beam energy, this effect in mainly driven by the increasing abundance of midvelocity yield: as the energy increases, the growing midvelocity contribution leaves the QP* slightly more neutron poor. The isospin content of the QP* consequently influences both the evaporated particles and the final QP remnant.

In conclusion, the midvelocity emission plays a role in determining the characteristics of the primary QP*, as observed in [61], and our results seem to indicate that, as a function of the beam energy, the effect is mainly driven by the increasing amount of neck emissions. It is also worth noting that the neutron enrichment of the midvelocity component is inconsistent with a full participant-spectator scenario, which is typically relevant at higher bombarding energies. In such a scenario, the midvelocity region would not exhibit significant neutron enrichment. Therefore, the observed neutron enrichment at midvelocity points to the formation of a neck structure, even at the highest investigated energy of 74 AMeV.

The results obtained for the QPb channel are consistent with those of the QPr channel, suggesting that the midvelocity particles occur before the following evolution of the excited QP*.

Overall, this study demonstrates the power of combined high-resolution isotopic measurements and careful source reconstruction in elucidating the complex interplay of statistical and dynamical processes in semiperipheral collisions. The results provide detailed information about the primary QP* properties, showing how they are affected by midvelocity emission and how they evolve with centrality and beam energy. These findings offer a benchmark for transport model predictions and contribute to a deeper understanding of isospin transport phenomena at Fermi energies.

Appendix A

Energy thresholds for Z and A identification using PSA

This appendix presents the evaluation of the energy thresholds for charge and mass identification using Pulse Shape Analysis on FAZIA Si1 detectors. It is noteworthy that this is the first time such an evaluation has been performed for the entire FAZIA apparatus. Indeed, the PSA energy thresholds reported in [70] refer to a single detector, whereas the values estimated here are representative of all 12 blocks currently in use.

As mentioned in Chapter 2, it is well known that doping uniformity is an essential property to achieve good results in charge and mass identification with PSA and for such a reason silicon detectors with the highest possible doping uniformity are used. Initially, the silicon detectors used by the collaboration were Neutron Transmutation Doped (nTD) material, which is known to provide the best resistivity homogeneity available to date. The non-uniformity of these detectors was tested in laboratory with a non-destructive method developed by the FAZIA collaboration [69]. This technique, based on scanning the detector surface with a collimated pulsed light source, allows a direct resistivity measurement as a function of position with millimetric resolution. The detectors were operated in reverse-mount configuration, and charge signals were collected at different applied voltages and for various (x, y) positions in which the collimated light source was impinging. Averaging over many charge signals, it is possible to extract the average signal risetime for each applied voltage-position combination: the typical decreasing of the charge risetime as a function of the applied voltage will end at the moment that a complete depletion is reached. So, using an opportune fit (see [69] for all details), it is possible to extract for each (x,y) position the

"local" depletion voltage. Using the formula:

$$\rho(x,y) = \frac{d^2}{2V_{depl}(x,y)\varepsilon_R\mu} \tag{A.1}$$

where ρ is the resistivity, d the detector thickness, μ the mobility and ε_R is the dielectric constant of the silicon, it is possible to extract an absolute resistivity map, as shown in Fig. A.1. This procedure makes it possible to

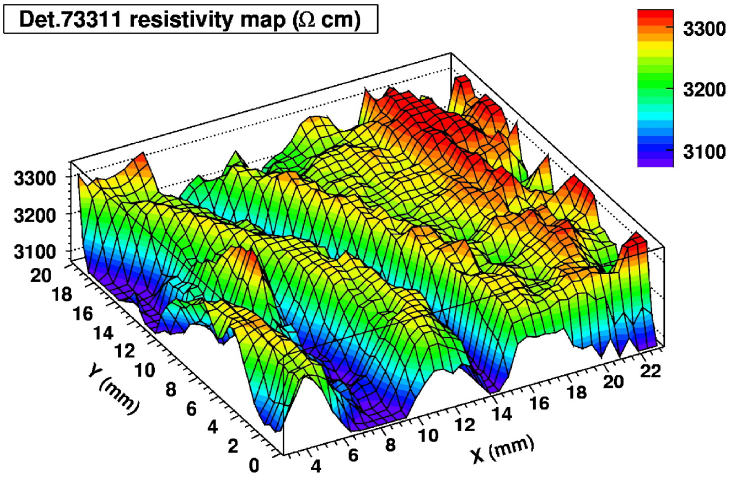

Figure A.1: Example of an absolute resistivity map obtained with the described method using a 0.5 mm scanning step. Taken from [69].

experimentally characterize the doping non-uniformity of the silicon detectors, quantified by the FWHM variation of the resistivity across the detector area. This method was used to reject silicon detectors that didn't match the resistivity uniformity requirements.

The particle identification performance of these detectors, with a doping uniformity typically better than 6% FWHM, was tested during one of the first physics experiments. In particular, the achievable energy thresholds for Z and A identification using PSA on the first Si layer were evaluated for a single silicon detector as representative of the four blocks present at that time [70].

After the first experiments with few blocks, a large-scale production of detectors was carried out to equip the 12 FAZIA blocks currently in use. Unfortunately, nTD material was no more available and so these silicon detectors are manufactured from TOPSIL Ultra-Homogeneous High Purity Silicon (UHPS) substrates, with a declared doping homogeneity below 10%. However, this specification has never been directly verified by the collaboration, because of the large number of detectors involved and the urgency of making

them available for physics experiments. It is therefore important to evaluate the PSA identification thresholds for the entire FAZIA apparatus, which includes detectors from different manufacturers. For the first time, such an evaluation is performed here.

To define the energy thresholds, we follow the same procedure proposed in [70], based on the Figure of Merit (FoM) method. As explained in details in Chapter 3, starting from the identification grid, the PID vs Energy correlation is built and then divided into consecutive energy intervals, chosen in order to have enough statistics. For each interval, the data are projected on the PID axis by integrating the event density over the energy interval, thus obtaining the PID distribution spectra relative to that energy range. The separation between two adjacent peaks in the PID spectrum is quantified by the FoM, defined as:

$$FoM = \frac{PID_2 - PID_1}{FWHM_2 + FWHM_1} \tag{A.2}$$

where PID_1 and PID_2 are the centroids of two peaks and $FWHM_1$ and $FWHM_2$ their widths. The identification threshold is defined as the lowest energy at which the FoM is greater than 0.7, a conventional reference value for well separated peaks. To get the energy threshold for the Z identification, a two Gaussian fit is performed for each element pair, as shown in the left panel of Fig. A.2 for Z=5 and Z=6. For the isotopic separation

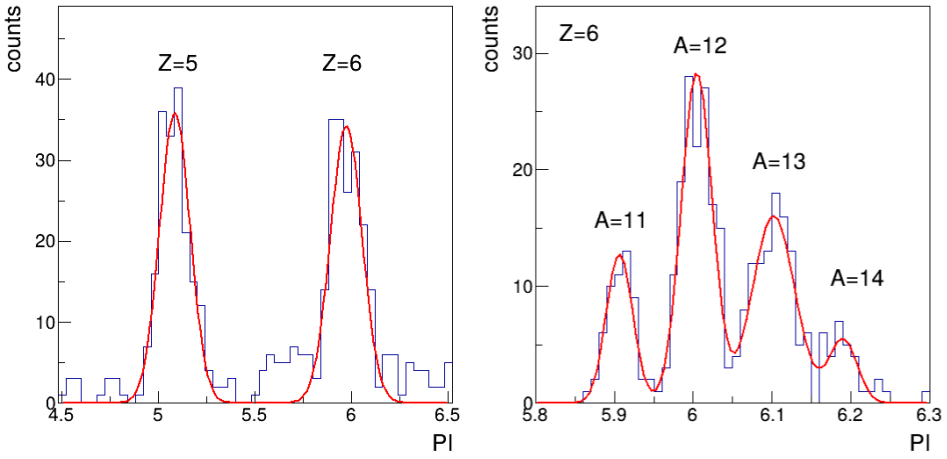

Figure A.2: Left panel: PID spectrum of Z=5 and Z=6 for a given energy interval (blue) with the corresponding two-Gaussian fit (red) are shown. Right panel: the PID spectrum of carbon isotopes for a different energy interval (blue) with the corresponding multi-Gaussian fit (red).

thresholds, a multi-Gaussian fit is performed on each element, and the FoM

is calculated for the two most abundant isotopes, as shown in the right panel of Fig. A.2 for carbon isotopes (A=12 and A=13).

This procedure has been applied to all working Si1 detectors (more than 150) for the ^{58}Ni+^{58}Ni reaction at 32 AMeV, where the statistic of ions stopped in Si1 is higher compared to the same reaction at higher energies. In this way, an average energy threshold for charge (blue square markers in Fig. A.3) and mass (blue star markers) identification as a function of Z was obtained, fully representative of the FAZIA apparatus. These results can be directly compared with the previous measurements (black symbols) reported in Ref. [**pastore20017**]. The outcome of this direct comparison shows that

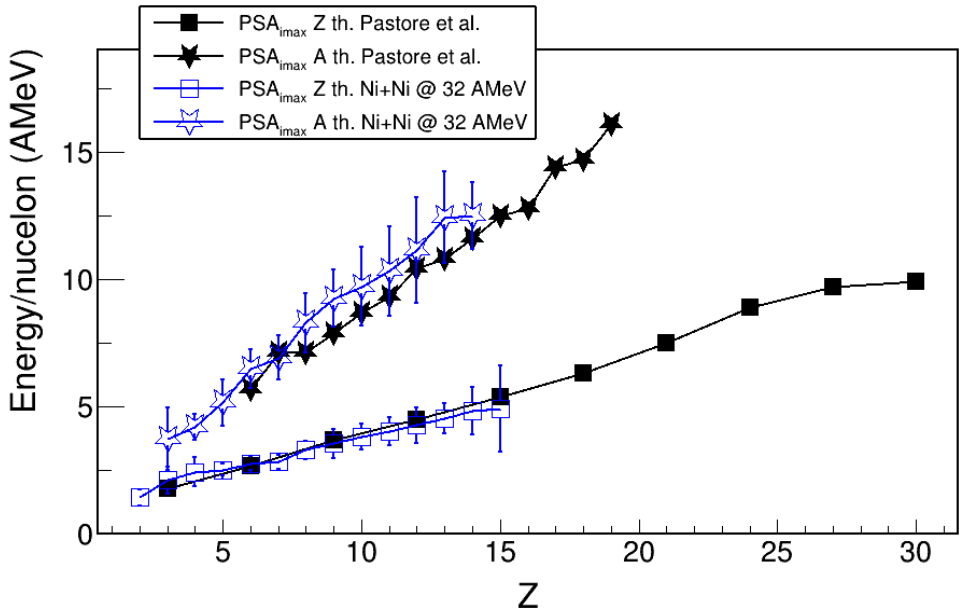

Figure A.3: Energy thresholds for Z and (Z,A) identification via PSA on FAZIA Si1 detectors. In black, the thresholds from [70] obtained with a single detector. In blue, the average thresholds obtained using all the FAZIA Si1 detectors.

the average thresholds extracted here are consistent, within the error bars, with the earlier results. In this analysis, the error bars attributed to the average values correspond the maximum deviations, showing that some detectors perform slightly better and others slightly worse than those reported in [70]. It is worth noting that the average thresholds for charge identification are essentially unchanged with respect to [70], while those for mass identification are found to be slightly higher, although still compatible within the uncertainties. This may suggest that the sensitivity to doping homogeneity

is more pronounced in the case of isotopic identification. Nevertheless, these results globally indicate that the PSA performance of the FAZIA apparatus does not differ significantly from that previously estimated for a typical nTD detector.

Appendix B

Response of FAZIA CsI(Tl) to energetic protons

This appendix presents the results obtained by the collaboration for the intrinsic detection efficiency of the FAZIA CsI(Tl) crystals and discusses their impact on the physics experiments analyzed in this thesis.

In recent years, some studies have reported experimental evidences of a decreasing detection efficiency of CsI(Tl) crystals for LCPs as a function of their energy [80, 124]. This occurs because particles along their path in the detector can interact with the crystal, leading either to the transmutation of colliding nucleus or to the scattering of the particle out of the crystal. In both cases, the LCP deposits only a part of its initial energy. In the following, we will refer to them as Incomplete Energy Deposition (IED) particles, while particles depositing their full energy are labelled as Complete Energy Deposition (CED). As already shown in [80], due to their nature, IED particles are also displaced from their typical positions within the Pulse Shape Analysis (PSA) identification matrix, filling the region below the proton line, which is typically associated with gamma rays.

The probability of IED due to nuclear reactions is governed by the cross sections, which increase smoothly with the energy. Also the averaged lateral scattering due to multiple Coulomb scattering along the path of the impinging particle in the CsI(Tl) crystal increases with the LCP energy, producing a larger fraction of escaping particles in case of elongated crystals and lighter particles. This is particularly relevant for the FAZIA detector, whose CsI crystals have a 20x20 mm^2 face and a 10 cm thickness. Since light charged particle detection and identification rely mainly on the CsI(Tl) (see Section 3.1), the IED effect cannot be neglected in experiments with beam energies above 30 AMeV, where forward emitted protons can exceed 100 MeV. Considering the beam energies employed in recent FAZIA experiments

(up to 74 AMeV) and the possible future activities involving Rare Isotope Beams at even higher energies, it is crucial to determine the efficiency of FAZIA CsI(Tl) scintillators especially for energetic protons, for which the IED fraction may become significant.

A first test of these scintillators was conducted at the CCB facility in Cracow [80]. However, the use of two collimated FAZIA crystals didn't allow to estimate the efficiency in normal operating conditions. For such a reason, a second experiment was preformed at CNAO (Pavia) in atmosphere (no vacuum chamber was available there), using a complete not collimated FAZIA block mounted at the nominal design distance (100 cm) from the target. Details of the experimental setup can be found in [125]. The detector was irradiated with protons elastically scattered from a gold foil target with a thickness of 6 μm. Several proton beam energies were employed: 70 MeV (close to the minimum available beam energy), 100, 130, 160, and 190 MeV (near the maximum energy at which protons can be fully stopped within the CsI(Tl) crystal used).

The intrinsic identification efficiency can be determined as the ratio between the number of CED protons, N_{CED}, and the total number of protons entering the crystal, $N_{CED} + N_{IED}$. These quantities can be experimentally determined by exploiting the Si1+Si2-CsI ΔE-E and the PSA in CsI correlations. In the Si1+Si2-CsI correlation, as shown in panel (a) of Fig. B.1, all impinging particles , regardless of their later interactions in the CsI(Tl) crystals, can be selected by applying a condition on the energy released in the silicon detectors (black solid lines). Then, in the CsI PSA matrix under the previous condition, the events that are correctly recognized as protons also in CsI (CED) can be selected using a graphical cut (red line), as shown in panel (b). Note that the Si1+Si2 energy selection also imposes a lower limit on the energy deposited in CsI(Tl) by the CED protons, highlighted in Fig. B.1 with the dashed black lines. It is worth mentioning that the condition on the silicon detectors strongly reduces possible contamination of gamma-rays, neutrons and protons coming from neighbouring crystals. These two selections enable the estimation of the intrinsic efficiency. Finally, panel (c) shows the CsI energy distributions for CED events (red line) and CED+IED events (black line). Considering the broad energy distribution of well-identified protons, caused by inelastic scattering and contributions from protons interacting inside and outside the target, the average of this distribution is taken as the effective impinging energy.

In Fig. B.2, the proton efficiency as a function of their energy for the quartets Q1 (black markers) and Q4 (red markers), obtained averaging their available telescopes, are shown. In this average, the two telescopes closest to the beam (Q1T4 and Q4T1) were excluded because they exhibited a different

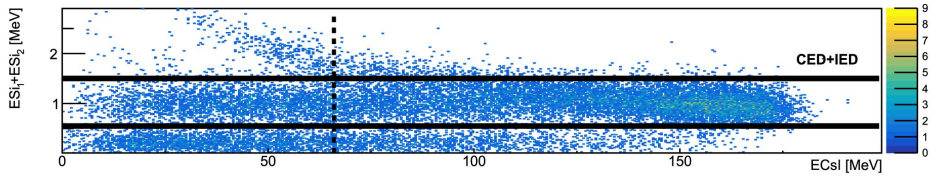

(a) Si1+Si2-CsI ΔE-E correlation

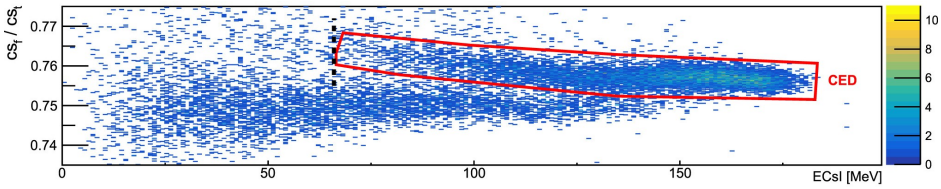

(b) CsI PSA correlation

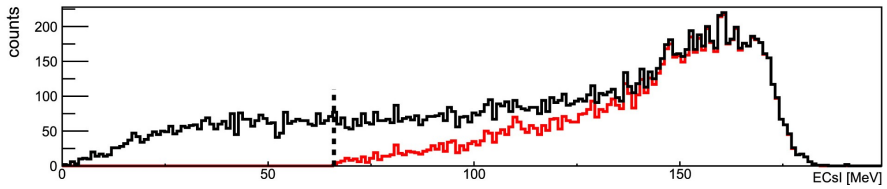

(c) CsI energy distributions

Figure B.1: In panel (a) the Si1+Si2-CsI ΔE-E correlation for a telescope at 190 MeV is shown. The black solid lines correspond to the selection of the CED+IED protons. In panel (b) the CsI PSA correlation for the selected events is presented with the red cut that separates the CED events. In panel (c) the CsI energy distributions of the CED+IED events (black line) and CED events (red line) are drawn. Figures taken from [125].

behaviour compared to the other telescopes due to the dominant presence of Rutherford scattering, which strongly focuses protons toward the forward side of the telescope, thereby enhancing proton escape from the crystals. The other quartet are not shown because they did not have sufficient statistics. The efficiency, very similar for Q1 and Q4, as expected, continuously drops with proton energy and it results to be just below 90% even at the lower probed energy. Experimental detection efficiencies have been also compared with a dedicated GEANT4 simulation, including the proton interaction processes and the full experimental set-up. The procedure used to extract the proton efficiency and the corresponding energy is similar to the experimental one. The GEANT4 simulation result is also shown in Fig. B.2 (blue open markers). In this case only one curve is shown since the Q1 and Q4 quartets are symmetric with respect to the beam and therefore equivalent from the simulation perspective. It is evident that the experimental proton identifi-

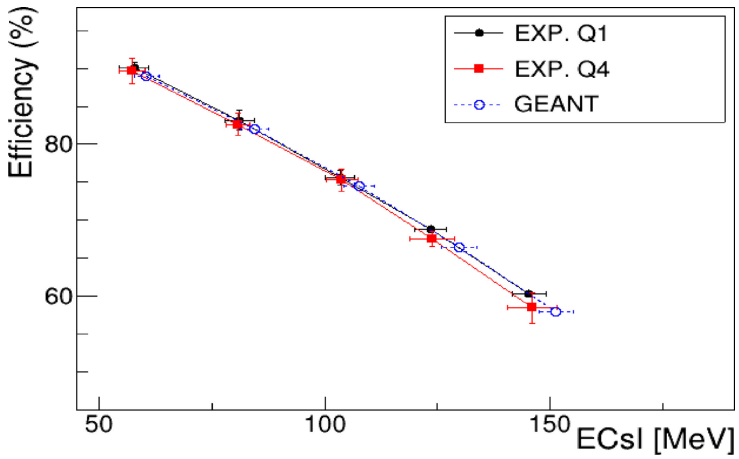

Figure B.2: Proton efficiency as a function of their energy obtained averaging the values of the selected telescopes for Q1 and Q4 and the corresponding GEANT4 simulation. Taken from [125].

cation efficiency as a function of energy is well reproduced by the GEANT4 simulation.

We may wonder what the effect of this inefficiency is on physics experiments. In fact, due to its energy dependence, it affects not only the particle yields but also the shape of the kinetic energy spectra. To investigate this effect, we used the data from the ^{58}Ni+^{58}Ni reaction at 74 AMeV, where the effect is expected to be more relevant. The GEANT simulation reported in Fig. B.2, which follows very well the experimental trend over a wide energy range, has been used to extrapolate the efficiency values also at higher energies.

Let us first consider the effect when the analysis is performed without any further selection. In Fig. B.3, the total energy spectrum of protons detected in the ^{58}Ni+^{58}Ni reaction at 74 AMeV with the full FAZIA apparatus is shown in black, while the red line corresponds to the same spectrum corrected for the inefficiencies described above. Concerning the multiplicities, the total number of detected protons increases from 8.6×10^7 to 1.06×10^8 after the correction, corresponding to a loss of about 19%. This represents the overall impact of IED inefficiencies in the ^{58}Ni+^{58}Ni reaction at 74 AMeV. The effect is mitigated when including the protons detected in INDRA. Assuming an efficiency of unity for the INDRA CsI(Tl) detectors, due to their larger size and the fact that they primarily detect less energetic protons, the proton loss is reduced to approximately 3%.

Fig. B.3 illustrates the impact of FAZIA CsI(Tl) efficiency in a fully inclusive analysis. More relevant and interesting for the present work is the

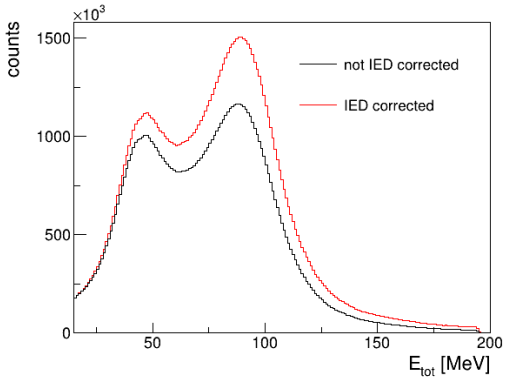

Figure B.3: The uncorrected (black line) and corrected (red line) total energy spectra of protons detected in the FAZIA apparatus for the ^{58}Ni+^{58}Ni reaction at 74 AMeV.

possible proton loss associated with the event selections applied in the analysis. In Fig. B.4, the uncorrected (black) and corrected (red) spectra are shown for protons detected in both FAZIA and INDRA, emitted forward with respect to the centre of mass, for the QPr (left panel) and QPb (right panel) channels. Within this selections, the proton loss amounts to about 6%.

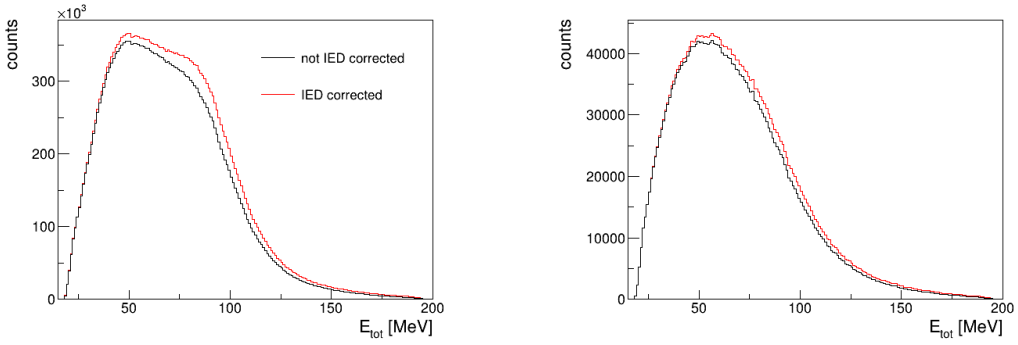

Figure B.4: Total energy spectra of protons emitted forward with respect to the centre of mass in the ^{58}Ni+^{58}Ni reaction at 74 AMeV for the QPr (left panel) and QPb (right panel) channels. The black line shows the uncorrected spectrum, while the red line shows the spectrum corrected for the IED inefficiency.

Given this non-negligible contribution, the corresponding efficiency correction was applied to experimental proton yield in the analysis presented in

this work. Possible efficiency corrections for deuterons, tritons, and α particles have been neglected so far, waiting for other experimental studies of the FAZIA collaboration, which are ongoing for α particles. In any case, considering that the IED particles in the FAZIA CsI(Tl) are mainly generated by elastic scattering leading to the escape of the particle from the crystals, it is clear that the maximum effect is expected for protons. Obviously, this correction is applied only to experimental data, while no correction is applied to filtered simulations, since IED inefficiency effects are not included in the filtering procedure.

Bibliography

[1] A. Sorensen et al., Prog. Part. Nucl. Phys. **134**, 104080 (2024).

[2] J. Łukasik et al., Phys. Rev. C **55**, 1906 (1997).

[3] S. Piantelli et al., Phys. Rev. C **74**, 034609 (2006).

[4] T. Lefort et al., Nucl. Phys. A **662**, 397 (2000).

[5] Y. Larochelle et al., Phys. Rev. C **62**, 051602(R) (2000).

[6] B. Davin et al., Phys. Rev. C **65**, 064614 (2002).

[7] A. Pagano et al., Nucl. Phys. A **A734**, 504 (2004).

[8] E. Galichet et al., Phys. Rev. C **79**, 064614 (2009).

[9] S. Hudan et al., Phys. Rev. C **70**, 031601(R) (2004).

[10] M. Jandel et al., J. Phys. G: Nucl. Part. Phys. **31**, 29 (2005).

[11] V. Baran et al., Nucl. Phys. A **730**, 329 (2004).

[12] V. Baran et al., Nucl. Phys. A **703**, 603 (2002).

[13] L. G. Sobotka et al., Phys. Rev. C **50**, R1272(R) (1994).

[14] M. Colonna et al., Nucl. Phys. A **589**, 160 (1995).

[15] J. F. Dempsey et al., Phys. Rev. C **54**, 4 (1996).

[16] P. M. Milazzo et al., Phys. Lett. B **509**, 204 (2001).

[17] R. Lionti et al., Phys. Lett. B **625**, 33 (2005).

[18] M. Di Toro et al., Eur. Phys. J. A **30**, 65 (2006).

[19] E. Galichet et al., Phys. Rev. C **79**, 064615 (2009).

[20] E. De Filippo et al., Phys. Rev. C **86**, 014610 (2012).

[21] P. Glässel et al., Z. Phys. A **310**, 189 (1983).

[22] G. Casini et al., Phys. Rev. Lett. **71**, 2567 (1993).

[23] A. A. Stefanini et al., Z. Phys. A **351**, 167 (1995).

[24] R. Moustabchir et al., Nucl. Phys. A **739**, 15 (2004).

[25] S. Piantelli et al., Phys. Rev. C **107**, 044607 (2023).
[26] F. Bocage et al., Nucl. Phys. A **676**, 391 (2000).
[27] E. De Filippo et al., Phys. Rev. C **71**, 064604 (2005).
[28] A. Jedele et al., Phys. Rev. Lett. **118**, 062501 (2017).
[29] A. B. McIntosh et al., Phys. Rev. Lett. **81**, 034603 (2010).
[30] A. Rodriguez Manso et al., Phys. Rev. C **95**, 044604 (2017).
[31] A. Rodriguez Manso et al., Phys. Rev. C **100**, 044612 (2019).
[32] B. Harvey et al., Phys. Rev. C **102**, 064625 (2020).
[33] S. Piantelli et al., Phys. Rev. C **101**, 034613 (2020).
[34] A. Jedele et al., Phys. Rev. Lett. **107**, 024601 (2023).
[35] W. Rösch et al., Nucl. Phys. A **496**, 141 (1989).
[36] L. Lassen et al., Phys. Rev. C **55**, 1900 (1997).
[37] E. Plagnol et al., Phys. Rev. C **61**, 014606 (1999).
[38] L. G. Sobotka et al., Phys. Rev. C **62**, 031603 (2000).
[39] S. Barlini et al., Phys. Rev. C **87**, 054607 (2013).
[40] S. Piantelli et al., Phys. Rev. C **103**, 014603 (2021).
[41] Q. Fable et al., Phys. Rev. C **107**, 014604 (2023).
[42] P. Danielewicz et al., Nucl. Phys. A **727**, 233 (2003).
[43] V. Baran et al., Phys. Rep. **410**, 335 (2005).
[44] B. A. Li et al., Phys. Lett. B **727**, 276 (2013).
[45] K. Iida et al., Eur. Phys. J. A **50**, 42 (2014).
[46] J. Carlson et al., Prog. Part. Nucl. Phys. **94**, 68–124 (2017).
[47] J. Margueron et al., Phys. Rev. C **97**, 025805 (2018).
[48] X. Roca-Maza et al., Prog. Part. Nucl. Phys. **101**, 96–176 (2018).
[49] W. Lynch et al., Phys. Lett. B **830**, 137098 (2022).
[50] R. Płaneta et al., Phys. Rev. C **38**, 195 (1988).
[51] A. A. Marchetti et al., Phys. Rev. C **48**, 266 (1993).
[52] H. Madani et al., Phys. Rev. C **51**, 2562 (1995).
[53] M. B. Tsang et al., Phys. Rev. Lett. **92**, 062701 (2004).
[54] T. X. Liu et al., Phys. Rev. C **76**, 034603 (2007).
[55] I. Lombardo et al., Phys. Rev. C **82**, 014608 (2010).

[56] S. Piantelli et al., Phys. Rev. C **88**, 064607 (2013).

[57] L. W. May et al., Phys. Rev. C **98**, 044602 (2018).

[58] A. Camaiani et al., Phys. Rev. C **103**, 014605 (2021).

[59] C. Ciampi et al., Phys. Rev. C **106**, 024603 (2022).

[60] C. Ciampi et al., Phys. Rev. C **108**, 054611 (2023).

[61] D. Thériault et al., Phys. Rev. C **71**, 014610 (2005).

[62] D. Thériault et al., Phys. Rev. C **74**, 051602(R) (2006).

[63] A. Mangiarotti et al., Phys. Rev. Lett. **93**, 232701 (2004).

[64] G. Lanzanò et al., Nucl. Phys. A **683**, 566 (2001).

[65] D. Gourio et al., Eur. Phys. J. A **7**, 245 (2000).

[66] R. Bougault et al., Eur. Phys. J. A **50**, 47 (2014).

[67] S. Valdré et al., Nucl. Instrum. Meth. A **930**, 27 (2019).

[68] A. Camaiani et al., Eur. Phys. J. Plus **139**, 1134 (2024).

[69] L. Bardelli et al., Nucl. Instrum. Meth. A **602**, 501 (2009).

[70] G. Pastore et al., Nucl. Instrum. Meth. A **860**, 42 (2017).

[71] N. Le Neindre et al., Nucl. Instrum. Meth. A **710**, 145 (2013).

[72] J. Pouthas et al., Nucl. Instr. Meth. A **357**, 418 (1995).

[73] J. Pouthas et al., Nucl. Instr. Meth. A **369**, 222 (1996).

[74] J. Frankland et al., Nucl. Instr. Meth. A **1082**, 170908 (2026).

[75] S. Valdré et al., Il Nuovo Cimento C **41**, 167 (2018).

[76] S. Valdré et al., Il Nuovo Cimento C **43**, A10 (2020).

[77] G. F. Knoll, *Radiation detection and measurement 4th ed.* (Wiley, New York, 2010).

[78] S. Carboni et al., Nucl. Instr. Meth. A **664**, 251 (2012).

[79] F. Benrachi et al., Nucl. Instrum. Meth. A **281**, 137 (1989).

[80] C. Frosin et al., Nucl. Instr. Meth. A **951**, 163018 (2020).

[81] F. Rami et al., Phys. Rev. Lett. **84**, 1120 (2000).

[82] C. Ciampi et al., Phys. Lett. B **868**, 139815 (2025).

[83] A. Rebillard-Soulié, PhD Thesis, Université de Caen Normandie (2024).

[84] H. Pais et al., Phys. Rev. Lett. **125**, 012701 (2020).

[85] T. Custódio et al., Phys. Rev. Lett. **134**, 082304 (2025).

[86] C. Ciampi, PhD Thesis, Università di Firenze (2021).
[87] https://kaliveda.in2p3.fr/.
[88] M. Parlog et al., Nucl. Instrum. Meth. A **482**, 693 (2002).
[89] M. Colonna et al., Nucl. Phys. A **642**, 449 (1998).
[90] P. Napolitani et al., Phys. Lett. B **726**, 382 (2013).
[91] A. Ono et al., Prog. Theor. Phys. **87**, 1185 (1992).
[92] A. Ono et al., Phys. Rev. C **53**, 2958 (1996).
[93] A. Ono et al., Phys. Rev. C **59**, 853 (1999).
[94] A. Ono et al., J. Phys. Conf. Ser. **420**, 012103 (2013).
[95] A. Ono et al., Prog. Part. Nucl. Phys. **105**, 139–179 (2019).
[96] A. Ono et al., Phys. Rev. C **66**, 014603 (2002).
[97] G. Tian et al., Phys. Rev. C **97**, 034610 (2018).
[98] R. J. Charity et al., Phys. Rev. C **82**, 014610 (2010).
[99] D. Lacroix et al., Phys. Rev. C **69**, 054604 (2004).
[100] D. Durand et al., Nucl. Phys. A **541**, 266 (1992).
[101] X. H. Zhang et al., Phys. Rev. C **85**, 024621 (2012).
[102] C. Frosin et al., Phys. Rev. C **107**, 044614 (2023).
[103] A. Rebillard-Soulié, Il Nuovo Cimento C **48**, 67 (2025).
[104] E. Chabanat et al., Nucl. Phys. A **635**, 231 (1998).
[105] G. A. Souliotis et al., Phys. Rev. C **90**, 064612 (2014).
[106] S. Piantelli et al., Phys. Rev. C **96**, 034622 (2017).
[107] S. Piantelli et al., Phys. Rev. C **99**, 064616 (2019).
[108] D. D. S. Coupland et al., Phys. Rev. C **84**, 054603 (2011).
[109] R. J. Charity et al., Nucl. Phys. A **483**, 371 (1988).
[110] W. Hauser and H. Feshbach, Phys. Rev. **87**, 366 (1952).
[111] N. Bohr et al., Phys. Rev. **56**, 426 (1939).
[112] L. G. Moretto et al., Nucl. Phys. A **247**, 211 (1975).
[113] R. J. Charity et al., Phys. Rev. C **58**, 1073 (1998).
[114] V. E. Viola et al., Phys. Rev. C **31**, 1550 (1985).
[115] C. Cavata et al., Phys. Rev. C **42**, 1760 (1990).
[116] C. Cugnon et al., Nucl. Phys. A **397**, 519 (1983).

[117] J. Frankland et al., Nucl. Phys. A **689**, 905 (2001).

[118] J. C. Steckmeyer et al., Nucl. Phys. A **686**, 537 (2001).

[119] E. Vient et al., Nucl. Phys. A **700**, 555 (2002).

[120] R. Yanez et al., Phys. Rev. C **68**, 011602 (2003).

[121] G. Tian et al., Phys. Rev. C **95**, 044613 (2017).

[122] R. Wang et al., Phys. Rev. C **110**, L031601 (2024).

[123] G. Lanzanò et al., Phys. Rev. C **58**, 1 (1998).

[124] S. Sweany et al., Nucl. Instrum. Meth. A **1018**, 165798 (2021).

[125] L. Baldesi et al., Nucl. Instrum. Meth. A **1075**, 170420 (2025).